Pore-Scale Modeling of Platinum Degradation in PEM Fuel Cells

by

Gerard Jaque Bulan Agravante

A thesis

presented to the University of Waterloo

in fulfillment of the

thesis requirement for the degree of

Master of Applied Science

in

Chemical Engineering

Waterloo, Ontario, Canada, 2026

© Gerard Jaque Bulan Agravante 2026

Author's Declaration

This thesis consists of material all of which I authored or co-authored: see Statement of Contributions included in the thesis. This is a true copy of the thesis, including any required final revisions, as accepted by my examiners.

I understand that my thesis may be made electronically available to the public.

Statement of Contributions

Parts of this thesis are based on manuscripts, both published and unpublished, as well as conference presentations, both completed and upcoming. As a first author in all works, I was the primary contributor to the design, execution, analysis, and communication (written and spoken) of the research. These works are also co-authored by my supervisor, Dr. Jeff Gostick, who contributed to the conceptualization, analysis, and revision, and played an important role in supervising my research direction. These contributions are outlined below.

Chapter 2.4 is based on the following published review paper:

- ***G. J. B. Agravante***, J. T. Gostick. "Physics-Based Modeling of Platinum Catalyst Dissolution and Oxidation in PEM Fuel Cells: A Focused Review" . Journal of The Electrochemical Society 173 (7), 074507 (2026). https://doi.org/10.1149/1945-7111/ae5740

Chapter 3 is based on the following published research article:

- ***G. J. B. Agravante***, J. T. Gostick. "Simulating transient pore-scale behaviour of platinum degradation in PEM fuel cells using pore network modeling". Journal of Power Sources 663, 238878 (2026). https://doi.org/10.1016/j.jpowsour.2025.238878

This work is also presented at the following conferences:

- (Oral Presentation) ***G. Agravante***, J. Gostick. "Pore Network Modeling of Platinum Catalyst Degradation in PEM Fuel Cells". 76th Annual Meeting of the International Society of Electrochemistry. Mainz, Germany. (Sep 2025).
- (Poster Presentation) ***G. Agravante***, J. Gostick. "Modeling Platinum Degradation in the Cathode Catalyst Layer of PEM Fuel Cells". 10th Waterloo Nanotechnology Conference. Waterloo, ON, Canada. (Mar 2025).

Chapter 4 is based on the following manuscript under review:

- ***G. Agravante***, J. Gostick. "Model-informed strategies for mitigating platinum loss in polymer electrolyte membrane fuel cells". (Submitted Mar. 14, 2026, ID: JFUE-D-26-03241). Preprint: https://doi.org/10.26434/chemrxiv.15001758/v1

This work is also intended to be presented at the following conference:

- (Online Presentation) ***G. Agravante***, J. Gostick. "In search of effective strategies for reducing platinum loss in polymer electrolyte membrane fuel cells". 18th Annual InterPore Meeting (InterPore 2026). Online. (May 2026).

Abstract

Heavy-duty vehicles rely primarily on diesel engines and produce disproportionately higher emissions in the transportation sector. They also lack feasible zero-emission alternatives due to their demanding range and load requirements. Polymer electrolyte membrane (PEM) fuel cells can offer a promising solution due to their long range, low weight, and fast refueling times. However, their application for heavy-duty vehicles is limited by durability issues which limit the fuel cell lifetime. In particular, platinum catalyst degradation in the cathode catalyst layer (CCL) is a critical degradation mechanism. Understanding the mechanisms of platinum degradation through physics-based modeling is essential for developing more durable fuel cells.

This thesis first presents an in-depth literature review of physics-based modeling approaches for platinum degradation, classifying the most widely used modeling frameworks and examining how recent studies have utilized and expanded upon them. The review then identified a key gap: the lack of pore-scale models capable of investigating the effects of the CCL microstructure and spatial properties on platinum degradation.

To address this gap, a transient pore-scale model of platinum degradation is first developed using pore network modeling. The model couples a performance solver (which simulates the oxygen reduction reaction) with a degradation solver (which simulates the degradation mechanisms of platinum dissolution, oxidation, and mass loss to the membrane). The model is able to reproduce key degradation trends including spatial variations in surface area loss and transient changes in platinum oxide coverage and ion concentration. Importantly, the pore-scale resolution reveals new microstructural insights, such as how constrictions between agglomerates lead to localized degradation and how the length of transport path correlates with platinum loss.

Building on the model developed, microstructural and spatial design strategies were systematically investigated. Strategies through modifications in the porosity, agglomerate size, and platinum placement were evaluated for their effects on performance and degradation. It was found that: (1) increasing porosity uniformly or near the membrane reduces platinum loss but worsens performance, although mid-CCL constrictions can minimize this trade-off, (2) reducing agglomerate size enhances performance and has negligible impact on degradation, and (3) increasing platinum loading near the membrane through larger particle sizes promotes more uniform degradation. A combined case study

integrating these strategies demonstrates simultaneous improvements in initial performance, total degradation, and degradation uniformity. These results indicate that while individual strategies have distinct trade-offs, combining complementary strategies can retain their advantages while minimizing the drawbacks.

Overall, the works presented in this thesis demonstrate the utility of pore-scale modeling for uncovering microstructural insights and identifying mitigation strategies for platinum degradation through the CCL design, which can ultimately contribute to the advancement of PEM fuel cells as a viable clean energy technology for heavy-duty vehicles.

Acknowledgements

As they say, it takes a village to raise a master's-level chemical engineering researcher, so I would like to acknowledge the support of everyone who played a part in my master's journey, including but not limited to:

- The janitor of E6 5th floor, Mr. Ioan Ciotmonda, who would give us life wisdom whenever we worked late.
- The service workers at the uni plaza (I get food there pretty often).
- The Chemical Engineering admin staff (especially Judy) – the people who keep the whole department together.
- The people of Canada 🍁 and UWaterloo 🦢 (I got federal and institutional scholarships for my master's funding). I hope my research and the skills I gained in this degree can make a positive impact on our community in the future, as a way of giving back.
- The artists and bands (mostly queer and mostly British for some reason) whose music has the magical ability to get me through difficult tasks.
- My readers, Dr. Michael Fowler and Dr. Eric Croiset, for reading excellently and providing great suggestions.
- My lab siblings: Hao, Mike, Nik, Mohammad, Serveh, Ricky, Brendan, Daniel (adopted), the van der Heijden lab – all Dr.'s, future Dr.'s and masters.
    - Especially to Nik, the guy I wanna be when I grow up.

  I feel so honoured and inspired to be among super smart people. Your numerous pieces of advice are noted in my survival guide for my life's next chapter (more grad school).
- My awesome supervisor, Dr. Jeff Gostick, who provided the following: coffee supply, printer toner, BBQ, group lunches, Japanese snacks, the best mentorship, cool opportunities, belief in my abilities, and an academic legend to look up to (that's him!). Thank you for giving me a chance. I look forward to being your student again.

- The great friends I made here (including the ones above) and all over the world. Even the smallest gestures like a DM to check up on me played a huge part in keeping me mentally stable. Special mention to my homegirls: Pristina, Faria, Trisha, and Hazel ❤️.
- My family. Ate Joy for providing me with everything I need in Waterloo and Luke for being the cutest nephew. You two have been my home away from home. Papa Bing for being my tour companion in Germany. The rest of the Agravantes of Samar and Bulans of Isabela. Most importantly, my parents who have given all the love and support that I needed, even from afar. My gratitude is infinite for your sacrifices that made it possible for me to achieve this impossible dream. *Sabi nga nila,"malayo pa, pero malayo na"*.

Dedication

Ha akon igkasi

[To my fellow]

Apo hin kakablas, anak hin kakurian

[Grandchild of poverty, child of struggle]

…

Han gintatalumpigos han kalibutan

[To those oppressed by the world]

Nga padayon nga naduso ngadto ha katadungan

[Who continue to strive for justice]

…

Ha iyo tanan

[To all of you]

Nga nakikigbisog para ha gahum han kaadman

[Who fight for the power of knowledge]

…

Table of Contents

Author's Declaration ii

Statement of Contributions iii

Abstract iv

Acknowledgements vi

Dedication viii

List of Figures xiii

List of Tables xviii

List of Abbreviations xix

List of Symbols xx

Chapter 1 Introduction 1

1.1 Research Motivation 1

1.2 Objective 1

1.3 Thesis Structure 2

Chapter 2 Background and Literature Review 3

2.1 Heavy-Duty Vehicles: A Decarbonization Dilemma 3

2.2 Fuel Cells as a Promising Solution 6

2.2.1 Alternatives to Diesel Engine 6

2.2.2 The PEM Fuel Cell 7

2.3 A Solution That Wears Away: The Platinum Degradation Problem 9

2.3.1 Fuel Cells, Durability, and Degradation 9

2.3.2 Platinum Degradation Mechanisms 11

2.4 Physics-Based Modeling of Platinum Catalyst Dissolution and Oxidation 13

2.4.1 Overview of Platinum Degradation Mechanisms 13

2.4.2 Darling-Meyers Model 16
2.4.3 Holby-Morgan Model 23
2.4.4 Rinaldo-Stumper-Eikerling Model 30
2.4.5 Other Models 34
2.4.6 Discussion and Outlook 38
2.5 Balancing Computational Accuracy and Complexity with Pore Network Modeling 46
2.5.1 The Porous Cathode Catalyst Layer 46
2.5.2 Pore-Scale Modeling 47
2.5.3 Pore Network Modeling 49
Chapter 3 Simulating Transient Pore-Scale Behaviour of Platinum Degradation in PEM Fuel Cells 51
3.1 Overview 51
3.2 Geometry Generation 52
3.2.1 Network Generation 52
3.2.2 Network Validation 56
3.2.3 Addition of Platinum Particles 59
3.3 Model Development 60
3.3.1 Modelling Strategy 60
3.3.2 Performance Solver 62
3.3.3 Degradation Solver 68
3.4 Results and Discussion 73
3.4.1 Model Calibration 73
3.4.2 Oxygen Transport and Overpotential at Different Voltages 77
3.4.3 Temporal and Spatial Trends of Degradation 78
3.4.4 Effects of the Pore Structure 84

3.5 Conclusions 87
Chapter 4 Model-Informed Strategies for Mitigating Platinum Loss in PEM Fuel Cells 90
4.1 Overview 90
4.1.1 Hypotheses 91
4.2 Methods 92
4.2.1 Base Case 92
4.2.2 Catalyst Layer Construction and Validation 93
4.2.3 Degradation Model Description and Calibration 94
4.2.4 Metrics 97
4.2.5 Analysis 97
4.3 Results and Discussion 101
4.3.1 Microstructural Modification: Porosity Effects 101
4.3.2 Microstructural Modification: Agglomerate Size Effects 105
4.3.3 Platinum Placement Effects 106
4.3.4 Case Study: Combined Strategies 110
4.3.5 Limitations of the Analyses 114
4.4 Conclusions and Recommendations 115
Chapter 5 Overall Conclusions and Future Work 117
5.1 Summary and Outcomes 117
5.1.1 Categorization and Evaluation of Platinum Degradation Models 117
5.1.2 The First Pore Network Model of Platinum Degradation 117
5.1.3 Significance of Microstructural and Spatial Variables on Degradation 118
5.2 Outlook and Perspectives 119
5.2.1 Improving Solver Performance 119

5.2.2 Extending Model Physics and Coupling 119
5.2.3 Optimizing CCL Structure for Durability 120
5.2.4 Translating Modeling Insights to Experiment 120
5.2.5 Final Perspective 121
References 122
Appendix A Modifications to the Blob Generation Algorithm 139
Appendix B Metric Calculation 144
Initial Performance 144
Degradation Reduction 145
Degradation Homogeneity 145
Appendix C Study on the Significance of Degradation Homogeneity 147

List of Figures

Figure 2-1: a.) Global greenhouse gas emissions by sector (2021) [6] and b.) Canadian NOx emissions by sector (2022) [7] 4

Figure 2-2: Yearly greenhouse gas emissions in Canadian Transportation [10] 5

Figure 2-3: Simplified illustration of the components, species, and reactions in a polymer electrolyte membrane fuel cell 8

Figure 2-4: Degradation mechanisms in different PEMFC components 10

Figure 2-5: Platinum degradation mechanisms 12

Figure 2-6: (a.) Electrochemical dissolution of platinum and (b.) electrochemical oxide formation on the platinum surface 14

Figure 2-7: Modified Pourbaix diagram of platinum for bulk (planar surface) and platinum nanoparticles of different diameters (in Pt^{2+} concentration of 10^{-6} M) using data from Tang et al. [57], showing the size-dependence of platinum stability 15

Figure 2-8: Data from Darling and Meyers[65] comparing simulated ECSA losses for potentiostatic holds of 1.2, 1.05, and 0.87 V and for square-wave cycling from 0.87 V to 1.2 V with 30 s period .. 17

Figure 2-9: Performance degradation rate and platinum concentration in the membrane obtained at different LPL with UPL=1.35 from Zhang et al. [50] showing three distinct regions of different dissolution behaviour from the interactions between the dissolution and oxidation reactions 21

Figure 2-10: Effects of platinum particle size distribution (PSD) on degradation behavior in the Holby and Morgan models. Panels (a) and (b), adapted from Holby et al. [59], show the influence of different mean PSD sizes, with (a) the initial PSD profiles and (b) the corresponding electrochemically active surface area (ECSA) loss for mean particle sizes of 2, 3, 4, and 5 nm. Panels (c) and (d), adapted from Holby and Morgan [77], shows the effects of different PSD distribution types, with (c) the initial PSD profiles and (d) the corresponding ECSA loss for log-normal, flat, Gaussian (narrow and wide), and delta (single-size) distributions. 24

Figure 2-11: Comparisons of optimized dissolution and redeposition rate constants from Baroody et al. [99] for (a.) low surface area carbon (LSAC) and (b.) medium surface area carbon (MSAC) 34

Figure 2-12: Schematic of the electrochemical double layer representation at the Pt/C-ionomer interface by Franco and Tembely [115], consisting of an inner layer (divided into platinum and compact sublayers) and a diffuse layer..... 38

Figure 2-13: Distribution of the relevant papers reviewed, categorized by year of publication and model dimensionality. The figure highlights the gradual shift toward higher-dimensional models and greater complexity..... 42

Figure 2-14: The cathode catalyst layer 47

Figure 2-15: a.) Simple three-pore pore network. b.) Pore-throat-pore conduit..... 50

Figure 3-1: Pore network approximation of the CCL..... 53

Figure 3-2: Comparison of agglomerate size distributions between the generated structure used in this work and a reconstructed catalyst layer from Epting and Lister 54

Figure 3-3: Algorithm used to generate an artificial image of the CCL..... 56

Figure 3-4: Ionomer conductivity curves for rt =0.9*min(rp) and rt =0.1*min(rp) and the chosen case compared to the conductivity range in Olbrich et al.'s model..... 59

Figure 3-5: Outline of the degradation modelling strategy employed..... 61

Figure 3-6: Flowchart of the algorithm used for the performance solver..... 63

Figure 3-7: Flowchart of the algorithm used for the degradation solver..... 70

Figure 3-8: a.) Polarization curve of the fitted model compared to experimental data from Braaten et al. b.) Empirical mass loss model curve in the first five cycles plotted with the fitted mass loss simulation data from the degradation model..... 77

Figure 3-9: Images of the pore network CCL showing a.) oxygen concentration and b.) overpotential for each pore at cell voltages of 0.9 V, 0.6 V, and 0.3 V. The left side of each image corresponds to the PEM-CCL interface, while the right side corresponds to the CCL-GDL interface..... 78

Figure 3-10: Map of the CCL by cycle in terms of surface area remaining for the platinum sites in each pore, relative to the initial surface area. The PEM-CCL interface is on the left side of each image and the CCL-GDL interface is on the right. 80

Figure 3-11: Profiles of slice-averaged surface area remaining plotted by distance from PEM at the end of each cycle. b.) 3D surface plot representing the slice-averaged surface area lost plotted with distance from the membrane and time. The surface area lost is multiplied by a factor of 40 and the voltage cycling is displayed on the y=0 plane to show the effects of voltage cycling on surface area lost 81

Figure 3-12: The a.) average oxide coverage of the platinum sites in the CCL during the first cycle is shown along with the b.) oxide coverage map of the CCL at discrete time points of 1, 2, 3, 4, 5, and 6 seconds. The PEM-CCL interface is on the left side of each image and the CCL-GDL interface is on the right..... 82

Figure 3-13: The a.) average platinum ion concentration in the CCL during the first cycle is shown along with the b.) platinum ion concentration map of the CCL at discrete time points of 1, 2, 3, 4, 5, and 6 seconds. The PEM-CCL interface is on the left side of each image and the CCL-GDL interface is on the right. 83

Figure 3-14: 3D surface plots with distance from the PEM and time of a.) oxide coverage and b.) platinum ion concentration (multiplied by a factor of 100), both averaged in the x-position. In both graph, the voltage cycling is displayed on the y=0 plane to show the effects of voltage cycling 84

Figure 3-15: a.) Map of the surface area remaining after cycle five and b.) scatter plots of the slice-averaged surface area values at each x-coordinate, together with their moving average. In both plots, the red dashed line represents the location at which there is an observed shift in the degradation behaviour, with the pores on the left of the line showing a steeper and more drastic degradation 85

Figure 3-16: a.) Coloured map of the transport length values for each pore in the CCL. b.) Surface area remaining for each pore plotted with the transport length and coloured by initial platinum size. 87

Figure 4-1: a.) 3D pore connectivity of the generated base-case CCL geometry. b.) Ionomer conductivity curves for the 3D networks generated with throat radii $r_t=0.8*r_p$ and $r_t=0.1*r_p$, plotted together with the chosen parameter set applied in all simulations and overlaid with the ionomer conductfivity model range reported by Braaten et al. [135]. c.) Agglomerate size distribution of the base case compared with experimentally reported agglomerate size distribution data from Epting and Lister [137]. d.) Polarization curve fitted with experimental data from Braaten et al. [135]. e.) Mass loss curve fitted from empirical model [159] 96

Figure 4-2: Left panel: slice-averaged porosity profiles in the through-plane direction for the a.) uniformly-varied porosity, d.) spatially-varied porosity, and g.) applied constrictions. Centre panel: polarization curves representing the initial performance for the b.) uniformly-varied porosity, e.) spatially-varied porosity, and h.) porosity constrictions. Right panel: slice-averaged surface area loss in the through-plane direction and overall surface area loss (dotted horizontal lines) for the c.) uniformly-varied porosity, f.) spatially-varied porosity, and i.) porosity constrictions. The base case is plotted in all plots for comparison. 104

Figure 4-3: a.) Fitted Gaussian distribution of different geometries with varied agglomerate sizes, along with the average agglomerate diameter. b.) Polarization curves representing the initial performances. c.) Slice-averaged surface area loss in the through-plane direction and overall surface area loss (dotted horizontal lines). The base case is plotted for comparison. 106

Figure 4-4: Left panel: slice-averaged number density of particle per pore for the a.) size-varied loading and e.) number-varied loading; with the slice-averaged platinum radius for the b.) size-varied loading and f.) number-varied loading. Centre panel: Polarization curves representing the initial performances for c.) size-varied loading and g.) number-varied loading. Right panel: Slice-averaged surface area loss in the through-plane direction and overall surface area loss (dotted horizontal lines) for the d.) size-varied loading and h.) number-varied loading 109

Figure 4-5 a.) Initial performances for the case study simulations compared to the base case. b.) Slice-averaged surface area loss in the through-plane direction and overall surface area loss (dotted

horizontal lines) for the case study simulations compared to the base case. c.) Current density increase plotted vs. ECSA loss reduction for all simulations run. d.) ECSA loss CoV reduction plotted vs. ECSA loss reduction for all simulations run 112

List of Tables

Table 2.1: Comparison between diesel, battery, and hydrogen fuel cell for heavy-duty vehicles adapted from [17] 7

Table 2.2: Values of the fitted and assumed parameters taken from select publications using Darling-Meyers model 22

Table 2.3: Values of the fitted and assumed parameters taken from select publications using Holby-Morgan model 29

Table 2.4: List of parameter values obtained by Rinaldo et al.[61], [95] from model fitting with different experimental data 31

Table 3.1: Parameters used in geometry generation, along with the operation conditions 58

Table 3.2: Parameters used in performance solver 73

Table 3.3: Parameters used in the degradation solver 75

Table 4.1 Fitting parameters from with the calibrated values used in this study 97

Table 4.2: Summary of simulation cases analyzed in this study with varying porosity profiles, mean agglomerate sizes, and spatial platinum loading distributions 99

Table 4.3: Table of simulation results 113

List of Abbreviations

0/1/2/3D	zero-/one-/two-/three-dimensional
AST	Accelerated stress test
BEV	Battery electric vehicle
BOL	Beginning-of-life
CCL	Cathode catalyst layer
CoV	Coefficient of variation
ECSA	Electrochemically active surface area
FCV	Fuel cell vehicle
GDL	Gas diffusion layer
GPU	Graphics processing unit
HFCV	Hydrogen fuel cell vehicle
HOR	Hydrogen oxidation reaction
HT-PEMFC	High-temperature polymer electrolyte membrane fuel cells
LPL	Lower potential limit
M2FCT	Million-mile fuel cell truck
MEA	Membrane-electrode assembly
ORR	Oxygen reduction reaction
PEM	Polymer electrolyte membrane
PEMFC	Polymer electrolyte / Proton exchange membrane fuel cell
PFSA	Perfluorosulfonic acid
PM	Particulate matter
PNM	Pore network model
PSD	Pore / Particle size distribution
PTFE	Polytetrafluoroethylene
RAM	Random access memory
RK4	Fourth order Runge-Kutta method
UPL	Upper potential limit

List of Symbols

Chapter 2 Symbols (arranged by appearance)

$\boldsymbol{F}$	Faraday's constant [A mol^{-1}]
$\boldsymbol{R}$	Gas constant [J mol^{-1}]
$\boldsymbol{T}$	Temperature [K]
$\boldsymbol{pH}$	pH [-]
$\boldsymbol{r}$	Platinum particle radius [m]
$\boldsymbol{\theta}$	Platinum oxide coverage [-]
$\boldsymbol{\theta_{vac}}$	Proportion of the catalyst surface area that is vacant [-]
$\boldsymbol{c_{Pt^{2+}}}$	Platinum ion concentration [mol m^{-3}]
$\boldsymbol{c_{Pt^{2+},ref}}$	Reference platinum ion concentration [mol m^{-3}]
$\boldsymbol{c_{H^{+}}}$	Proton concentration [mol m^{-3}]
$\boldsymbol{c_{H^{+},ref}}$	Reference proton concentration [mol m^{-3}]
$\boldsymbol{\Gamma}$	Platinum surface density [mol m^{-2}]
$\boldsymbol{R_1}$	Rate of platinum dissolution (Reaction (1)) [mol m^{-2} s^{-1}]
$\boldsymbol{R_2}$	Rate of platinum oxide formation (Reaction (2)) [mol m^{-2} s^{-1}]
$\boldsymbol{R_3}$	Rate of platinum oxide dissolution (Reaction (3)) [mol m^{-2} s^{-1}]
$\boldsymbol{k_1}$	Rate constant for R_1 [mol m^{-2} s^{-1}]
$\boldsymbol{k_2}$	Rate constant for R_2 [mol m^{-2} s^{-1}]
$\boldsymbol{k_3}$	Rate constant for R_3 [mol m^{-2} s^{-1}]
$\boldsymbol{U_1^{\theta}}$	Standard thermodynamic potential of Reaction (1) [V]
$\boldsymbol{U_2^{\theta}}$	Standard thermodynamic potential of Reaction (2) [V]
$\boldsymbol{\alpha_{a,1}}$	Anodic transfer coefficient of Reaction (1) [-]
$\boldsymbol{\alpha_{c,1}}$	Cathodic transfer coefficient of Reaction (1) [-]
$\boldsymbol{\beta_1}$	Symmetry factor of Reaction (1) [-]

$\alpha_{a,2}$	Anodic transfer coefficient of Reaction (2) [-]
$\alpha_{c,2}$	Cathodic transfer coefficient of Reaction (2) [-]
β_2	Symmetry factor of Reaction (2) [-]
n_1	Number of equivalent electrons transferred per Pt dissolved [-]
n_2	Number of equivalent electrons transferred per Pt oxidized [-]
ϕ_s	Solid potential [V]
ϕ_l	Electrolyte potential [V]
V	Cell voltage [V]
ω	Platinum oxide-oxide interaction coefficient [-]
σ_{Pt}	Surface tension of platinum [J m^{-2}]
M_{Pt}	Molecular weight of platinum [kg mol^{-1}]
ρ_{Pt}	Density of platinum [kg m^{-3}]
σ_{PtO}	Surface tension of platinum oxide [J m^{-2}]
M_{PtO}	Molecular weight of platinum oxide [kg mol^{-1}]
ρ_{PtO}	Density of platinum oxide [kg m^{-3}]
$\Delta\mu^0_{PtO}$	Chemical potential shift for platinum oxide [J mol^{-1}]
$\bar{\bar{N}}$	Number of platinum particles per electrode volume [m^{-3}]
ε	CCL porosity [-]
v_1	Forward dissolution reaction attempt frequency [s^{-1}]
v_2	Backward dissolution reaction attempt frequency [s^{-1}]
$v_{1,ox}$	Forward oxidation reaction attempt frequency [s^{-1}]
$v_{2,ox}$	Backward oxidation reaction attempt frequency [s^{-1}]
$\bar{H}_{1,fit}$	Partial molar dissolution activation enthalpy [J mol^{-1}]
$\bar{H}_{2,fit}$	Partial molar zero-coverage oxide formation activation enthalpy [J mol^{-1}]
Ω_{Pt}	Molar volume of platinum [m^3 mol^{-1}]
$\bar{S}'_{H_2O}$	Water partial molar entropy [J K^{-1} mol^{-1}]

$\bar{S}'_{PtH_2O}$	Activation state partial molar entropy [J K^{-1} mol^{-1}]
U_{fit}	Oxide formation bulk equilibrium voltage [V]
λ	Oxide dependent kinetic barrier constant [J mol^{-1}]
ξ	Excluded volume [-]
N	Number of platinum particles [-]
$\Delta \mathbf{v}$	Effective volume of the first electrolyte volume increment
K_{rdp}	Redeposition rate constant [m s^{-1}]
K_{dis}	Dissolution rate constant [m s^{-1}]
β	Dimensionless proportionality constant [-]
R	Resistance [generic]

Chapter 3 Symbols (arranged by appearance)

σ	Gaussian blur parameter [-]
τ	Image threshold parameter [-]
L_{CCL}	CCL length [m]
r_c	Carbon particle radius [m]
ξ	Ionomer-to-carbon weight ratio [-]
n_t	Number of throats [-]
n_p	Number of pores [-]
r_p	Pore radius [m]
r_t	Throat radius [m]
l_t	Throat length [m]
$\rho_{ionomer}$	Ionomer density [kg m^{-3}]
ρ_{carbon}	Carbon density [kg m^{-3}]
ρ_{H_2O}	Water density [kg m^{-3}]
n_{px}	Number of x pixels [-]

σ_{bulk}	Bulk protonic conductivity [S m^{-1}]
σ_{eff}	Effective protonic conductivity [S m^{-1}]
T	Temperature [K]
P	Pressure [Pa]
λ	Water content [-]
RH	Relative humidity [-]
E_{left}	Left applied voltage [V]
I	Current [A]
A_{CCL}	CCL cross-sectional area [m^2]
g	Effective-to-bulk conductivity ration [-]
x_{ion}	Ionomer volume fraction [-]
n_{Pt}	Number of platinum [-]
λ_{Pt}	Platinum loading [kg m^{-2}]
V_{Pt}	Platinum particle volume [m^3]
η	Overpotential [V]
ϕ_s	Electrode potential [V]
ϕ_l	Electrolyte potential [V]
E_{eq}	Open-circuit voltage [V]
R	Reaction rate [mol s^{-1}]
c	Dissolved oxygen concentration [mol m^3]
c_0	Reference dissolved oxygen concentration [mol m^3]
j_0	Exchange current density [A m^{-2}]
n	Number of electrons transferred in the overall reaction [-]
z	Number of electrons transferred in the rate-limiting step [-]
$\alpha_{a,ORR}$	Anodic transfer coefficient [-]
$\alpha_{c,ORR}$	Cathodic transfer coefficient [-]

$\boldsymbol{F}$	Faraday's constant [A s mol^{-1}]
$\boldsymbol{R}$	Universal gas constant [m^3 Pa K^{-1} mol^{-1}]
$\boldsymbol{A_{Pt}}$	Platinum particle surface area [m^2]
$\boldsymbol{\theta_{vac}}$	Fraction of vacant sites in platinum surface [-]
$\boldsymbol{\theta_{PtO}}$	Fraction of sites covered by PtO in platinum surface [-]
$\boldsymbol{G}$, $\boldsymbol{g}$	Diffusive conductance [m^3 s^{-1}]
$\boldsymbol{D_{O_2,ion}}$	Diffusivity of oxygen in ionomer [m^2 s^{-1}]
$\boldsymbol{A_p}$	Pore cross-sectional area [m^2]
$\boldsymbol{A_t}$	Throat cross-sectional area [m^2]
$\boldsymbol{c_{outside}}$	Concentration of oxygen entering the GDL [mol m^3]
$\boldsymbol{H_{O_2,ion}}$	Dimensionless Henry's constant of oxygen from void to ionomer [-]
$\boldsymbol{\varepsilon_{GDL}}$	GDL porosity [-]
$\boldsymbol{\tau_{GDL}}$	GDL tortuosity [-]
$\boldsymbol{P_{v,H_2O}}$	Vapour pressure of water [Pa]
$\boldsymbol{Q}$, $\boldsymbol{q}$	Protonic conductance [S]
$\boldsymbol{\phi_{PEM}}$	Ionomer voltage at the left boundary of the PEM [V]
$\boldsymbol{\varepsilon}$	Calculation error for electrolyte potential [V]
$\boldsymbol{c_{Pt^{2+}}}$	Platinum ion concentration [mol m^3]
$\boldsymbol{c_{Pt^{2+}}^{ref}}$	Reference platinum ion concentration [mol m^{-3}]
$\boldsymbol{c_{H^+}}$	Proton concentration [mol m^{-3}]
$\boldsymbol{c_{H^+}^{ref}}$	Reference proton concentration [mol m^{-3}]
$\boldsymbol{\Gamma}$	Platinum surface density [mol m^{-2}]
$\boldsymbol{R_{diss}}$	Rate of platinum dissolution [mol m^{-2} s^{-1}]
$\boldsymbol{R_{PtO}}$	Rate of platinum oxide formation [mol m^{-2} s^{-1}]
$\boldsymbol{R_3}$	Rate of platinum oxide dissolution [mol m^{-2} s^{-1}]
$\boldsymbol{k_{diss}}$	Rate constant for platinum dissolution [mol m^{-2} s^{-1}]

k_{PtO}	Rate constant for platinum oxidation	[mol m^{-2} s^{-1}]
k_3	Rate constant for platinum oxide formation	[mol m^{-2} s^{-1}]
U_{diss}^{θ}	Standard thermodynamic potential of platinum dissolution	[V]
U_{PtO}^{θ}	Standard thermodynamic potential of platinum oxidation	[V]
$\alpha_{diss,a}$	Anodic transfer coefficient of platinum dissolution	[-]
$\alpha_{diss,c}$	Cathodic transfer coefficient of platinum dissolution	[-]
$\alpha_{PtO,a}$	Anodic transfer coefficient of platinum oxidation	[-]
$\alpha_{PtO,c}$	Cathodic transfer coefficient of platinum oxidation	[-]
n_{diss}	Number of equivalent electrons transferred per Pt dissolved	[-]
n_{PtO}	Number of equivalent electrons transferred per Pt oxidized	[-]
ϕ_s	Solid potential	[V]
ϕ_l	Electrolyte potential	[V]
ω_{PtO}	Platinum oxide-oxide interaction coefficient	[-]
σ_{Pt}	Surface tension of platinum	[J m^{-2}]
M_{Pt}	Molecular weight of platinum	[kg mol^{-1}]
ρ_{Pt}	Density of platinum	[kg m^{-3}]
σ_{PtO}	Surface tension of platinum oxide	[J m^{-2}]
M_{PtO}	Molecular weight of platinum oxide	[kg mol^{-1}]
ρ_{PtO}	Density of platinum oxide	[kg m^{-3}]
$\Delta\mu_{PtO}^{0}$	Chemical potential shift for platinum oxide	[J mol^{-1}]
$D_{Pt^{2+},ion}$	Platinum diffusivity in the ionomer	[m^2 s^{-1}]
Y	Platinum membrane band loss term	[mol s^{-1}]
x_{band}	Location of the platinum band relative to PEM-CCL interface	[m]
M	Normalized mass loss	[-]
M_{min}, k	Fitting parameters for empirical mass loss equation	[-]
N	Cycle number	

Chapter 4 Symbols (arranged by appearance)

$\boldsymbol{\varepsilon}$	CCL Porosity [-]
$\boldsymbol{\beta}$	Blobiness parameter [-]
$\boldsymbol{r_t}$	Throat radius [m]
$\boldsymbol{r_p}$	Pore radius [m]
$\boldsymbol{l}$	Platinum loading [mg cm^{-2}]

Chapter 1
Introduction

1.1 Research Motivation

Heavy-duty vehicles are economically essential due to their role in freight transportation, but they also remain among the most difficult vehicles to decarbonize due to their reliance on diesel engines. Polymer electrolyte membrane (PEM) fuel cells offer a promising zero-emission alternative due to their suitability for heavy-duty operation. Despite their advantages, durability remains a major barrier for the deployment of fuel cell heavy-duty vehicles, as they are required to have long lifetimes under demanding conditions. These conditions accelerate the degradation of several components within the cell, leading to performance loss over time.

Among the various degradation mechanisms, platinum catalyst degradation in the cathode catalyst layer (CCL) is widely recognized as a critical contributor to performance loss. Platinum coarsening and mass loss reduce the electrochemically active surface area, which consequently affects the kinetics of the cathodic oxygen reduction reaction. The CCL is a thin, heterogeneous structure which makes experimental probing of degradation mechanisms challenging. Furthermore, the inherently multiscale and multiphysics nature of the CCL makes modeling efforts more difficult. Although numerous studies have investigated platinum degradation mechanisms, there remains a lack of pore-scale modeling frameworks that are capable of resolving transient platinum degradation within catalyst layer microstructures. Addressing this gap is essential for linking microstructural effects to degradation behavior and ultimately informing the design of more durable catalyst layers.

This research is thus motivated by the need to develop a pore-scale model that enables the investigation of platinum degradation within the cathode catalyst layer and the exploration of pore-scale mitigation strategies.

1.2 Objective

To address the identified gap, this research is structured around two primary objectives:

1. Model Development: Develop a pore-scale model capable of simulating transient platinum degradation in the cathode catalyst layer by coupling species transport with platinum degradation mechanisms.
2. Model Application: Utilize the developed model to investigate the effects of structural and spatial parameters on both the fuel cell performance and degradation behaviour.

1.3 Thesis Structure

The main contents of this thesis are organized as follows:

- Chapter 2 presents the relevant background and literature review, including an introduction to the decarbonization problem in heavy-duty vehicles, an overview of platinum degradation mechanisms, an in-depth review of existing models and computational approaches for the problem, and an introduction to pore network modeling as the framework adopted in this study.
- Chapter 3 addresses the first objective by detailing the development of the pore network model. The chapter primarily outlines the model development which includes the coupling of a performance solver, which models the cathodic reaction, with a degradation solver that captures platinum dissolution and oxidation reactions. Additionally, the geometry generation process, the model assumptions and simplifications, and model validation and calibration are explored. The resulting model enables transient, pore-scale simulations of degradation and shows agreement with trends reported in experimental and modeling studies.
- Chapter 4 addresses the second objective by applying the developed model to investigate the influence of microstructural and spatial parameters. Studies are conducted to evaluate the effects of catalyst distribution and microstructural modifications on both the degradation and performance. The results demonstrate how a combination of targeted strategies may help address the trade-off between durability and performance.
- Chapter 5 summarizes the key findings of this work and outlines recommendations for future research directions.

Chapter 2
Background and Literature Review

2.1 Heavy-Duty Vehicles: A Decarbonization Dilemma

Under current policies on greenhouse gas emissions, the global mean temperature is projected to increase by 2 to 3 °C above pre-industrial levels by 2100 [1], with net-zero emissions not being achieved by 2100 [2]. This level of warming is expected to increase the frequency and intensity of extreme weather events, heighten health risks (particularly those related to heat and humidity), affect wildlife and biodiversity, and disrupt food supply and production [3]. Collectively, these impacts will have profound environmental, economic, and sociopolitical consequences worldwide, and will affect vulnerable communities which contribute the least to global emissions per capita [3].

At the same time, air pollution remains a major public health concern, particularly in densely populated areas where emissions from urban activities are highly concentrated. These impacts again affect low-income communities [4]. Pollutants such as NO_x (nitrogen oxides), SO_x (sulfur oxides), and particulate matter are known to contribute to respiratory and cardiovascular diseases [4]. In fact, exposure to particulate matter was identified as the leading contributor to the global disease burden in 2021 [5].

The transportation sector contributes a significant share of greenhouse gas and pollutant emissions due to its reliance on fossil fuels. For example, Figure 2-1a illustrates the contribution of different sectors to global greenhouse gas emissions in 2021, showing that transportation accounts for 15.5% of total emissions. In terms of air pollutant emissions, Figure 2-1b shows a Canadian example, where transportation is responsible for 41.8% of total NO_x emissions in Canada.

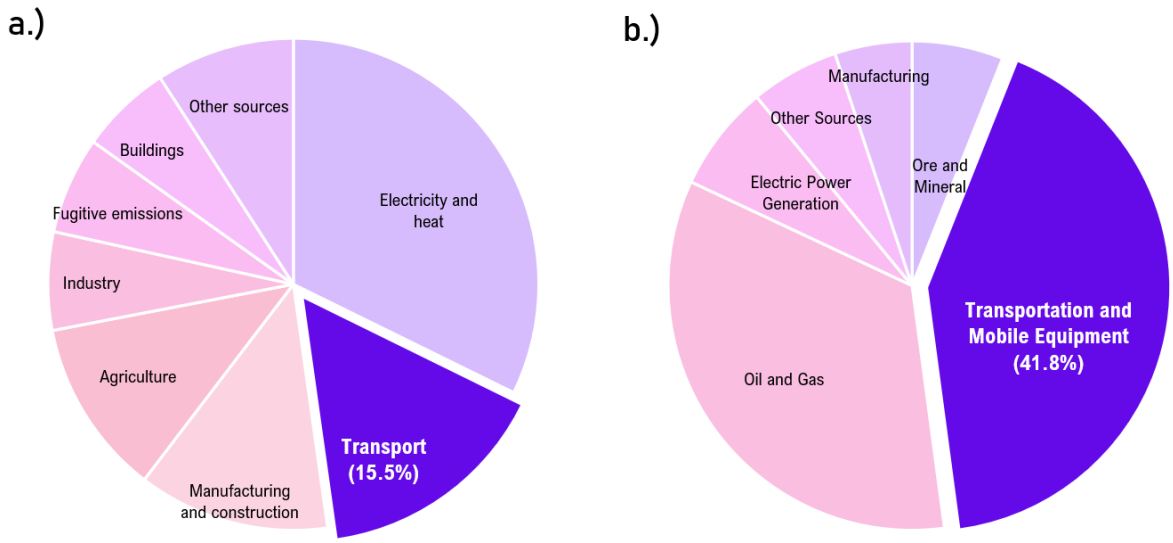


Figure 2-1: a.) Global greenhouse gas emissions by sector (2021) [6] and b.) Canadian NOx emissions by sector (2022) [7]

More concerning in the Canadian context is that transportation-related emissions continue to increase. Figure 2-2 presents greenhouse gas emissions from the transportation sector in Canada, separated by vehicle type. Despite declining emissions from passenger and light-duty vehicles, likely due to the widespread adoption of emissions-reducing technologies and stricter regulations, [8], total transportation emissions show a persistent upward trend. It is evident in the graph that this increase is primarily driven by rising emissions from heavy-duty vehicles. Notably, heavy-duty vehicles accounted for only 2.2% of the total vehicle fleet in 2019 [9], yet were responsible for nearly 34% of transportation-related greenhouse gas emissions [10]. This disproportionate contribution arises from the continued reliance of heavy-duty trucks on diesel internal combustion engines, which emit substantially higher levels of pollutants; for example, diesel trucks emit over 100 times more $PM_{2.5}$ than light-duty vehicles [11]. To date, the continued use of diesel engines can be attributed to the fact that no alternative powertrain technology has matched diesel engines in terms of durability, energy efficiency, and low operating cost in the heavy-duty sector [12].

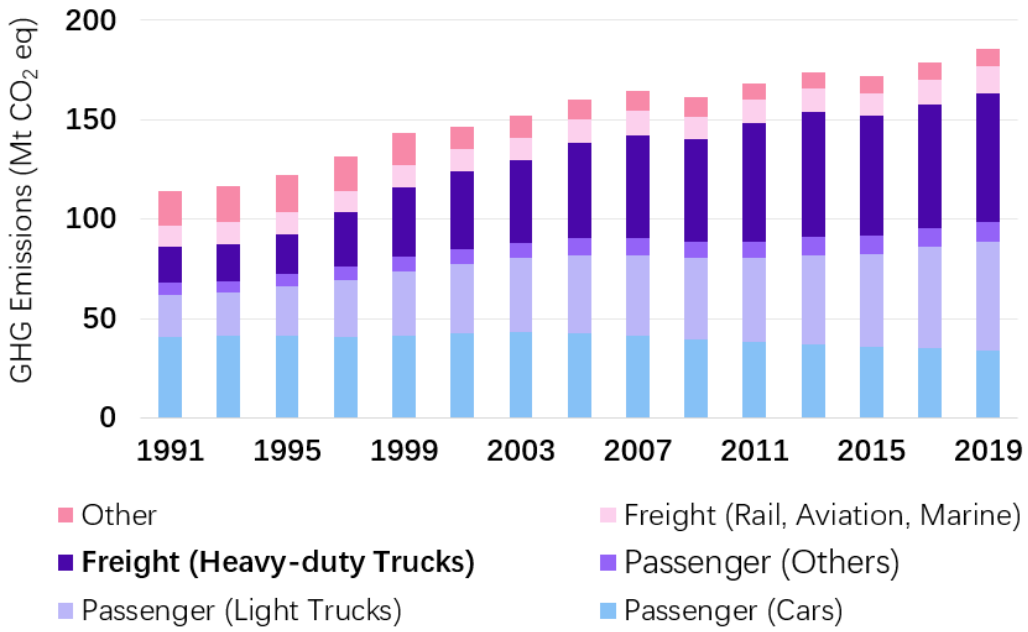


Figure 2-2: Yearly greenhouse gas emissions in Canadian Transportation [10]

At the same time, heavy-duty trucks play a critical role in the economy due to their significant role in freight transportation [11]. The transportation and warehousing sector contributes 3.6% of Canada's gross domestic product and employs 5.2% of the national workforce, while trucks carry 77.7% of the total volume of goods transported domestically [13]. In the United States, a country with comparable economic and logistical characteristics, the demand for freight transport is projected to increase by nearly 50% by 2050 [11]. Together, these trends emphasize the urgent need to develop viable alternatives to diesel engines for heavy-duty vehicles, as emissions reductions in this sector are essential for mitigating climate change and air pollution without compromising economic growth.

These facts highlight a central dilemma: the vehicles that contribute disproportionately to emissions are also among the most difficult to decarbonize, as they cannot simply be phased out without disrupting essential economic activity. This creates the need for the development of alternative technologies capable of matching diesel engines in terms of functionality and cost. Viable alternatives for heavy-duty vehicles must possess several key characteristics to compete with diesel engines, such as durability, high energy efficiency, and cost competitiveness, while simultaneously achieving low- to zero-emission operation.

2.2 Fuel Cells as a Promising Solution

2.2.1 Alternatives to Diesel Engine

Several lower-emission alternative technologies have been proposed for heavy-duty vehicles. Some of these rely on alternative fossil fuels to be used in internal combustion engines. For example, natural gas engines are often regarded as cleaner than diesel engines in terms of NO_x emissions [14], and prior studies have reported that they produce lower tailpipe emissions relative to diesel [15]. However, natural gas engines face notable limitations, including reliability and durability issues, as well as restricted driving range [14]. Additionally, a life cycle assessment conducted by Tong et al. [16] studied the life cycle emissions of alternative fossil fuels to diesel such as gasoline, liquefied natural gas, and compressed natural gas and found that for heavy-duty trucks, these alternative fuels did not improve the lifecycle emissions, with some of the fuels even increasing emissions by up to 13%, primarily due to higher upstream (non-tailpipe) emissions.

Because alternatives based on internal combustion engines inherently produce tailpipe emissions that often fail to offset overall emissions, the transition toward zero-emission heavy-duty vehicles has to involve developing technologies that do not rely on fossil fuels. For this, two electrochemical technologies have emerged as the leading candidates: battery electric vehicles (BEVs) and hydrogen fuel cell vehicles (HFCVs) [17]. BEVs store electrical energy in an onboard battery system that are recharged via connection to the electrical grid. They typically use lithium-ion batteries due to their high power density and longer battery life [18]. HFCVs generate electricity onboard through the electrochemical reaction of hydrogen with oxygen, with polymer electrolyte membrane fuel cells being the most suitable for vehicular applications because of their low operating temperature and high efficiency [19].

It should be acknowledged that, despite being zero-emission during operation, both BEVs and HFCVs may still have emissions associated with their lifecycles, as emissions may arise from electricity generation, hydrogen production, material extraction, and manufacturing processes. Nevertheless, the increasing penetration of renewable energy sources, driven in part by climate change mitigation policies, suggests that these upstream emissions are also on a trajectory toward decarbonization. Under these conditions, both technologies have the potential to enable near-zero-emission operation over their full lifecycles.

Table 2.1 presents a comparison of BEVs and HFCVs, summarized and adapted from Cunanan et al. [17]. This comparison highlights that fuel cell electric vehicles are particularly well-suited to heavy-duty applications, offering several advantages over battery electric vehicles, including higher energy density,

longer driving range, and shorter refueling times. These attributes are especially critical for heavy-duty vehicles, where capacity constraints limit the allowable mass for its power source and where long range and minimal refuelling times are essential for efficient freight transport.

Table 2.1: Comparison between diesel, battery, and hydrogen fuel cell for heavy-duty vehicles adapted from [17]

Criteria	Diesel	Battery	Hydrogen Fuel Cell
Tailpipe Emissions	Yes	No	No
Total Cost	199k – 134k USD	165k – 585k USD	136k – 250k USD
Well-to-tank Efficiency	~86%	~55%	~76%
Tank-to-wheel Efficiency	~23%	~68%	~76%
Fuel Consumption	6.5 miles/gallon	0.5 miles/kWh	5.5 – 9.2 miles/kgH2

Taken together, these considerations indicate that fuel cell-based technologies are the most promising alternative for decarbonizing heavy-duty vehicles.

2.2.2 The PEM Fuel Cell

As noted above, polymer electrolyte membrane fuel cells (PEMFCs) are the most widely used fuel cell technology and are particularly well suited for vehicular applications. This is because of their relatively low operating temperatures compared to other fuel cell technologies (e.g., solid oxide fuel cell), typically in the range of 60-120°C [19], which is compatible with automotive requirements. A vehicle fuel cell system comprises several subsystems, including an air supply system for delivering the oxygen reactant, a hydrogen supply system for delivering the fuel, as well as thermal management and humidification systems [20]. At the core of the system is the fuel cell stack, which consists of multiple single cells electrically connected in series or in parallel to collectively generate the required power output [21]. The fuel cell stack is composed of individual electrochemical cells, and understanding the operation of a single cell is essential. Figure 2-3 illustrates a typical single-cell configuration of a PEM fuel cell showing the different layers, the typical transport of species, and electrochemical reactions.

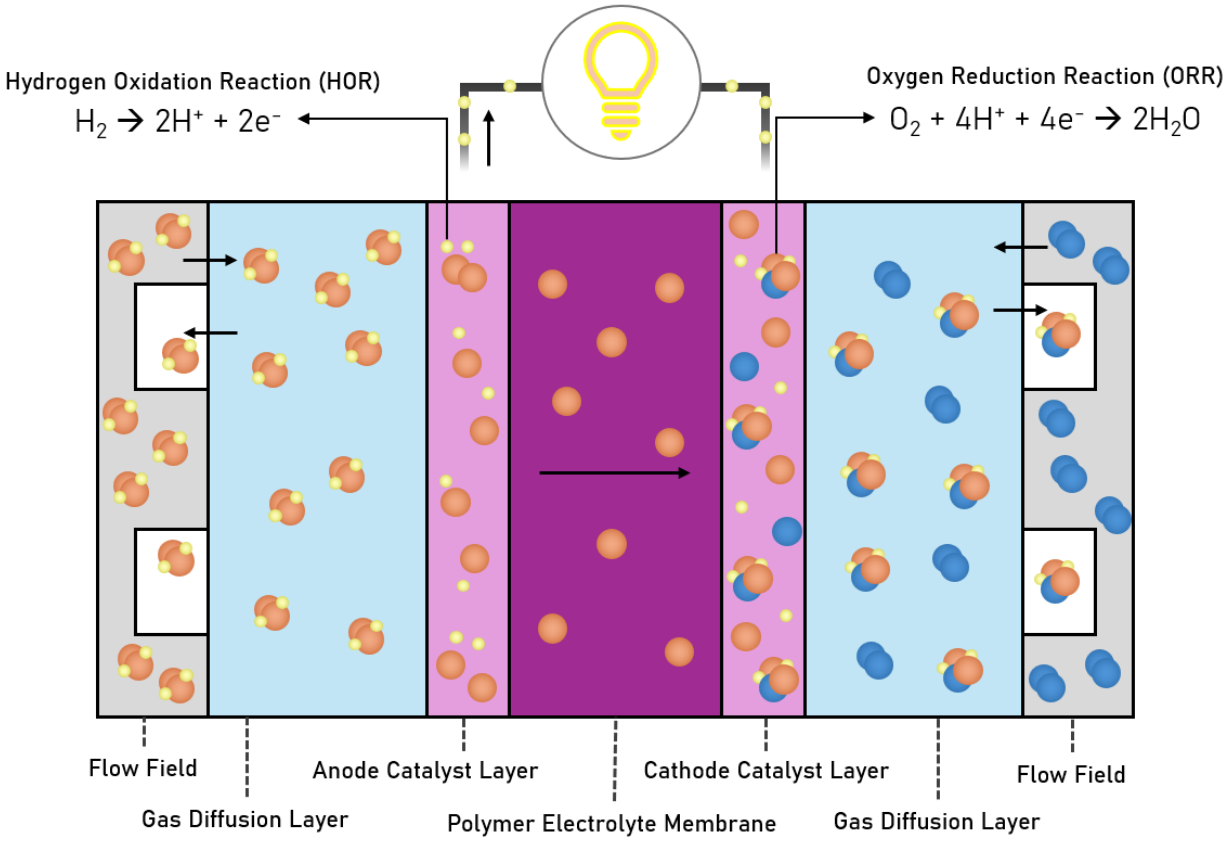


Figure 2-3: Simplified illustration of the components, species, and reactions in a polymer electrolyte membrane fuel cell

Hydrogen enters the anode side through the flow field, passes through the gas diffusion layer, and reaches the anode catalyst layer, where the hydrogen oxidation reaction (HOR) occurs:

$$H_2 \rightleftarrows 2H^+ + 2e^-$$

The electrons produced by this reaction are transported through the electrically conductive components of the cell and external circuit to the cathode, generating electrical power. Simultaneously, the protons are transported through the polymer electrolyte membrane to the cathode side. The polymer electrolyte membrane is the defining component of PEM fuel cells and it serves as a proton-conducting and electronically insulating separator. It is typically composed of a perfluorosulfonic acid (PFSA) polymer, most commonly Nafion [22].

On the cathode side, oxygen (typically supplied through air) enters through the flow field, diffuses through the gas diffusion layer, and reaches the cathode catalyst layer, where it reacts with protons and electrons to form water via the oxygen reduction reaction (ORR):

$$O_2 + 4H^+ + 4e^- \rightleftarrows H_2O$$

The water produced at the cathode may leave the cell as either vapor or liquid, depending on operating conditions, and its management is critical to fuel cell performance, particularly at high current densities. Adequate water content is necessary to maintain membrane conductivity and catalyst activity, while excess liquid water can impede oxygen transport by blocking pores in the gas diffusion layer and catalyst layer [23], [24]. Water and unreacted gases exit the cell through their respective gas diffusion layers and flow fields.

Because water is the only byproduct of the electrochemical reactions, PEM fuel cells do not emit carbon-based pollutants during operation, making them attractive candidates for different zero-emission applications. However, despite these advantages, several challenges continue to limit their widespread deployment. Among these, there is one concern that persists for heavy-duty applications: durability.

2.3 A Solution That Wears Away: The Platinum Degradation Problem

2.3.1 Fuel Cells, Durability, and Degradation

Durability is an important consideration for heavy-duty vehicles, as they operate at significantly higher annual mileage than light-duty vehicles. The annual distance traveled by a Class 8 truck is estimated to be approximately 100,000 km, compared to around 18,000 km for a typical passenger car, which is more than a fivefold difference [25]. This higher utilization along with the load requirements for heavy-duty vehicles are also associated with greater power demands, with heavy-duty vehicles typically requiring power outputs in the range of 150-400 kW, compared to approximately 80-200 kW for light-duty vehicles [25]. Durability therefore represents a major limitation for fuel cell vehicles, especially in heavy-duty applications. The expected lifetime mileage of light-duty fuel cell vehicles is approximately 200,000 km, compared to around 300,000 km for their internal combustion engine counterparts [26]. This difference becomes wider for heavy-duty vehicles, where internal combustion engines can achieve lifetimes of up to 1,200,000 km, while fuel cell vehicles are currently limited to approximately 700,000 km [26]. As a result, the durability-adjusted cost of fuel cell heavy-duty vehicles remains higher than that of diesel-powered vehicles.

These challenges have motivated initiatives aimed at improving fuel cell durability. For example, in the United States, their Department of Energy has established the Million Mile Fuel Cell Truck Consortium (M2FCT) [27], a collaboration among multiple national laboratories focused on extending the lifetime of fuel cell trucks to one million miles (approximately 1.6 million km). The consortium also targets system lifetimes of 25,000 hours by 2030 and 30,000 hours by 2050, alongside improvements in cost and

efficiency. These efforts recognize the importance of durability and also highlights the ongoing commitment to advance fuel cell technologies toward practical deployment in heavy-duty applications.

To address durability limitations, it is important to understand the underlying degradation mechanisms in fuel cells. Patil et al. [28] identified several degradation mechanisms that occur in different components of a fuel cell, summarized in Figure 2-4. These include chemical, thermal, mechanical, and catalytic degradation, which occurs in different forms in different layers.

Chemical degradation includes corrosion of conductive materials (which reduces the conductivity of electrons and ions), poisoning of the hydrogen fuel by contaminants such as carbon monoxide, carbon dioxide, hydrogen sulfide, and ammonia, and chemical membrane degradation by peroxide radicals. Thermal degradation consist of thermal decomposition of various materials under both hot and cold temperature extremes, with high temperatures (>90 °C) causing a reduction in mechanical and electrochemical properties [29] and sub-zero temperatures causing structural damage due to freezing water [30]. Mechanical degradation occurs from the mechanical stress under dynamic operating conditions in the fuel cell, which results in deformation, cracks, and other mechanical and material effects. This deformation is enhanced by the difference in gas pressure between the anode and cathode sides, with the temperature and humidity also affecting the in-plane stress [31].

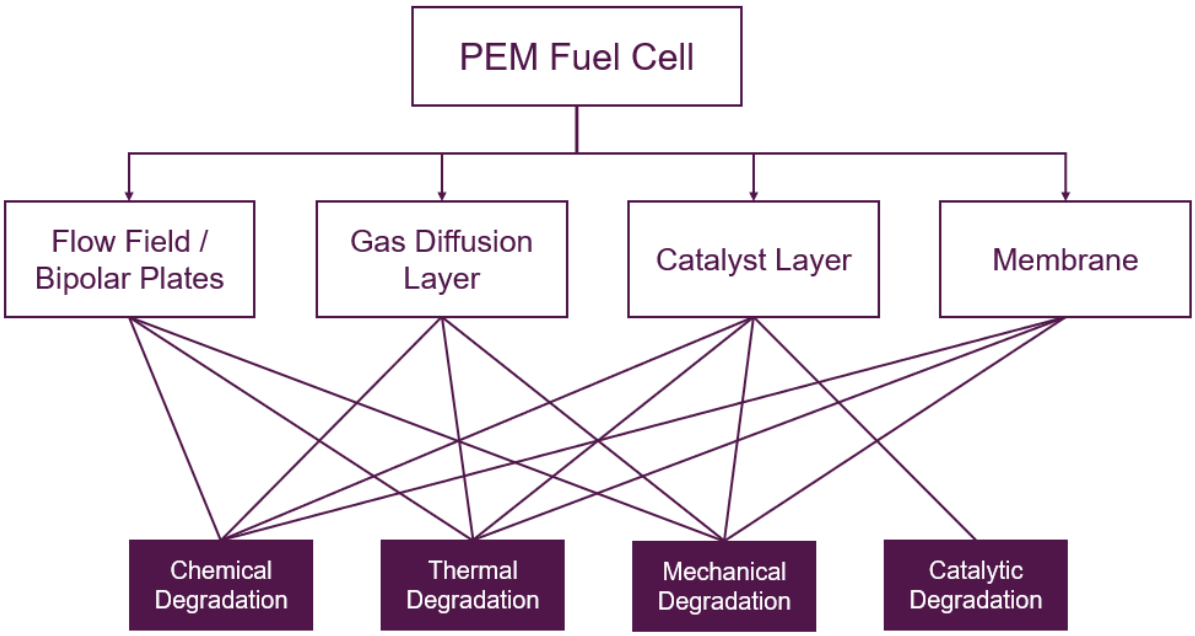


Figure 2-4: Degradation mechanisms in different PEMFC components

Catalyst layer degradation, together with gas diffusion layer (GDL) degradation, has been identified as a major contributor to overall fuel cell performance loss, accounting for more than 90% of total degradation in PEM fuel cells [32]. Among these, one of the most critical degradation mechanisms arises from the instability of the platinum catalyst in the cathode catalyst layer (CCL). Platinum serves as the active material for the sluggish oxygen reduction reaction (ORR), and its degradation therefore has a direct and significant impact on both cell performance and operational lifetime.

Over time, platinum degradation leads to a gradual reduction in the electrochemically active surface area (ECSA), resulting in fewer available catalytic sites for the ORR and a corresponding decline in fuel cell performance [33]. Catalyst layer degradation is primarily driven by several platinum degradation mechanisms, including platinum agglomeration, detachment from the carbon support, and dissolution followed by redeposition or migration to the membrane [34]. These mechanisms alter both the distribution and accessibility of platinum within the CCL.

The loss of ECSA directly contributes to increased kinetic losses due to reduced catalytic activity at the cathode. In addition, platinum degradation can indirectly increase ohmic losses, as preferential platinum migration into the membrane causes more pronounced platinum loss near the membrane and forces protons to travel longer distances to reach active catalytic sites. Mass transport losses are also exacerbated, particularly at high current densities, where oxygen transport becomes limiting. The reduction and redistribution of platinum increase the effective oxygen transport resistance within the catalyst layer, making it more difficult for oxygen to reach remaining active sites through the ionomer phase.

Collectively, these coupled effects demonstrate that platinum degradation is a dominant contributor to PEMFC performance loss. As a result, understanding and modeling platinum degradation mechanisms is critical for accurately predicting fuel cell durability and for guiding the development of more robust and long-lasting cathode catalyst layers.

2.3.2 Platinum Degradation Mechanisms

Several platinum degradation mechanisms have been identified in the literature [35], [36], [37], [38], [39], [40]. In particular, Shao-Horn et al. [41] classified electrochemically active surface area loss into two primary pathways: platinum mass loss and platinum coarsening. Platinum mass loss refers to the removal of platinum from the cathode catalyst layer, whereas platinum coarsening involves an increase in the overall particle size, which reduces the surface-to-volume ratio and therefore the available catalytic surface area. Based on the literature reviewed, the platinum degradation mechanisms are conceptually

organized and summarized in Figure 2-5. Although both pathways ultimately lead to ECSA loss, they originate from distinct physical and electrochemical processes.

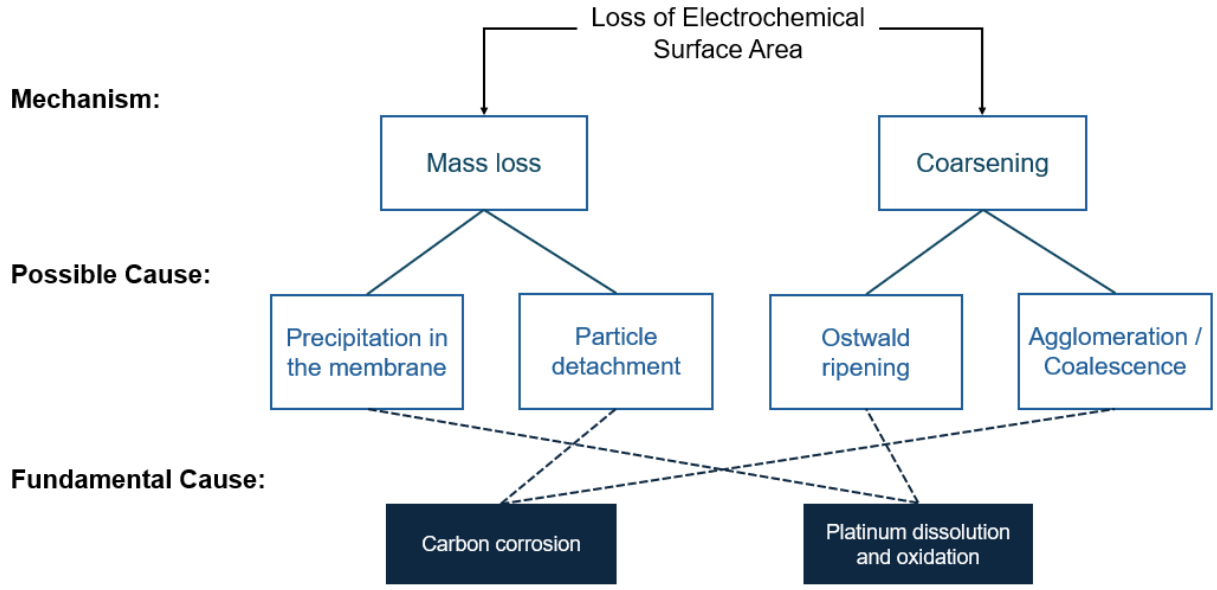


Figure 2-5: Platinum degradation mechanisms

Platinum mass loss is primarily attributed to platinum dissolution and precipitation within the membrane, as well as particle detachment from the carbon support. During operation, platinum can dissolve from the catalyst surface under high potentials, transport into the polymer electrolyte membrane, and then reprecipitate in the membrane. This results in platinum being electrically disconnected from the CCL, effectively making it inactive. Particle detachment, on the other hand, is largely associated with carbon support corrosion, which weakens the anchoring of platinum particles and allows them to detach from the catalyst layer.

Platinum coarsening occurs mainly through Ostwald ripening and particle agglomeration or coalescence. Ostwald ripening involves the preferential dissolution of smaller platinum particles and preferential redeposition onto larger particles due to differences in surface energy. This leads to a progressive shift toward larger particle sizes and a corresponding reduction in ECSA. Agglomeration and coalescence occur when adjacent platinum particles migrate and merge, often facilitated by carbon corrosion, which alters the surface morphology of the support and promotes particle mobility.

Carbon corrosion itself has been identified as a critical catalyst degradation pathway, particularly under high electrode potentials and extended cycling conditions. Meyers and Darling [42] noted that carbon corrosion becomes increasingly significant at elevated potentials but they can be mitigated through

strategies such as improved fuel distribution or nitrogen purging. These observations suggest that carbon corrosion may be alleviated through operational or system-level mitigation strategies.

In contrast, platinum dissolution and oxidation are intrinsic electrochemical side reactions that are more difficult to suppress through external control. Because these processes are strongly coupled to electrode potential and local reaction conditions, they remain a persistent issue and a central focus of platinum degradation and fuel cell durability studies. Understanding and accurately modeling these mechanisms is therefore important for predicting long-term fuel cell performance and guiding the design of more durable catalyst layers.

2.4 Physics-Based Modeling of Platinum Catalyst Dissolution and Oxidation

Early efforts on modeling platinum degradation often relied on empirical approaches to reproduce experimentally observed trends in electrochemically active surface area loss [43], [44], which served as useful black-box tools for degradation prediction. In recent years, data-driven models have also emerged as a helpful approach in offering system-level analyses that enable rapid predictions for the fuel cell lifetime as well as real-time applications [33], [45], [46]. Although these approaches are valuable for forecasting performance degradation, they lack the physical detail necessary to isolate individual catalyst degradation mechanisms and reactions as well as understand their underlying causes. To address these limitations, numerous studies have developed physics-based models and formulations. These models explicitly resolve particle size evolution by coupling electrochemical reaction dynamics and charge and species transport with realistic operating conditions. Over the past two decades, these physics-based models have provided increasingly detailed insight into the spatial and temporal evolution of platinum degradation and its interaction with other phenomena occurring within the fuel cell.

2.4.1 Overview of Platinum Degradation Mechanisms

As discussed, platinum loss through precipitation in the membrane and platinum coarsening through Ostwald ripening involve the dissolution of metallic platinum into ionic species, which is usually described as a potential-dependent reaction [47], [48]. At higher electrode potentials, a surface oxide layer is also believed to form on the platinum surface through its interactions with water and oxygen in the cathode, although the contribution of water in platinum oxidation is dominant at higher humidity [49]. This oxide layer acts to passivate the platinum surface, temporarily suppressing further dissolution [50]. However, the oxide layer is also believed to chemically dissolve into platinum ions [51]. The most commonly proposed electrochemical reactions in the literature describing platinum dissolution and oxidation are shown in Figure 2-6 and are defined as follows:

$$\mathrm{Pt} \rightleftarrows \mathrm{Pt}^{2+} + 2\mathrm{e}^{-} \qquad E^0 = 1.188\,V \qquad (1)$$

$$\mathrm{Pt} + \mathrm{H_2O} \rightleftarrows \mathrm{PtO} + 2\mathrm{H}^{+} + 2\mathrm{e}^{-} \qquad E^0 = 0.98\,V \qquad (2)$$

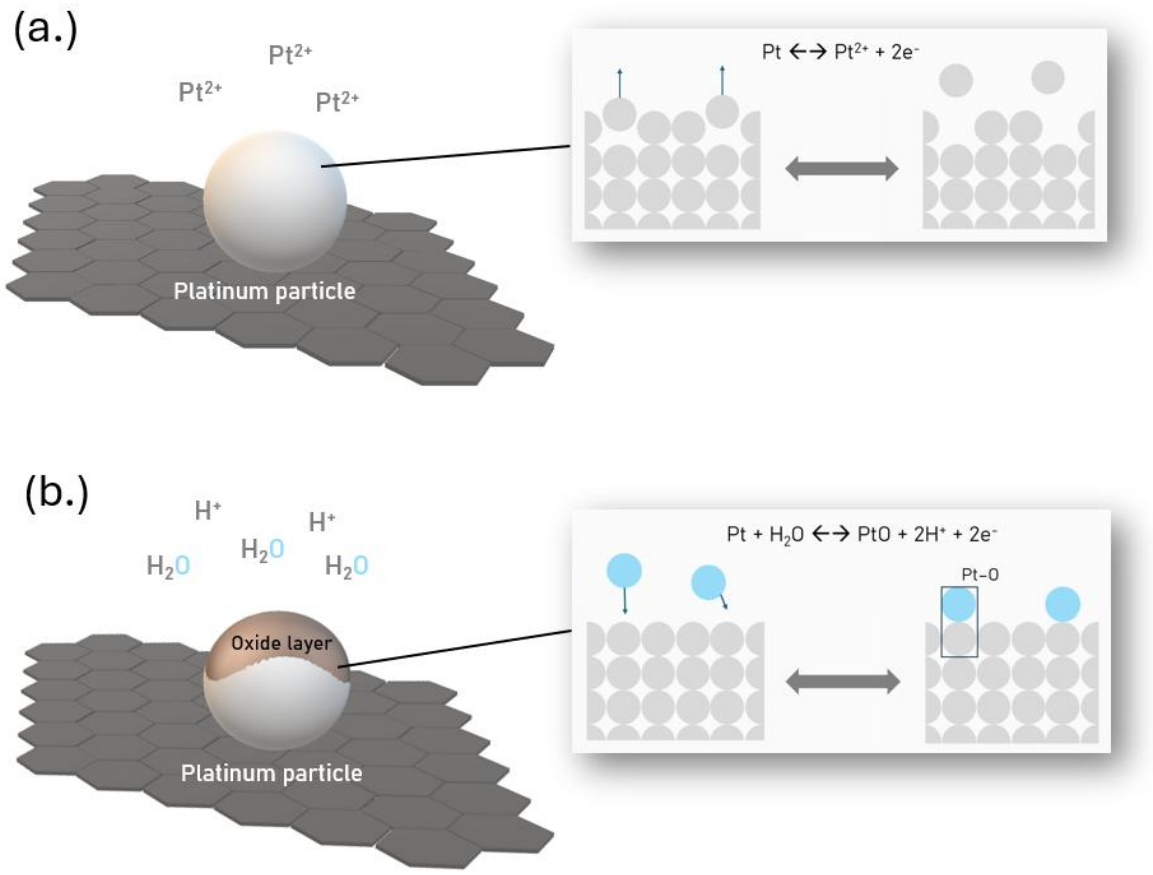


Figure 2-6: (a.) Electrochemical dissolution of platinum and (b.) electrochemical oxide formation on the platinum surface

The parallel reactions of platinum dissolution into ionic species and the formation of surface platinum oxides have long been recognized as key reactions that govern catalyst degradation in PEMFCs [48], [52], [53]. Due to the nanoscale nature of the platinum particles, these reactions exhibit a strong dependence on particle size, where smaller particles tend to dissolve and oxidize more rapidly due to their higher surface energy [53], [54], [55], [56]. Figure 2-7 illustrates this size dependence by presenting modified Pourbaix diagrams [57], which map the regions with thermodynamic stability of different platinum phases as a function of potential and pH. As shown, the equilibrium potential at which metallic platinum remains stable shifts to lower values as the particle size decreases. Hence, the stability of nanoscale platinum

particles changes under realistic PEMFC operating conditions, where local potential and pH fluctuate during load cycling, providing a fundamental explanation for the size-dependent dissolution behavior observed experimentally. As such, the physical modeling of these mechanisms involves kinetic equations (typically Butler-Volmer rate laws for electrochemical reactions) and the Gibbs-Thomson equation to account for size effects. These formulations enable a quantitative description of the platinum reactions as functions of potential and particle radius. By coupling these equations, physics-based models capture the dynamic evolution of the platinum surface area and its dependence on the potential load profile of the fuel cell, providing a direct link between the nanoscale degradation phenomena and fuel cell performance loss.

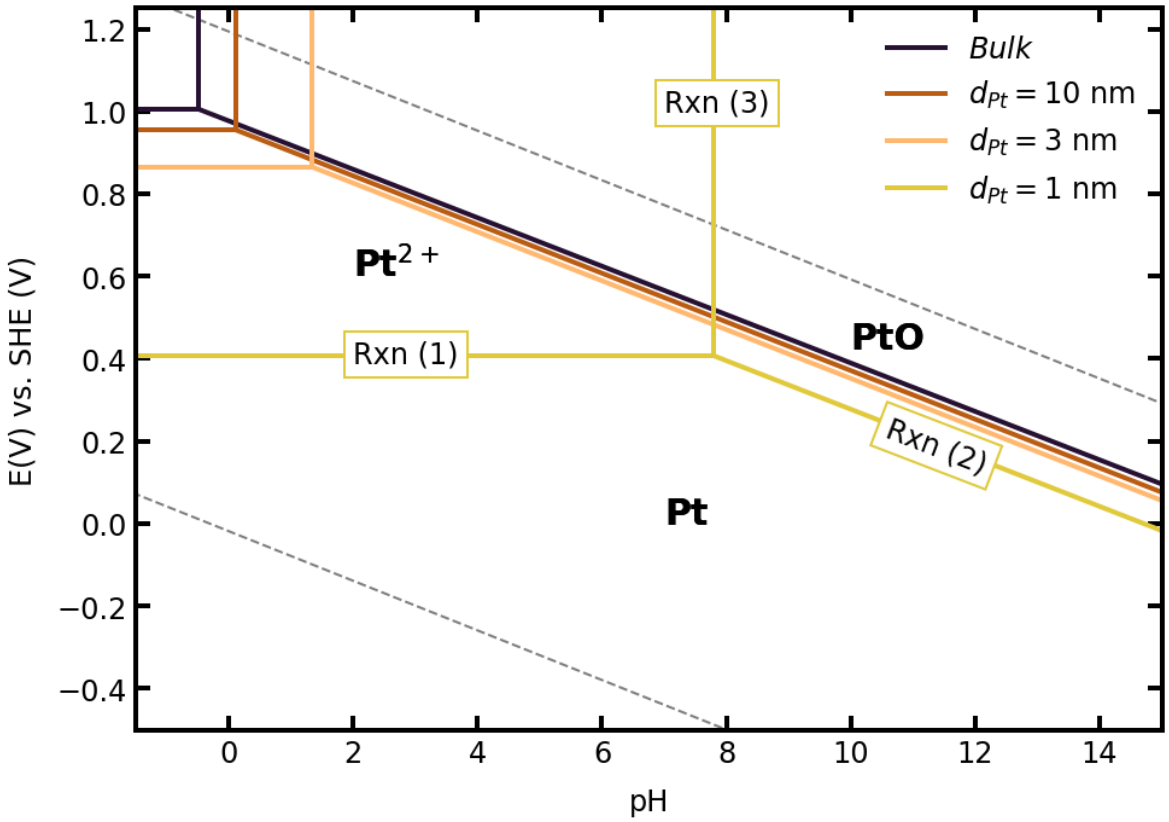


Figure 2-7: Modified Pourbaix diagram of platinum for bulk (planar surface) and platinum nanoparticles of different diameters (in Pt^{2+} concentration of 10^{-6} M) using data from Tang et al. [57], showing the size-dependence of platinum stability

There remains an ongoing debate regarding the dominant platinum dissolution pathway. Specifically, it is unclear whether dissolution predominantly occurs via direct electrochemical dissolution of metallic platinum as in Equation (1) or through the chemical dissolution of formed platinum oxides (e.g., PtO), as shown in Equation (3).

$$PtO + 2H^+ \rightleftarrows Pt^{2+} + H_2O \quad (3)$$

Some studies argue in favor of the electrochemical Pt dissolution being the only significant pathway [58], [59], citing experimental evidence showing that dissolution significantly decreases once the platinum surface is fully covered in oxide [60]. Others argue that the chemical oxide dissolution plays a non-negligible role, particularly under specific conditions, and should not be disregarded [61], [62], as supported by observations of weaker dependence on potential for platinum ion concentration in experimental studies [63], [64].

This review therefore focuses on physics-based models describing platinum dissolution and oxidation, which represent key pathways of catalyst degradation in PEM fuel cells. Purely empirical or data-driven ECSA loss models, atomistic studies of platinum dissolution such as density functional theory, and experimental investigations without a modeling component are outside the scope of this review. This is intended to provide a focused and coherent assessment of physics-based degradation modeling approaches. Among the many modeling efforts proposed, we have identified three frameworks that emerged as the most widely adopted for modeling platinum dissolution and oxidation: the Darling-Meyers model, the Holby-Morgan model, and the Rinaldo-Stumper-Eikerling model. The following sections introduce these foundational models and highlight key studies that have applied or extended them across various contexts.

2.4.2 Darling-Meyers Model

2.4.2.1 Foundational Studies

In 2003, Darling and Meyers [51] proposed Butler-Volmer-type expressions for Equation (1) and Equation (2). The equilibrium potentials of the reactions were expressed as size-dependent terms based on the Kelvin (Gibbs-Thomson) equation. The authors acknowledge that the terms neglect the effect of different surface planes in very small particles, as well as the interactions between the surface and the electrochemical double layer. A third reaction to account for the chemical dissolution of platinum oxide (Equation (3)) was also proposed. The rates of these reactions were coupled with equations for the transient evolution of platinum particle radius, oxide coverage, and dissolved platinum ion concentration, each treated as a single lumped value. Together, these relationships formed a system of differential equations that could be solved transiently. Despite being a lumped model, it was able to offer key insights into platinum behavior during potential sweeps, such as a rapid rise in Pt ion concentration up to 1.1 V, beyond which full surface coverage by a monolayer oxide slows the dissolution rate.

The same authors later extended their model to a one-dimensional full PEMFC domain [65], incorporating a bimodal particle size distribution to simulate platinum ion transport and more complete dissolution dynamics. This extension enabled spatial variation in Pt ion concentration and explicit modeling of platinum migration within the cell. The results showed that potentiostatic operation at an intermediate potential of 1.05 V led to a higher dissolution rate than at either 0.87 V or 1.2 V, as can be seen in Figure 2-8, suggesting the existence of a potential window where dissolution is accelerated, between startup and shutdown. Furthermore, voltage cycling between 1.2 V and 0.87 V caused more pronounced platinum loss than the potentiostatic operation at any of the voltages.

As the first of its kind, the model made a pioneering contribution to physics-based degradation modeling in PEM fuel cells and laid the foundation for subsequent multi-dimensional and multi-scale degradation models. It marked the beginning of integrating kinetic modeling, particularly kinetic descriptions of electrochemical platinum degradation, into the degradation studies in literature. By linking reaction kinetics, platinum particle characteristics, and local conditions within the catalyst layer, the model connected platinum dissolution and oxidation dynamics with a cell-level framework capable of predicting surface area loss.

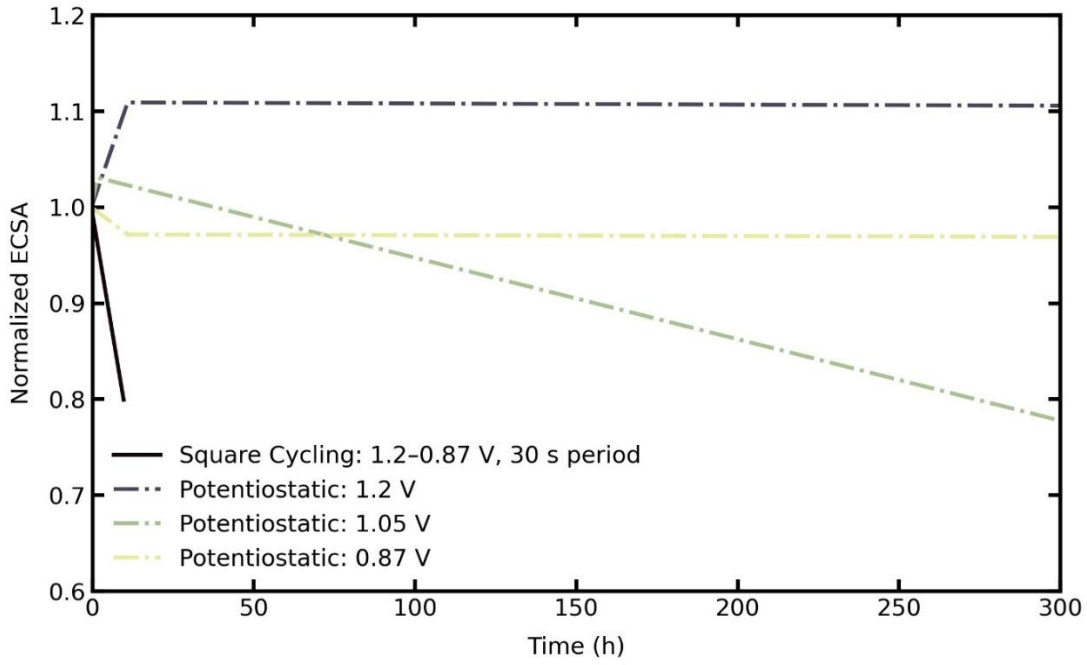


Figure 2-8: Data from Darling and Meyers[65] comparing simulated ECSA losses for potentiostatic holds of 1.2, 1.05, and 0.87 V and for square-wave cycling from 0.87 V to 1.2 V with 30 s period

2.4.2.2 Model Overview

The following rate equations were proposed for reactions described in (1), (2), and (3), respectively:

$$R_1 = k_1\theta_{vac}\left[exp\left(\frac{\alpha_{a,1}n_1F}{RT}(\phi_s - \phi_l - U_1(r))\right) - \frac{c_{Pt^{2+}}}{c_{Pt^{2+},ref}}\exp\left(-\frac{\alpha_{c,1}n_1F}{RT}(\phi_s - \phi_l - U_1(r))\right)\right] \tag{4}$$

$$R_2 = k_2\left[exp\left(-\frac{\omega\theta}{RT}\right)exp\left(\frac{\alpha_{a,2}n_2F}{RT}(\phi_s - \phi_l - U_2(r))\right) - \theta\left(\frac{c_{H^+}}{c_{H^+,ref}}\right)^2\exp\left(-\frac{\alpha_{c,2}n_2F}{RT}(\phi_s - \phi_l - U_2(r))\right)\right] \tag{5}$$

$$R_3 = k_3\left(\theta c_{H^+}^2 - \frac{c_{Pt^{2+}}}{exp\left[\frac{F}{RT}(n_1U_1(r) - n_2U_2(r))\right]}\right) \tag{6}$$

$U_1(r)$ and $U_2(r)$ are size-dependent equilibrium potentials for reactions 1 and 2, defined as:

$$U_1(r) = U_1^{\theta} - \frac{\sigma_{Pt}M_{Pt}}{2r\rho_{Pt}F} \tag{7}$$

$$U_2(r) = U_2^{\theta} + \left(\Delta\mu_{PtO}^0 + \frac{\sigma_{PtO}M_{PtO}}{\rho_{PtO}} - \frac{\sigma_{Pt}M_{Pt}}{\rho_{Pt}}\right)\frac{1}{2Fr} \tag{8}$$

The change in particle radius, platinum oxide coverage, and ion concentration are expressed in terms of the rate equations as:

$$\frac{dr}{dt} = -\frac{M_{Pt}}{\rho_{Pt}}(R_1 + R_2) \tag{9}$$

*** **An important note**: Equation (9) contains the original formulation of Darling and Meyers for the particle radius evolution, which is shown to be dependent on the electrochemical dissolution and oxide formation of platinum (Reactions (1) and (2)). However, as oxide formation does not directly remove platinum mass from the particle and is therefore unlikely to contribute to a reduction in particle radius, most subsequent studies employing the Darling-Meyers model have either replaced R_2 with R_3 (chemical dissolution) or omitted R_2 entirely, depending on the assumed role of chemical dissolution on radius change.

$$\frac{d\theta}{dt} = \frac{(R_2 - R_3)}{\Gamma} - \left(\frac{2\theta}{r}\right)\frac{dr}{dt} \tag{10}$$

$$\varepsilon \frac{dc_{Pt^{2+}}}{dt} = 4\pi r^2 \bar{\bar{N}}(R_1 + R_3) \quad (11)$$

The fitting parameters of the model include the reaction rate constants, the transfer coefficient of the electrochemical reactions, and the $\Delta\mu^0_{PtO}$. Given the pioneering nature of these studies, the authors fitted several parameters: k_1, k_2, $\alpha_{c,1}$, $\alpha_{c,2}$, and $\Delta\mu^0_{PtO}$, while they assumed the following parameters: $\alpha_{a,1}$, $\alpha_{a,2}$, k_3

2.4.2.3 Model Adoption in Subsequent Studies

As the first study to include additional mechanisms, Bi and Fuller [58] extended the Darling-Meyers model by incorporating the platinum precipitation mechanism in the membrane from their earlier work [66] into a one-dimensional domain spanning the anode, membrane, and cathode. They implemented a bimodal particle size distribution, and platinum ion transport was assumed to occur solely through diffusion, neglecting migration effects. The model successfully captured electrochemical Ostwald ripening behaviors. However, it did not accurately reproduce experimental degradation rates, suggesting the need to include additional mechanisms to be modeled, such as cluster formation and nanoparticle coarsening.

Zhang et al. [50] applied the same model in a 1D domain to study the effect of the lower potential limit (LPL) on dissolution. Their work defined the potential window where dissolution is accelerated. They identified three regions: (1) high redeposition at LPL < 0.7 V, where dissolution slows due to favorable redeposition, (2) passivation at LPL > 1.0 V, where complete oxide coverage limits dissolution, and (3) an intermediate region (0.7 V < LPL < 0.9 V), where low redeposition and partial oxide coverage lead to the peak of the dissolution rate. These potentials are shown in Figure 2-9. This analysis provided one of the earliest model-based analyses on the effects of cycling conditions on platinum loss, offering valuable insight into the development of durability testing protocols.

On a more practical application, Thangavelautham and Dubowsky [67] adapted the model for degradation analysis in field sensor fuel cells, incorporating relative humidity and particle migration effects. Their results showed that migration strongly affects catalyst lifetime between 0.85-0.75 V, though its effect diminishes at higher voltages due to reduced current densities.

Schneider et al. [68] utilized the model to incorporate dissolution and oxidation into a full lumped model of catalyst degradation which also includes carbon corrosion and place-exchange mechanism. The model was validated against experimental data across various operating conditions and reliably predicted

electrochemical surface area loss within that range. Their work stands out for its broad integration of degradation mechanisms with the Darling-Meyers model, albeit within a lumped formulation.

Kregar and Katrašnik [69] critically analyzed electrochemical Ostwald ripening models, using the Darling-Meyers model within a lumped (0D) domain, and demonstrated how its behavior can deviate from classical diffusion-driven Ostwald ripening. Specifically, they showed that at high voltages, these models predict exponential particle growth driven by platinum-ion oversaturation. Their results emphasize the need for improved ion transport modeling and more accurate treatment at high voltages. Nevertheless, the same authors later applied a Darling-Meyers-type model with similar assumptions for platinum dissolution in a larger system-level degradation framework for high-temperature PEM fuel cells [70]. The model incorporated a 3D hybrid approach combining analytical and numerical solutions [71] to simulate a variety of degradation mechanisms, such as carbon corrosion and platinum agglomeration and detachment, but kept some assumptions the same, such as constant platinum ion concentration.

Another practical application was presented by Baroody and Kjeang [72], who implemented a lumped Darling-Meyers-type model with a particle size distribution to first examine the effects of voltage sweep rate and upper potential limit, alongside a parametric study of reaction rate constants. Then, the model was used to predict platinum degradation under a realistic drive cycle, utilizing the model for real-world cycling behavior.

More recently, Darling-Meyers-type models have been applied in various settings: by Shojayian and Kjeang [73] in a zero-dimensional catalyst degradation model tested under transit bus operation, by Haslinger and Lauer [74] who coupled a one-dimensional degradation model with a dynamic three-dimensional CFD model of an industrial PEMFC, by Fu et al. [75] who integrated the model to analyze and propose an energy management strategy for minimizing ECSA loss, and by Touil et al. [76] in a lumped degradation model integrated into a multi-physics, stack-level framework validated against AST protocols as well as the New European Driving Cycle dataset,.

As mentioned above, the Darling-Meyers model requires a suite of input values which are usually treated as fitting parameters. Table 2.2 summarizes the parameter sets used in selected works, showing how the fitting parameters vary across different contexts. These variations reflect differences in experimental conditions, parameter calibration approaches, and model scope. More recent studies have extended the original formulation by redefining certain parameters, particularly the rate constants, as functions of operating conditions such as temperature and relative humidity, in an attempt to reduce the number of free parameters required. Additionally, there has been a growing emphasis on conducting parametric studies

[68], [72], [76], which enhances model robustness and provides insight into the sensitivity of platinum degradation behavior to fitting parameters and operating conditions.

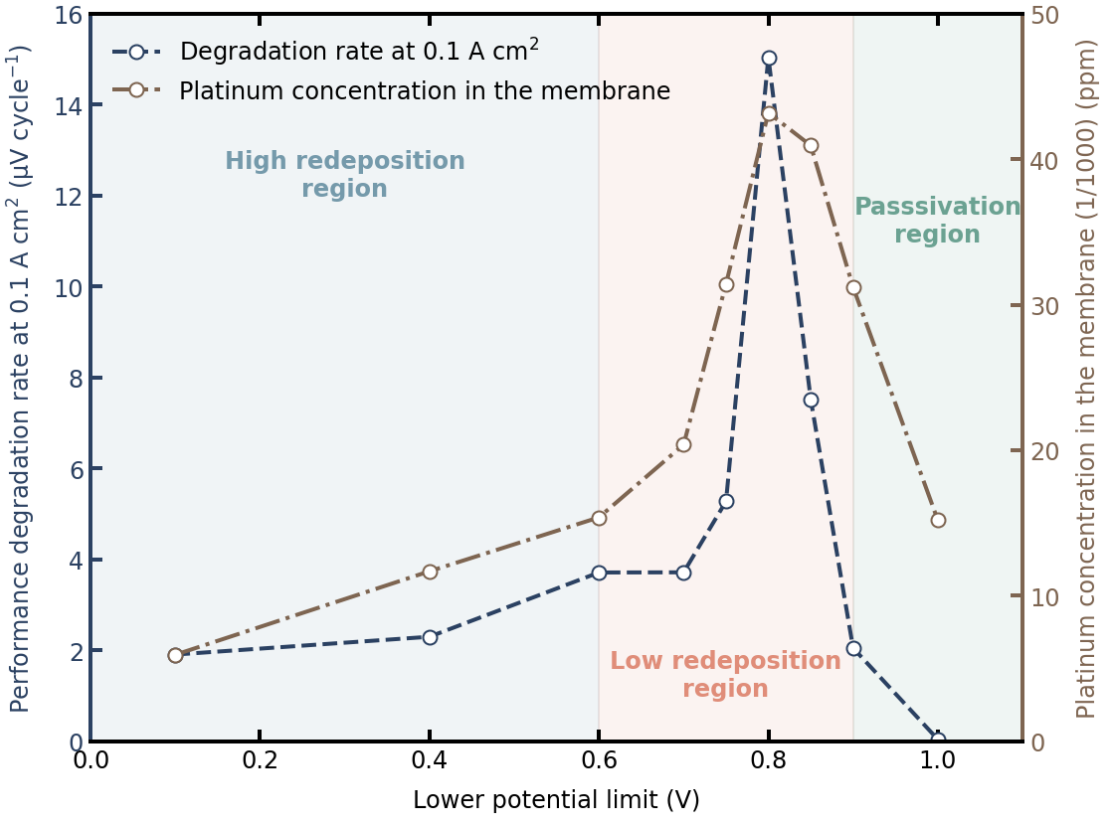


Figure 2-9: Performance degradation rate and platinum concentration in the membrane obtained at different LPL with UPL=1.35 from Zhang et al. [50] showing three distinct regions of different dissolution behaviour from the interactions between the dissolution and oxidation reactions

Table 2.2: Values of the fitted and assumed parameters taken from select publications using Darling-Meyers model

Literature	Operating Conditions	Voltage Conditions	k_1 [mol m^2 s^{-1}]	k_2 [mol m^2 s^{-1}]	k_3 [mol m^2 s^{-1}]	$\alpha_{a,1}$	$\alpha_{c,1}$	$\alpha_{a,2}$	$\alpha_{c,2}$	$\Delta\mu^0_{PtO}$ [kJ mol^{-1}]
Darling and Meyers, 2003 [51] and 2005 [65]	T = 65 °C P = 100 kPa	Potentiostatic and Square wave cycle [0.87 to 1.2 V, varied periods]	$3.40 \cdot 10^{-9}$	$1.36 \cdot 10^{-7}$	$3.20 \cdot 10^{-20}$	0.5	0.5	0.35	0.15	-42.3
Bi and Fuller, 2008 [58]	T = 60 °C Fully humidified	Square wave cycle [0.87 to 1.2 V, 60 s period]	$3.00 \cdot 10^{-6}$	$7.00 \cdot 10^{-6}$	Reaction (3) not considered	0.5	0.5	0.4	0.1	-38.0
Zhang et al., 2013 [50]	T = 60 °C RH = 100%	Square wave cycle [1.35 V UPL, LPL varied, 4 s period]	$3.00 \cdot 10^{-8}$	$6.00 \cdot 10^{-6}$	$3.20 \cdot 10^{-20}$	0.5	0.5	0.35	0.15	Not given
Schneider et al., 2019 [68]	Varied T and RH (part of analysis)	Varied shapes and parameters (part of analysis)	Function of RH	$1.40 \cdot 10^{-7}$	$3.20 \cdot 10^{-20}$	0.3	0.5	0.35	0.5	-42.3
Baroody and Kjeang, 2021 [72]	T = 80 °C	Triangular, varied parameters (part of analysis)	Varied (part of analysis) Included forward and backward rate constants for Reaction (1)	Varied (part of analysis) Included forward and backward reaction rate constants for Reaction (2)	Varied (part of analysis) Simplified reaction (3) rate equation	0.5	0.5	0.5	0.5	Not given
Toiul et al., 2025 [76]	Varied T and RH (part of analysis)	Varied shapes and parameters (part of analysis)	Function of RH and T	Function of RH and T	$1.00 \cdot 10^{-11}$	0.5	0.5	0.5	0.5	Not given

2.4.3 Holby-Morgan Model

2.4.3.1 Foundational Studies

Six years after Darling and Meyers, Holby and Morgan also presented pioneering contributions to platinum degradation modeling [59], [77] . In essence, they proposed a detailed extension of the Darling-Meyers model. In their framework, they expressed the rate constants and equilibrium potentials in terms of interfacial thermodynamic properties and their dependencies on operating conditions. This approach is more rigorous and enables a deeper physical interpretation of degradation mechanisms as a result, but it also introduces a larger number of parameters that must be determined or fitted, including dependencies on variables such as pH. Their work further emphasized the critical influence of the platinum particle size distribution on overall catalyst stability. They were one of the first models to differentiate between mechanisms of platinum coarsening and mass loss, allowing for a more accurate representation of how each mechanism independently contributes to electrochemical surface area loss.

In their first work [59], they introduced a new model and analyzed the effect of particle size distribution (PSD), emphasizing the Gibbs-Thomson effect on stability. They showed that increasing particle size from 2-3 nm to 4-5 nm can significantly reduce surface area loss, despite starting with less initial surface area, as can be seen in Figure 2-10a and Figure 2-10b. The model included a membrane band sink to account for platinum loss to the membrane and neglected platinum oxide dissolution as a dissolution pathway. They further concluded that having a platinum sink will shift the dominant ECSA loss mechanism from coarsening (Ostwald ripening) to platinum mass loss. The second study [77] extended the PSD analysis by comparing different PSD shapes, shown in Figure 2-10c and Figure 2-10d. It found that narrower distributions, while initially more stable, can lead to poorer long-term stability if they lack a large-particle tail, particularly when mass loss through the membrane sink dominates over coarsening. They also observed that hydrogen crossover influences degradation by shifting the effective platinum sink location, with sinks closer to the membrane interface increasing its effect on surface area loss.

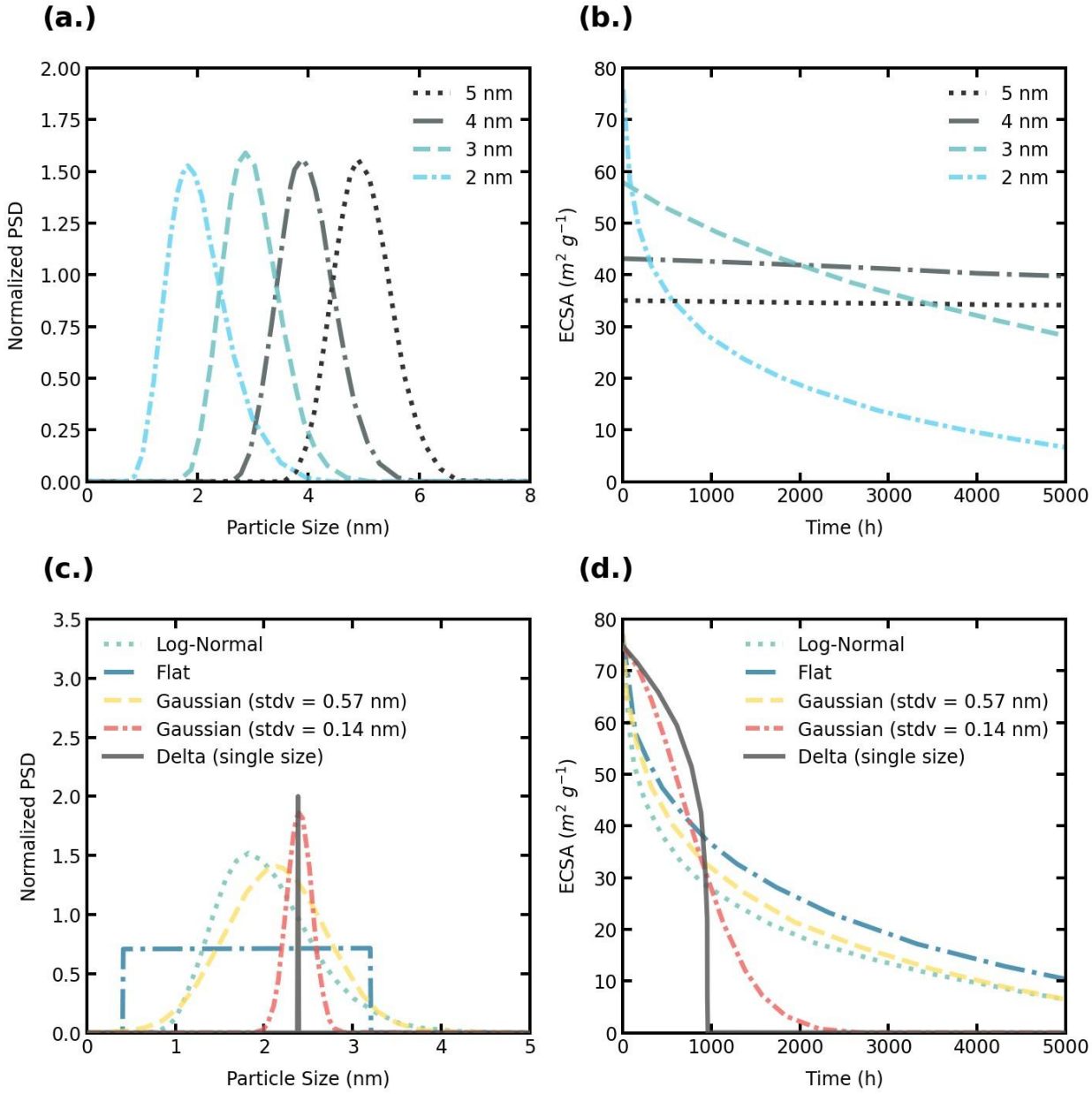


Figure 2-10: Effects of platinum particle size distribution (PSD) on degradation behavior in the Holby and Morgan models. Panels (a) and (b), adapted from Holby et al. [59], show the influence of different mean PSD sizes, with (a) the initial PSD profiles and (b) the corresponding electrochemically active surface area (ECSA) loss for mean particle sizes of 2, 3, 4, and 5 nm. Panels (c) and (d), adapted from Holby and Morgan [77], shows the effects of different PSD distribution types, with (c) the initial PSD profiles and (d) the corresponding ECSA loss for log-normal, flat, Gaussian (narrow and wide), and delta (single-size) distributions.

2.4.3.2 Model Overview

The following rate equations were proposed for reactions described in (1) and (2):

$$R_1 = \nu_1 exp\left[\frac{-\bar{H}_{1,fit}}{RT}\right](1 - min(\theta, 1))\Gamma\left[exp\left(\frac{-(1-\beta_1)n_1F}{RT}\left(U_{eq} - V - \frac{2\Omega_{Pt}\gamma_{eff}(\theta,V,T)}{rn_1F}\right)\right)\right.$$
$$\left. - c_{Pt^{2+}}\frac{\nu_2}{\nu_1}exp\left(\frac{-\beta_1 n_1F}{RT}\left(U_{eq} - V - \frac{2\Omega_{Pt}\gamma_{eff}(\theta,V,T)}{rn_1F}\right)\right)\right] \quad (12)$$

$$R_2 = \nu_1^*\,\Gamma\left(1 - \frac{\theta}{2}\right)exp\left[-\frac{1}{RT}\left(\bar{H}_{2,fit} + \lambda\theta + (1-\beta_2)\left(n_2FU_{fit} + \omega\theta - n_2FV\right)\right)\right]$$
$$- \nu_2^*\Gamma\left(\frac{\theta}{2}\right)(10^{-pH})^2 exp\left[-\frac{1}{RT}\left(\bar{H}_{2,fit} + \lambda\theta - \beta_2\left(n_2FU_{fit} + \omega\theta - n_2FV\right)\right)\right] \quad (13)$$

where ν_1^* and ν_2^* are expressed as:

$$\nu_1^* = \nu_{1,ox} exp\left[\frac{\bar{S}'_{PtH_2O} - \bar{S}'_{H_2O}}{R}\right] \quad (14)$$

$$\nu_2^* = \nu_{2,ox} exp\left[\frac{\bar{S}'_{PtH_2O}}{R}\right] \quad (15)$$

In the second work [77], the authors set ν_1^* and ν_2^* as fitting parameters.

The effective surface energy, γ_{eff}, is given by:

$$\gamma_{eff}(\theta,V,T) = \gamma_{Pt}$$
$$+ \Gamma\theta RT\left(log\left(\frac{\nu_2^*}{\nu_1^*}\right) + log\left(\frac{\theta}{2}\right) + \frac{(2-\theta)}{\theta}log\left(1 - \frac{\theta}{2}\right) + log(10^{-2pH})\right.$$
$$\left. + \frac{n_2F}{RT}\left(U_{fit} - V\right) + \frac{\omega\theta}{RT}\right) \quad (16)$$

The radius and oxide coverage evolution are given by:

$$2\frac{dr}{dt} = -\Omega_{Pt}(R_1 + R_2) \quad (17)$$

*** **An important note**: Similar to the Darling-Meyers formulation, the original Holby-Morgan model expresses particle radius evolution as a function of both electrochemical dissolution and oxide formation rates (Reactions (1) and (2)) in Equation (17). However, because oxide formation does not directly remove metallic

platinum from the particle, subsequent studies employing the Holby-Morgan model have omitted the contribution of R_2 from the radius evolution equation.

$$\frac{d\theta}{dt} = \frac{R_2}{\Gamma} - \left(\frac{2\theta}{r}\right)\frac{dr}{dt} \tag{18}$$

Note that the platinum ion transport was modelled using Fick's law of diffusion, with the following boundary condition applied in the electrolyte/Pt interface ($x = 0$), as the cathode was modelled as zero-dimensional:

$$\frac{dc_{Pt^{2+}}(x=0)}{dt} = \frac{1}{\xi}\sum_i \frac{2\pi r_i^2 N_i R_{1,i}}{\Delta \mathrm{v}} \tag{19}$$

This summation is performed over discrete particle size classes, i

The authors identified the following parameters for fitting: ν_1, ν_2, ν_1^*, ν_2^*, $\overline{H}_{1,fit}$, $\overline{H}_{2,fit}$, U_{fit}, ω, λ, β_1 and β_2, though some of these parameters were assumed in order to reduce the number of fitting parameters.

2.4.3.3 Model Adoption in Subsequent Studies

Li et al. [78] developed a one-dimensional model based on this framework to study platinum degradation. Their results revealed significantly greater surface area loss near the membrane compared to the rest of the catalyst layer, due to platinum migration into the membrane, making it one of the first modeling studies to focus on non-uniform degradation within the CCL. They also identified a critical CCL thickness below which degradation accelerates, highlighting the challenges of ultrathin catalyst layer designs. Later, Li and Wang [79] extended this work by coupling the 1D degradation model with an M2 fuel cell performance model. Their study captured 2D non-uniformities in local current density and ECSA loss, showing that degradation increases micro-scale oxygen transport resistance and thereby impacts overall performance. This was among the earliest efforts to directly couple degradation and performance modeling and analyze their interdependence.

Zheng et al. [80] applied the Holby-Morgan model to study platinum degradation under triangular, square, and trapezoidal voltage waveforms. They found that overall ECSA loss and the ratio of mass loss to Ostwald ripening is highest with trapezoidal wave, followed by square wave, and then by triangular wave. They also showed that longer dwell times at high potentials (UPL) promote greater mass loss in square and trapezoidal waveforms, while faster cycling enhances Ostwald ripening due to increased cycling-induced instability. These findings provide valuable insight into how different voltage profiles

influence the balance between degradation mechanisms, offering a basis for tailoring potential cycling in durability studies.

Zheng et al. [81] used the model to explore degradation mitigation strategies, demonstrating that a 3-layer ePTFE-reinforced membrane, designed to reduce gas crossover, can shift the platinum band away from the PEM-CCL interface and effectively reduce mass loss. They also showed improved durability with reduced Pt ion diffusivity in the ionomer. The study is valuable for highlighting the sensitivity of degradation to waveform shapes and cycling parameters.

Several studies by Kovtunenko et al. [82], [83], [84], [85], [86], [87], [88] employed Holby-Morgan-type models for platinum dissolution and oxidation. Some of these works [84], [85], [86] contributed novel insights to the utility of the Holby-Morgan model, including sensitivity analyses of the numerous variables in the model and an exploration of the parameter ranges and operating conditions under which the model remains valid. These efforts help clarify the model's robustness and guide its more reliable application.

Goswami et al. [89] developed a coupled degradation-performance model to investigate how platinum degradation affects PEMFC performance. They identified distinct regions in the catalyst layer that exhibit coarsening, stable shrinking, and unstable shrinking behavior. The study highlighted the complex interplay between operating conditions, species transport, and local particle dynamics, showing how these factors collectively influence ECSA loss and degradation during fuel cell operation.

Recent literature has increasingly applied the Holby-Morgan model in various degradation studies. Zhu et al. [90] used the model for a study mostly focused on the behaviour of platinum precipitation in the membrane. Sheng et al. [91] incorporated the model into an optimization framework to assess voltage conditions and proposed energy management strategies to minimize degradation. Dong et al. [92] applied the model to evaluate how gradient CCL structures influence platinum loss, identifying optimal designs that balance performance and durability. Huang et al. [93] incorporated the model as a 1D sub-model within a 3D fuel cell framework to study the effects of voltage parameters, Pt loadings, and operating conditions with 3D spatial resolution. Hu et al. [94] applied the model to a 2D domain coupled with a performance model to analyze spatial heterogeneities in degradation and performance losses.

Similar to the Darling-Meyers model, subsequent studies have applied the Holby-Morgan model under various operating and voltage conditions, each using different sets of fitted parameters. Table 2.3 summarizes these parameter sets from selected works, illustrating how the fitting values vary across different contexts. Notably, the range of parameter values reported for the Holby-Morgan model is narrower than that for the Darling-Meyers model. This could be attributed to two main reasons. First, the

larger number of parameters in the Holby-Morgan model introduces stronger interdependencies among them, which constrains the range of feasible values. Second, the parameter-fitting procedure in the original studies is demanding, leading many subsequent works to adopt parameter values directly from prior literature rather than performing full recalibration. This highlights a key limitation of the Holby-Morgan model: while it offers a more detailed and physically rigorous description of platinum degradation and oxidation, its practical implementation is challenging due to its numerous parameter that requires calibration. Nevertheless, its comprehensive treatment of the underlying thermodynamics and kinetics has made it popular in recent modeling efforts.

Table 2.3: Values of the fitted and assumed parameters taken from select publications using Holby-Morgan model

Literature	Operating Conditions	Voltage Conditions	v_1 [s^{-1}]	v_2 [s^{-1}]	v_1^* [s^{-1}]	v_2^* [s^{-1}]	β_1	β_2	$\bar{H}_{1,fit}$ [J mol^{-1}]	$\bar{H}_{2,fit}$ [J mol^{-1}]	U_{fit} [V]	ω [J mol^{-1}]	λ [J mol^{-1}]
Holby and Morgan, 2012 [77]	T = 80 °C	Potetiostatic [0.95 V] Triangular cycling [0.6 to 1.0 V, 20 mV/s]	$1 \cdot 10^4$	$8 \cdot 10^5$	$1 \cdot 10^4$	$2 \cdot 10^{-2}$	0.5	0.5	$6.39 \cdot 10^4$ (Potentiostatic) $4.79 \cdot 10^4$ (Cycling)	$1.2 \cdot 10^4$	1.03	$5 \cdot 10^4$	$2 \cdot 10^4$
Li et al., 2015 [78]	Varied T and RH (part of analysis)	Triangular cycling [0.6 to 1.0 V, 20 mV/s]	$1 \cdot 10^4$	$8 \cdot 10^5$	$1 \cdot 10^4$	$2 \cdot 10^{-2}$	0.5	0.5	$4 \cdot 10^4$	$1.2 \cdot 10^4$	1.03	$5 \cdot 10^4$	$2 \cdot 10^4$
Zheng et al., 2020 [80]	T = 80 °C	Varied shape and parameters (part of analysis)	$1 \cdot 10^4$	$6 \cdot 10^6$	$4 \cdot 10^4$	$4.5 \cdot 10^{-2}$	0.5	0.5	$3.7 \cdot 10^4$	$1.8 \cdot 10^4$	1.02	$1 \cdot 10^5$	$3 \cdot 10^4$
Goswami et al., 2022 [89]	Varied T and RH (part of analysis)	Triangular cycling [0.6 to 1.0 V, scan rate not explicitly mentioned]	$1 \cdot 10^4$	$6 \cdot 10^6$	$14 \cdot 10^4$	$16 \cdot 10^{-2}$	0.5	$\beta_{2,a} = 0.5$, $\beta_{2,c} = 0.35$	$4.7 \cdot 10^4$	$1.8 \cdot 10^4$	0.98	$0.8 \cdot 10^5$	$0.2 \cdot 10^4$
Huang et al., 2024 [93]	T = 80 °C P = 150 kPa RH = 100%	Square cycling, varied parameters (for analysis)	$1 \cdot 10^4$	$8 \cdot 10^4$	$1 \cdot 10^4$	$2 \cdot 10^{-2}$	0.5	0.5	$4.25 \cdot 10^4$	$1.2 \cdot 10^4$	1.03	$5 \cdot 10^4$	$2 \cdot 10^4$
Hu et al., 2025 [94]	T = 80 °C P = 1 atm RH = 50%	Square cycling [0.6 to 0.95 V, 6 s period]	$1 \cdot 10^4$	$6 \cdot 10^6$	$4 \cdot 10^4$	$4.5 \cdot 10^{-2}$	0.5	0.5	$4.5 \cdot 10^4$	$1.8 \cdot 10^4$	0.98	$1 \cdot 10^5$	$3 \cdot 10^4$

2.4.4 Rinaldo-Stumper-Eikerling Model

2.4.4.1 Foundational Studies

Starting in 2010, Rinaldo et al. [61], [95] presented literature reviews on experimental work examining dissolution dynamics of platinum nanoparticles and concluded from potentiostatic studies that Pt ion concentration and platinum dissolution exhibit weak dependence on potential at high voltages (~1.0 V for carbon-supported platinum). This suggests that electrochemical dissolution of metallic platinum is not the dominant mechanism at these potentials. Furthermore, they highlighted the lack of consensus on the relative contributions of chemical dissolution of oxide-covered platinum and electrochemical dissolution of bare platinum. This challenges the assumptions made in earlier models (e.g., Bi et al. [58] and Holby et al. [59]) that chemical oxide dissolution plays an insignificant role. To address this, the authors proposed additional chemical dissolution pathways for platinum oxide and derived an analytical solution for potentiostatic dissolution. Their derivation assumes full oxide coverage above a critical potential of 0.9 V, spatially invariant reaction rates, and dominance of Pt-O species (excluding Pt-O_2). Using only two types of fitting parameters: the dissolution rate constant and the effective surface tension, both of which can be correlated to experimental data, the analytical solution matched experimental surface-area loss trends under potentiostatic holds with close agreement. Table 2.4 shows the different values for the two parameters obtained in different conditions using their model [95].

In a subsequent work, the authors expanded their model to include redeposition[96]. This study applied the Lifshitz-Slyozov-Wagner theory of Ostwald ripening. By varying the ratio of redeposition to dissolution, they identify three behaviours. In the dissolution-limited case, there is a higher loss of surface area and particle number density but the PSD retains its original shape. In the redeposition-limited case, the PSD flattens more significantly, and the mean particle size increases substantially. In the intermediate case, however, the surface area loss exhibits a nonmonotonic S-shape surface area loss.

They further applied their model [62] to simulate degradation under potential cycling, using triangular waveforms, and included mechanisms like coagulation and particle detachment in addition to dissolution and redeposition. Their results showed that dissolution and redeposition are active under all tested conditions. However, at high upper potential limits (e.g., 1.2 V), it becomes ambiguous whether coagulation also contributes significantly. Despite this uncertainty, the experimental trends could still be captured well by using only dissolution and redeposition in the model, suggesting that these two mechanisms might be dominant or sufficient to explain the observed surface-area loss.

Table 2.4: List of parameter values obtained by Rinaldo et al.[61], [95] from model fitting with different experimental data

Operating Conditions	Cycling Conditions	$k_{diss}^{\infty,eff}$ [mol m^{-2} s^{-1}]	γ_{Pt}^{eff} [J m^{-2}]
ex situ T = 60 °C	Potentiostatic, 0.9 V	$7.8 \cdot 10^{-12}$	0.67
ex situ T = 20 °C	Potentiostatic, 1.2 V	$3.4 \cdot 10^{-12}$	0.79
in situ T = 80 °C	Potentiostatic, 0.75 V	$2.2 \cdot 10^{-15}$	1.90
in situ T = 80 °C	Potentiostatic, 0.95 V	$8.5 \cdot 10^{-13}$	0.71
ex situ T = 25 °C	Triangular cycling [0.4-1.4, 1.0 V/s]	$3.0 \cdot 10^{-11}$	1.80

This modeling approach represents a key departure from previous models due to its derivation of an analytical solution and simplification of kinetic expressions. Rather than relying on numerous empirical parameters, the model reduces complexity to a small set of physically meaningful parameters (rate constants and surface tension) that can be independently fitted and verified. Additionally, by incorporating detachment and coagulation mechanisms into the theoretical framework, the model offers a more comprehensive description of platinum degradation compared to earlier models that focused primarily on dissolution and redeposition. These added mechanisms allow the model to account for particle loss and growth dynamics more realistically, particularly under high voltage conditions where such mechanisms become more pronounced.

Note that the original model is built on key simplifications that distinguish it from the previous two frameworks, most notably the assumptions of spatial invariance. While these assumptions are useful for isolating dominant degradation mechanisms, they limit the model's ability to capture spatial gradients in the CCL. However, several studies [70], [97] have shown that these limitations can be bypassed by coupling the degradation rates calculated to the local environments, which localizes the degradation behavior and enables spatially resolved predictions of particle size evolution and ECSA.

2.4.4.2 Model Overview

The first work by Rinaldo et al. [61] presents a complete derivation of the analytical solution, which is omitted here for brevity. The simplified PSD evolution kinetic model is instead shown. It integrates the kinetics of platinum dissolution and oxidation into a single rate law for particle radius evolution. This approach bypasses the need to explicitly track each elementary reaction by combining their net effect into an effective dissolution constant. The resulting radius evolution is given as:

$$\frac{dr}{dt} = \Omega_{Pt} K_{rdp} c_{Pt^{2+}}(t) exp\left(-\frac{\Omega_{Pt}\beta\sigma_{Pt}}{RT}\frac{1}{r}\right) - \Omega_{Pt} K_{dis} c_{Pt^{2+},ref} exp\left(\frac{\Omega_{Pt}\beta\sigma_{Pt}}{RT}\frac{1}{r}\right) \quad (20)$$

The equation is often expressed in terms of R_0, which is defined as $R_0 = \frac{\Omega_{Pt}\beta\sigma_{Pt}}{RT}$

The model is simplified enough to only have three, physically intuitive fitting parameters: R_0, which is related to surface tension and controls the strength of size dependence, and K_{rdp} and K_{dis} (often combined with $c_{Pt^{2+},ref}$ to be a single fitting parameter), which are the redeposition and dissolution rate constants, respectively.

Note that in later works by the same authors, additional terms were introduced to account for coagulation and particle detachment mechanisms, but these are omitted here since the focus is solely on dissolution-driven surface area loss.

2.4.4.3 Model Adoption in Subsequent Studies

Urchaga et al. [98] applied the Rinaldo-Stumper-Eikerling model to distinguish the effects of dissolution/redeposition, coagulation, and detachment at different upper potential limits (UPLs) and waveform shapes (triangular vs. square). They found that degradation is more severe with square waveforms and at higher UPLs. Their results also suggest that particle detachment contributes to degradation at 1.2 V but not at 0.9 V. At UPL of 1.2 V, the model was able to distinguish the individual effects of dissolution/redeposition and coagulation, but these effects became less discernible at lower UPLs with reduced ECSA loss.

Baroody et al. [99] applied the Rinaldo-Stumper-Eikerling model and used a statistical approach to extract the kinetic rate constants for each degradation mechanism by fitting the model to experimental data. In this work, the authors were also able to incorporate membrane precipitation into the model by modifying the platinum mass balance. Because the model uses a conservative number of free parameters, these rate constants could be uniquely determined. Figure 2-11 shows the optimized dissolution and redeposition rate constants as a function of the upper potential limit for both low and medium surface area

carbon. In general, the redeposition values show no clear trend while the dissolution rates increase with higher upper potential cycling limits (UPL) up until 1.2 V, where detachment, coagulation, and membrane precipitation become the dominant mechanisms. Additional insights into other mechanisms are also discussed, such as how particle detachment increases with greater carbon support surface area. This work sheds light on the competing roles of catalyst vs. support in determining degradation pathways.

Wang et al. [100] developed a model to optimize the power management strategy of a fuel cell/battery hybrid transit vehicle, incorporating the Rinaldo-Stumper-Eikerling model for fuel cell degradation to evaluate long-term performance. The study aimed to minimize fuel consumption while maximizing system lifetime. One key insight, for instance, was that increasing platinum loading, despite raising upfront costs, could lower overall operating costs.

More practical applications of the Rinaldo-Stumper-Eikerling model were explored by Ao et al. [101] who used an extended version of the analytical model for steady-state power output, but considered an empirical model for transient power instead of recalibrating the same model. Their work enabled lifetime predictions of vehicles under real driving conditions, going beyond standard AST-based analyses. In a separate study, Ao et al. [102] proposed a new catalyst degradation model that tracks individual Pt particles and includes both dissolution and Ostwald ripening mechanisms. They compared their model with the Rinaldo-Stumper-Eikerling model and highlighted improvements in accuracy and particle-level resolution.

More recently, Ding et al. [103] explored in greater depth the influence of particle size distribution (PSD) on degradation. They derived dimensionless Damköhler numbers for each degradation mechanism and identified critical values that govern the evolution of the PSD shape. Their study also investigated how different initial distribution types and parameters impact overall degradation behavior.

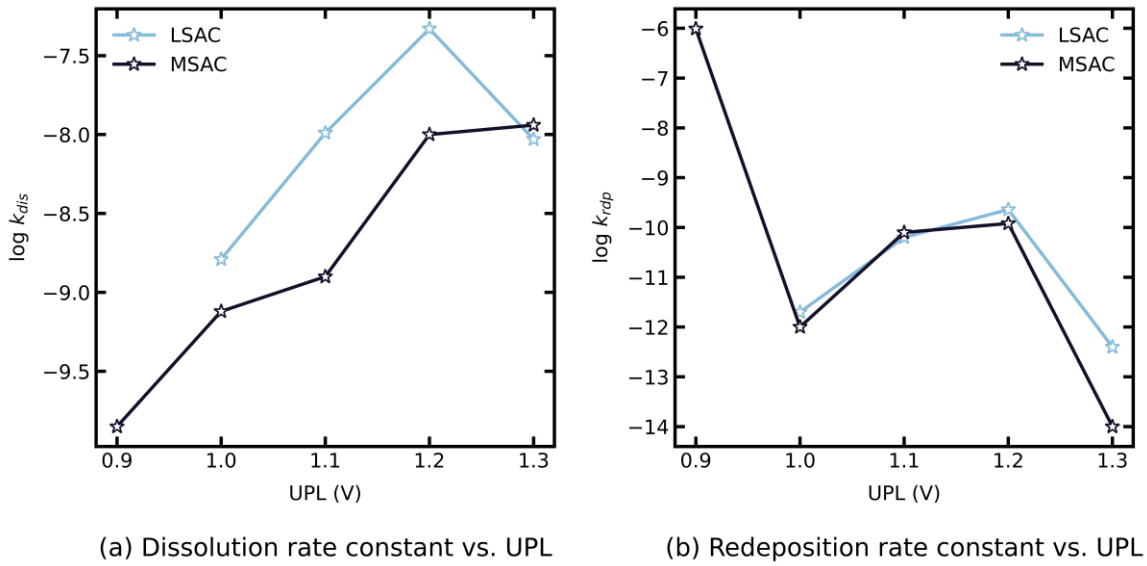


Figure 2-11: Comparisons of optimized dissolution and redeposition rate constants from Baroody et al. [99] for (a.) low surface area carbon (LSAC) and (b.) medium surface area carbon (MSAC)

2.4.5 Other Models

Other notable physics-based models have been developed over the years that diverge sufficiently from the three frameworks discussed above to be considered distinct modeling approaches but have not been as widely adopted or standardized. These physics-based models share the same goal of describing platinum degradation phenomena but introduce unique assumptions and formulations that set them apart conceptually.

Hiraoka et al. [104] presented a kinetic model similar to the Darling-Meyers model that captures platinum dissolution and oxide formation via a dissolution and redeposition approach with the Gibbs-Thomson effect, but with a different formulation and distinct rate constants for the forward and reverse reactions. Similar to earlier works, their model examines how the dissolution and re-deposition of Pt, particularly favoring smaller particles, drives changes in particle size distribution and electrochemically active surface area. The simulation results closely reflect experimental trends observed in surface area loss, particle size evolution, and distribution shifts, although the need for further development remains, and there appears to be little literature building directly on their work.

Prokop et al. [105] developed a model for platinum dissolution, oxide formation, and oxide dissolution as part of a series of studies on platinum degradation kinetics in high-temperature PEM fuel cells (HT-PEMFC) [105], [106], [107]. Adapted from kinetic models for low-temperature fuel cells (Darling-Meyers and Holby-Morgan), it was modified to reflect HT-PEMFC conditions, such as the absence of

liquid water, which uncovered unique degradation trends. It was found, for instance, that the chemical dissolution of PtO is the dominant degradation mechanism, contrary to prior findings for low-temperature systems.

Some models simplify the physics of platinum degradation to reduce computational effort and improve numerical stability, but this often comes at the cost of omitting important phenomena and finer physical details that could enhance its accuracy.

For instance, Robin et al. [108] proposed a simplified platinum degradation model considering only dissolution, which was coupled with a 2D cell performance framework. The kinetic rate equation contained common features from earlier models, such as the Gibbs-Thomson effect and potential dependence, but omitted a cathodic term, implying that the reaction is irreversible and no redeposition takes place. They reported that this initially created difficulties in achieving accurate fits to experimental data, which was addressed by introducing an equivalent active surface area. Mayur et al. [109] applied the same framework to various real-world driving cycles, to reveal distinct spatial degradation patterns and transient behaviors.

Moein-Jahromi et al. [110] developed an algorithm to forecast degradation. Their model consists of an ECSA loss model and an Ostwald ripening model. The ECSA loss model was derived from an empirical model of surface area loss, which was a previously observed correlation [43], [111], but with the correction factor separated into functions of temperature, relative humidity, and cycling conditions. The simplified Ostwald ripening model uses the Lifshitz-Slyozov-Wagner theory, and only the platinum dissolution reaction is considered. Moein-Jahromi and Kermani [112] then coupled the model to a 3D multiphase CFD model of the catalyst layer. The authors used multi-objective optimization to explore trade-offs between initial power density and power density degradation. Similar to the Rinaldo-Stumper-Eikerling model, their model is simplified and better suited for scale-bridging analyses and system-level degradation forecasts rather than detailed nanoscale mechanistic studies.

Baricci et al. [113] adopted an alternative approach, based on a model presented by Takeshita et al. [114], which used a simplified solubility equation with a size-dependent saturated concentration term and a cycle-averaged dissolution rate constant. This approach deviates from Butler-Volmer-based kinetic models that are used in most degradation studies and bears closer resemblance to empirical models of surface area loss due to its simplicity. The authors justified this simplification as a way to reduce the computational cost of simulating full dissolution and redeposition kinetics. The model was applied to evaluate gradient catalyst layer structures, showing that placing larger platinum particles and increasing the Pt/C ratio near the PEM-CCL interface is beneficial in mitigating platinum loss.

On the other hand, some models adopt a more thorough approach to capture the underlying physical phenomena with higher accuracy, though this often comes at the cost of robustness and ease of computation.

In an early study, Franco and Tembely [115] developed a modular and multiscale degradation model that links nanoscale interfacial processes to the microscale oxygen transport in the ionomer and MEA-scale transport of charged species. The nanoscale portion, illustrated in Figure 2-12, represents an electrochemical double layer composed of an inner layer (compact layer with Pt layer) and an adjacent diffuse layer. In the Pt layer, electrochemical Ostwald ripening is modeled to capture particle coarsening, while the compact layer accounts for Pt oxide, adsorbed water dipoles, and ORR intermediates. Dissolution and oxidation kinetics in this compact layer follow Darling-Meyers-type reactions, but here they are embedded in a coupled framework with the surface coverage dynamics. The diffuse layer solves the Nernst-Planck and Poisson equations for H^+ and Pt^{2+}, and Fickian diffusion for O_2.

Compared to simpler kinetic models like the Darling-Meyers model, this approach is more detailed and explicitly multiscale, and it places greater emphasis on nanoscale interfacial physics and adsorption effects. While useful for mechanistic insights and impedance spectroscopy simulations, the model is computationally complex, with a large set of strongly coupled equations to solve and many parameters to determine.

Jahnke et al. [116] developed a rigorous multiscale model for platinum degradation, expanding the platinum oxidation pathway into three steps: a fast reversible oxidation of Pt to PtOH, a slow irreversible oxidation of PtOH to PtO, and an irreversible reduction of PtO. Platinum dissolution was modeled via both direct Pt dissolution and PtO dissolution. Notably, these reactions had associated kinetic equations with PtO and PtOH coverage dependence, and similar to Holby-Morgan, variable surface tension. The model also introduced kinetic equations for platinum band formation, which is a level of detail rarely seen in other studies that incorporate platinum precipitation in the membrane. Coupled with a 2D performance model, it enabled analysis of the effects of operating conditions on platinum band location and the impact of potential cycling on ECSA loss.

The model stands out for its breadth in capturing multiple mechanisms and refining the oxidation mechanisms for greater accuracy. Similar to Franco and Tembely's work [115], a major drawback of this work is its reliance on numerous free parameters (17 fitted and assumed parameters). Thus, a thorough parametric study may still be necessary for reliability and robustness. Nevertheless, this model has potential for widespread adoption in future studies that employ physics-based modeling. In fact, this model was employed in a recent study by Van-Brunt et al. [117] to derive a scaling law for estimating the

normalized ECSA, which yielded an asymptotic equation that was analyzed for different conditions, and by Pan et al. [118] , who coupled Janke's CCL degradation model with a membrane degradation model, enabling the analysis of distinct degradation behaviours and trends within each layer.

Several studies have investigated the thermodynamics and kinetics of platinum degradation using ex-situ aqueous electrolyte tests and complementary in-cell fuel cell experiments. Notably, Ahluwalia et al. [119] obtained dissolution data for Pt/C catalysts in aqueous solution and developed a kinetic model for dissolution and oxide growth within a solid solution theory framework. Their model was applied to triangular potential cycling to study the interplay between particle size, oxide coverage and dissolution dynamics. In a subsequent study [120], the authors expanded the framework to incorporate Ostwald ripening and coalescence/sintering through a population balance approach, which enabled the prediction of particle growth and electrochemical surface area loss under both aqueous and single-cell accelerated stress tests.

A few models primarily focus on analyzing fuel cell performance and the effects of degradation on the transport processes, without fully modeling the degradation mechanisms themselves through kinetic modeling. For instance, Jomori et al. [121] studied the performance decay caused by electrochemical surface area loss and concluded that increased transport resistance in the cathode catalyst layer due to degradation significantly contributes to performance loss at high current densities. Their model did not include a kinetic description of platinum dissolution but incorporated oxidation effects to capture the voltage-dependent reduction in active surface area caused by oxide coverage, which in turn influences the oxygen reduction reaction. Similar studies include Gwak et al.'s [122] analysis of the effect of particle size on oxygen transport resistance, and Zhang et al.'s [123] of how platinum degradation alters transport paths and the distribution of platinum particles through a pore-scale analysis.

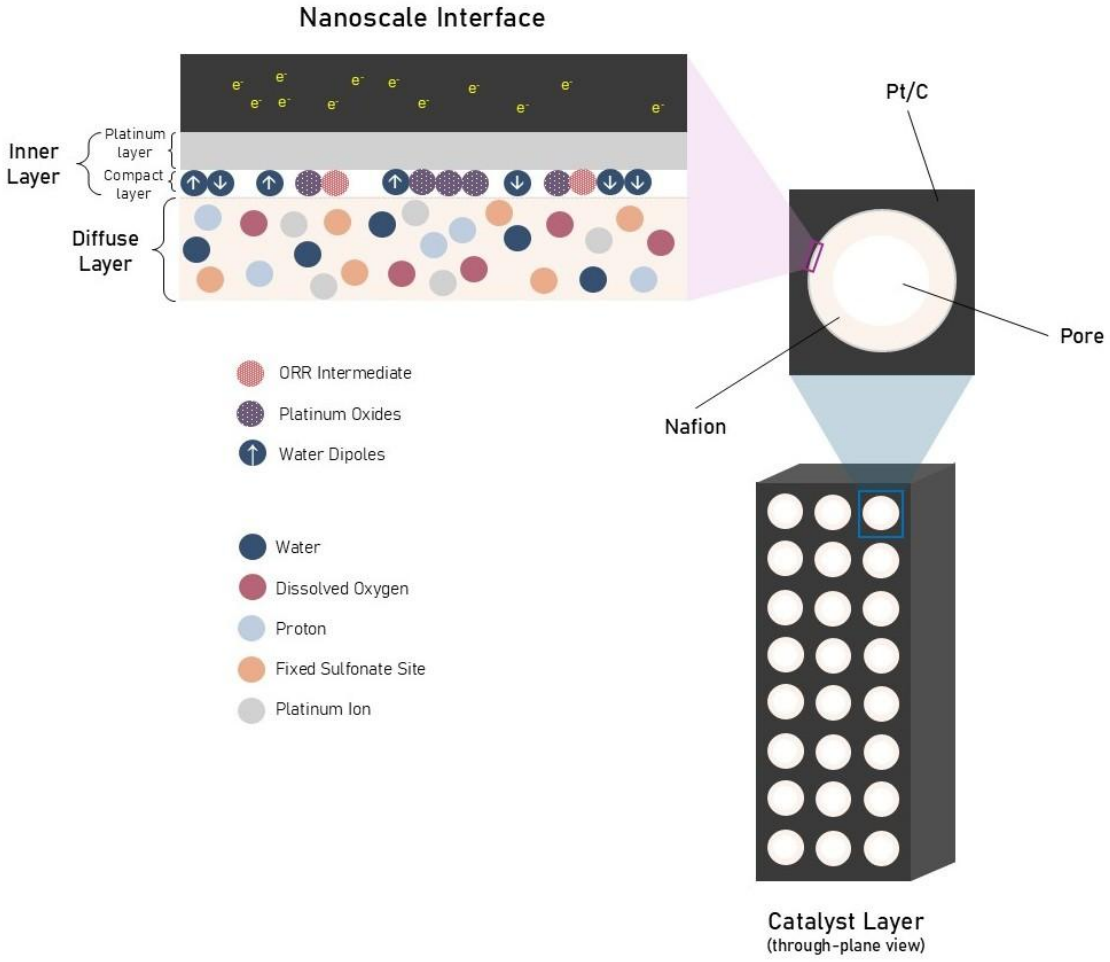


Figure 2-12: Schematic of the electrochemical double layer representation at the Pt/C-ionomer interface by Franco and Tembely [115], consisting of an inner layer (divided into platinum and compact sublayers) and a diffuse layer

2.4.6 Discussion and Outlook

2.4.6.1 Utility of the Three Modeling Frameworks

Studying the works that apply the three most common degradation modeling frameworks reveals both the different directions that modeling studies can take and which models are best suited for each application.

Physics-based models are particularly valuable because they link fuel cell operating conditions, such as temperature and potential, to the dynamics of platinum dissolution and oxidation, allowing for the prediction of surface area loss. This ability makes them powerful tools for uncovering platinum degradation behavior. Notably, the Darling-Meyers and Holby-Morgan models can relate dissolution and

oxidation rates to local conditions such as platinum ion concentration and overpotential. Thus, many studies use these frameworks to investigate degradation mechanisms in greater detail, revealing behaviors that were previously poorly understood. For example, both 1D [78], [89] as well 2D [79], [92] studies highlighted the non-uniformity of degradation, showing, for instance, that mass loss near the membrane is dominated by platinum band formation while Ostwald ripening becomes more significant further from the membrane-CCL interface. For investigations aiming to capture the spatial heterogeneity of degradation, either the Darling-Meyers or Holby-Morgan models can be employed. The Darling-Meyers model is more suitable when minimal calibration or limited experimental data are available due to its simpler formulation. In contrast, the Holby-Morgan model can provide more detailed and potentially more accurate results, but it demands extensive parameter fitting and calibration.

Some studies, on the other hand, focus on the broader influence of operating and cycling conditions, particularly when the goal is to identify ways to control external parameters to minimize degradation. For example, several works have investigated the effects of accelerated stress test (AST) protocols and voltage waveform types [50], [80], [98] offering insights into how various start-stop cycling profiles affect degradation differently. These types of studies also help determine which AST protocols best represent the lifetime power load of a vehicle under realistic conditions. In such cases, the Rinaldo-Stumper-Eikerling model or the lumped version of the Darling-Meyers model (from their first work) is often sufficient, especially when spatial detail is not the primary concern and model simplicity is desired.

Beyond physical insights, some studies emphasize the practical applications of degradation modeling, pushing it beyond theory into real-world contexts. For instance, models have been integrated into simulations of real-life drive cycles [72], [76], incorporated into larger power management strategies [91], [100], and even applied to operational devices such as field sensor fuel cells [67], transit bus [73], and industrial PEMFCs [74]. The emergence of these applications is noteworthy, as it indicates that the utility of physics-based models is expanding toward real-world applications and larger-scale use. There is also a smaller but important group of studies using models to investigate modifications of the materials used in the fuel cell as mitigation strategies, such as implementing ePTFE-reinforced membranes [81] and gradient catalyst layer structures [92]. These developments are important as they go beyond purely predictive modeling and leverages mechanistic understanding to guide in material design. For all of these applications, the model choice again depends on the desired balance between complexity and practicality. At the most detailed end, the Holby-Morgan model offers the most comprehensive description but also requires significant time for calibration and computational complexity. The Darling-Meyers model offers a simpler alternative that still retains the ability to resolve spatial variations. At the most reduced level,

the Rinaldo-Stumper-Eikerling model treats degradation in a lumped fashion, sacrificing spatial detail but providing a robust option for larger-scale or operational studies.

2.4.6.2 Trends in Model Dimensionality

The relevant papers reviewed in this study are summarized in Figure 2-13, arranged by year of publication and model dimensionality to illustrate the evolution in spatial complexity. Zero-dimensional (lumped) models treat the catalyst layer as a single homogeneous point with uniform properties. These models may include a particle size distribution (if considered) but lack spatial information. While computationally efficient, they rely on critical assumptions that can undermine relevance. Most notably, these studies use a single, uniform value for both the platinum ion concentration and the local overpotential. Spatially resolved models address these limitations by incorporating one or more spatial dimensions. Since the performance model (used to generate polarization curves by accounting for reaction kinetics) often involves species transport processes that are largely independent of the degradation model, such as oxygen or proton transport, these components can be formulated in a different way and then coupled with the degradation model. As a result, several studies employ hybrid dimensional setups (i.e., a 2D performance model coupled with a 1D degradation model)

From Figure 2-13, a trend emerges toward higher-dimensional representations of degradation, progressing from the early 0D lumped formulations to more recent 2D and 3D approaches. Despite this, most studies continue to rely on 0D or 1D formulations. The continued popularity of 0D models stems from their computational efficiency, which makes them useful when spatial non-uniformities are not central to the study. One-dimensional continuum models, on the other hand, are often sufficient to capture through-plane degradation, which is known to be the dominant source of platinum degradation heterogeneity in the catalyst layer [79] allowing modellers to neglect in-plane variations without major loss of accuracy. Two-dimensional models are typically employed when in-plane heterogeneities become significant, such as when inlet-outlet gradients exist along the flow field [94], but they remain relatively uncommon. Extensions to three dimensions are rare, as the additional computational cost is difficult to justify when through-plane variation remains the primary concern.

Finally, almost all studies identified in this review are continuum models, which treat the catalyst layer as a homogeneous medium and do not explicitly resolve the underlying pore-scale structure. So far, there have been no attempts in platinum degradation modeling at the pore scale, despite their potential to directly link morphology with platinum dissolution and oxidation behavior, likely due to their high computational complexity and the inherent multiscale nature of the catalyst layer. This gap highlights a clear opportunity for further model development as computational tools continue to improve. Approaches

such as pore network modeling [124] can offer simplified yet physically representative geometries of the catalyst layer that capture pore-scale transport and degradation behavior, potentially uncovering phenomena that are inaccessible to continuum models

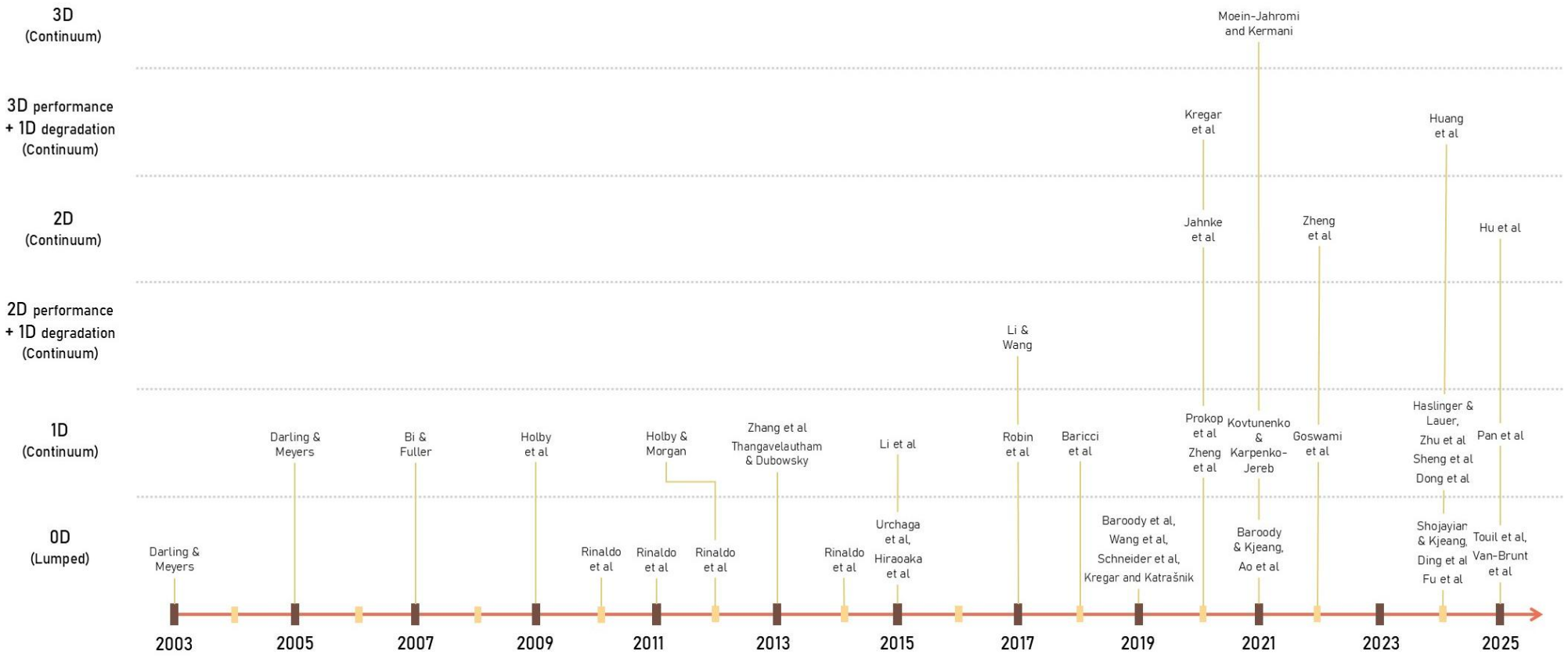


Figure 2-13: Distribution of the relevant papers reviewed, categorized by year of publication and model dimensionality. The figure highlights the gradual shift toward higher-dimensional models and greater complexity

2.4.6.3 Gaps and Future Direction

The models reviewed here have each advanced the understanding of platinum dissolution and oxidation and contributed to the broader efforts in improving fuel cell durability. Nevertheless, several important gaps remain that point to opportunities for future development.

A key limitation in many existing studies is that degradation is still often treated in isolation, without strong coupling to fuel cell performance models. For example, some implementations substitute the solid-liquid potential difference $\phi_s - \phi_l$ in Darling-Meyers with the cell voltage, V, which eliminates the need to calculate the electrolyte potential through a performance model. However, this decoupling overlooks critical interactions. The electrochemically active surface area affects the kinetics of the cathodic reaction, and platinum loss can influence proton and oxygen transport resistances. Conversely, electrode potential and local operating conditions strongly affect the rates of dissolution and oxidation. Tighter integration between performance and degradation models would therefore enable a more realistic representation of this interdependence.

Several assumptions commonly made in degradation models can also be relaxed with current computational capabilities. One example is the treatment of platinum-ion transport. While some models employ a full Nernst-Planck formulation, it is more common to assume diffusion-dominated transport and rely solely on Fick's law. Likewise, multiphase flow, such as capillary movement of liquid water and transport of dissolved gases are often excluded. Incorporating these effects in future implementations could improve understanding of how other factors influence degradation dynamics.

There also remains substantial room to expand the physical scope of degradation modeling. Recent efforts have advanced models that describe platinum precipitation in the membrane, including the fluxes of crossover hydrogen and oxygen gases and kinetic formulations for platinum nucleation and growth. Extending these developments and coupling them with dissolution and oxidation models in the catalyst layer could provide a more complete picture of platinum mass loss. Similarly, further investigation into the kinetics of PtO formation is needed, as uncertainty remains regarding oxidation pathways. Current oxidation models generally include only water-driven electrochemical oxidation, as represented in Reaction (2), but future work could explore oxygen-driven or multistep oxidation mechanisms to refine kinetic accuracy.

Many existing studies have focused on mechanistic exploration, such as end-of-life surface area prediction or the inclusion of additional dissolution and oxidation pathways, but relatively few have used models to evaluate or design mitigation strategies. Modeling provides a unique advantage over

experiments in this regard, as it enables systematic and low-cost testing of catalyst-layer structural modifications. Opportunities include investigating the influence of structural parameters, nonuniform catalyst distributions, and membranes with selective conductivity to guide material optimization. The integration of performance and degradation models, together with other degradation mechanisms such as membrane degradation and carbon corrosion, also opens the possibility of multi-objective optimization of the catalyst layer design, balancing trade-offs between performance and durability.

Another persistent issue is the lack of standardization across studies, including differences in testing protocols, parameter sets, and validation metrics. Accelerated stress tests, for example, vary widely between studies (triangular vs. square waveforms, DOE protocols vs. New European Driving Cycle) making direct comparison of results difficult, especially given that degradation behavior is highly dependent on the chosen protocol. As seen in the parameter tables (Table 2.2, Table 2.3, and Table 2.4) fitting parameters also vary across models because of differing operating and cycling conditions. Future work that systematically examines the influence of these conditions on model parameters, including feasible parameter ranges for each model, would enhance the reproducibility and practicality across the field. In this context, several common pitfalls should also be noted, particularly for new modelers entering the field. One common challenge is the difference between the model assumptions and the intended application, where simplifying assumptions made may limit the validity of the conclusions. For instance, neglecting key mechanisms or over-simplifying transport or kinetics can lead to misleading results. In addition, parameter calibration requires careful consideration, as fitted parameters directly taken from other papers are often protocol-specific and may not be transferable across studies without recalibration. Numerical implementation also presents challenges, as more complex degradation models typically involve stiff and tightly coupled equations that require appropriate discretization and choice of solvers. Being aware of these issues will ensure that the model predictions will remain physically meaningful and reproducible.

As discussed earlier, most available work remains formulated at the 0D or 1D level, with only a few studies extending to 2D or 3D representations. Moving toward applying these model frameworks at the pore scale would provide valuable insight into the relationship between structure and degradation.

In parallel with physics-based approaches, there has been a growing interest in data-driven and machine learning models for degradation prediction. While these methods can be effective for forecasting performance and ECSA loss, they generally lack the resolution required to isolate platinum degradation mechanisms or to provide physical insight into their underlying causes. Physics-based models therefore remain essential for linking degradation predictions to physical mechanisms, which is particularly

important for guiding catalyst and materials development aimed at mitigation strategies. An important opportunity for future work lies in the development of open-source, physics-based degradation software tools. Such tools could lower the barrier to entry for new researchers, improve reproducibility across studies, as well as facilitate systematic comparisons between models and experimental data. In addition, hybrid approaches that combine physics-based models with machine learning, such as physics-informed neural networks, can offer a promising direction to leverage the strengths of both methodologies.

Physics-based models could also be further integrated with experimental diagnostics and multiscale fuel cell models to improve their predictive capabilities and expand the scope of these studies beyond microscale modeling analyses. Some recent works addressing this topic are also reviewed by Prokop et al. [125]. Finally, physics-based models could be used for purposes beyond predictive degradation studies. For instance, integrating these models into system-level analyses, such as optimizing power management strategies or evaluating durability under realistic drive cycles for heavy-duty vehicles, would represent a valuable next step. Bridging detailed mechanistic modeling with device-scale applications could accelerate the translation of modeling insights into practical advances in fuel cell durability.

Overall, there is a promising outlook for degradation modeling. As computational resources continue to expand and model integration improves, future work can bridge the gap between physical understanding and practical implementation, moving fuel cells closer to widespread commercialization as a clean and durable energy technology.

2.5 Balancing Computational Accuracy and Complexity with Pore Network Modeling

As established, pore-scale modeling is a useful computational approach to both deepen the current understanding of platinum degradation behavior in the porous catalyst layer and serve as a tool to explore potential microstructural modifications to mitigate platinum catalyst degradation.

2.5.1 The Porous Cathode Catalyst Layer

Figure 2-14 shows a simplified illustration of the cathode catalyst layer showing the components that facilitate the transport of species participating in the oxygen reduction reaction. The ionomer is a continuation of the polymer electrolyte membrane and primarily serves to conduct protons while also transporting dissolved oxygen to the catalyst sites. The catalyst material is embedded within ionomer agglomerates and consists of platinum nanoparticles dispersed on a catalyst support typically composed of carbon spheres. This carbon support forms a continuously percolating electronic pathway which enables electron transport to the catalyst sites for the oxygen reduction reaction.

Surrounding the network of ionomer agglomerates is the void phase, which may consist of liquid water produced by the oxygen reduction reaction or gas species diffusing to and from the gas diffusion layer. The oxygen reactant is primarily transported through this void phase. Liquid water may also be present within the ionomer and carbon pores. The cathode catalyst layer is therefore a highly multiphase component, spanning multiple length scales and involving the transport of electrons, gases, liquids, and ions. As a result, fully resolving all relevant transport and reaction phenomena is highly challenging, which is why most modeling efforts rely on continuum approaches. However, as computational

capabilities continue to advance, there is growing interest in pore-scale modeling of the cathode catalyst layer, as such approaches can resolve phenomena that are difficult to capture using continuum models.

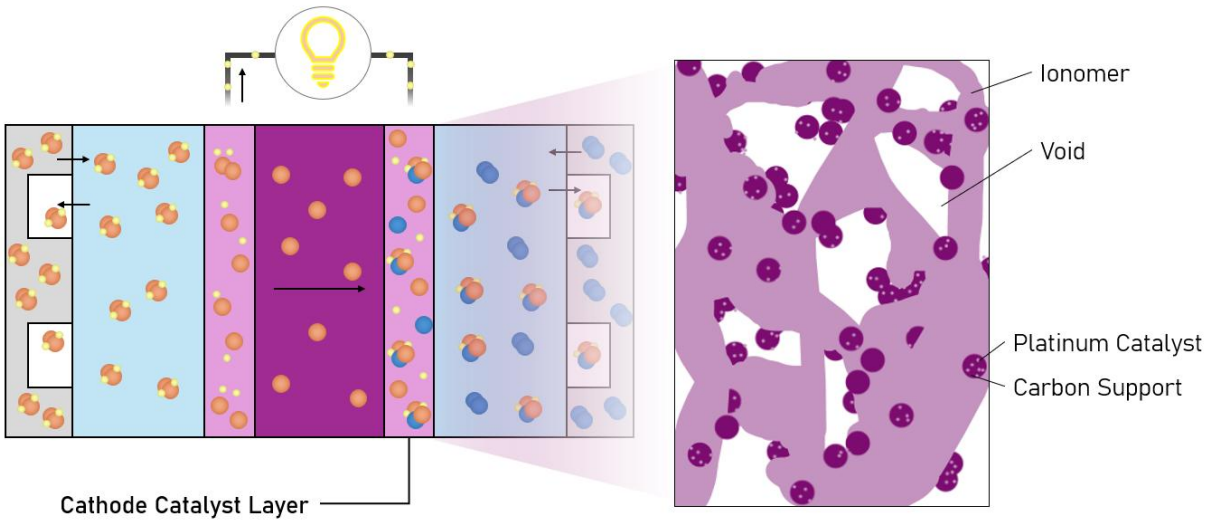


Figure 2-14: The cathode catalyst layer

2.5.2 Pore-Scale Modeling

In the field of porous media, three primary pore-scale modeling approaches are most widely used: bundle-of-tubes modeling, direct numerical modeling, and pore network modeling [126]. Bundle-of-tubes modeling is generally the most straightforward approach, in which porous media are reconstructed within a domain as a bundle of parallel capillary tubes. These capillaries may contain interacting fluids and can be modeled as simple cylindrical tubes or as more realistic pore shapes [126]. Due to its simplicity, the practical application of the bundle-of-tubes approach is limited to domains that closely resemble parallel capillary structures and does not capture complex pore geometries such as tortuous pathways or blind pores. Direct numerical modeling involves the use of reconstructed images of porous media coupled with numerical solution methods. This approach is often the most robust and rigorous, as it can be applied to highly realistic porous structures. The numerical techniques used in direct numerical modeling can be broadly classified as particle-based methods (e.g., the lattice Boltzmann method), grid-based methods (e.g., computational fluid dynamics), and morphology-based methods [126]. However, due to their complexity, direct numerical models are typically associated with high computational cost [127]. Pore network modeling represents a middle ground between the simplicity of bundle-of-tubes models and the complexity of direct numerical simulations. In this approach, porous media are represented as a simplified network of interconnected pores (nodes) and throats (edges), analogous to a resistor network. This

representation significantly reduces computational complexity relative to direct numerical simulations while retaining key geometric features and acceptable computational accuracy [127].

Pore-scale modeling remains a relatively emerging area of research for the cathode catalyst layer of PEM fuel cells, given the multiphase nature of the CCL and the critical role of species transport and electrochemical reactions in determining overall fuel cell performance. Because of the complex structure of the catalyst layer, bundle-of-tubes modeling is generally not suitable for CCL pore-scale studies. Existing modeling efforts therefore mostly employ either direct numerical simulations [128], [129], [130] or pore network modeling approaches [131], [132].

Relatively few studies have applied pore-scale models to investigate catalyst degradation in PEM fuel cells with the aim of improving understanding of how CCL pore structure influences degradation behavior. As an example, Zhang et al. [123] performed a pore-scale analysis of the CCL in a single agglomerate, reconstructing its microstructure at various degradation stages. Their study provides detailed insights into how platinum degradation alters transport paths and the distribution of platinum – effects which are not captured in conventional continuum models. However, their approach lacks transient kinetic modeling and relies instead on imaging-based reconstructions at discrete time points. Thus, while geometry is resolved at the pore scale, the model cannot dynamically predict degradation.

Several advanced pore-scale studies have examined species transport and electrochemical reactions in the CCL using approaches such as lattice Boltzmann modeling and direct numerical simulation [9–11]. However, similar to the work of Zhang et al. [123], most pore-scale models that consider degradation do so by comparing reconstructed microstructures at different degradation stages, without explicitly coupling transient platinum dissolution and oxidation kinetics with ion transport [128], [130], [133]. This limitation reduces the predictive capability of these models for platinum degradation and may overlook the influence of local pore geometry on platinum ion transport and spatial variations in platinum loss.

A pore-scale model that resolves the transient behavior of platinum degradation could therefore provide deeper insight into the specific effects of CCL pore structure on degradation mechanisms. Achieving this using direct numerical simulations is particularly challenging due to the multiscale nature of the problem: platinum ion transport occurs at the nanoscale within ionomer regions between carbon particles, while ion and dissolved gas transport occurs at the microscale through inter-agglomerate pathways. Consequently, transient platinum degradation modeling using direct numerical simulations is typically limited to small computational domains that do not fully represent the catalyst layer [134]. In this context, pore network modeling may offer advantages due to its reduced computational complexity.

2.5.3 Pore Network Modeling

As mentioned, pore network modeling is a computational approach for simulating transport phenomena in porous materials, in which the porous medium is approximated as a network of interconnected pores and throats. This representation reduces transport in a complex two- or three-dimensional geometry to a set of one-dimensional transport pathways defined along pore and throat connections. The resulting pore network formulation is mathematically analogous to a resistor network, where transport resistances may represent different physical phenomena, such as diffusion, electrical conduction, or fluid flow.

In pore network models, pores and throats can be assigned a wide range of shapes and sizes. Common idealized representations include spherical pores connected by cylindrical throats, which offer a simple and computationally efficient description, although other geometries such as cubic pores and prismatic (rectangular) throats may also be employed. More generally, network representation enables the use of concepts from graph theory in computer science, such as percolation theory, to characterize transport pathways within the porous medium.

Figure 2-15a illustrates a simple pore network consisting of three spherical pores connected in series by two cylindrical throats. Each pore is associated with a discrete state variable, denoted here as X , which may represent quantities such as concentration in a diffusion problem or electric potential in a conduction problem. Transport between adjacent pores occurs through pore-throat-pore conduits, with the associated resistance denoted by R. Figure 2-15b shows the decomposition of this conduit resistance into contributions from the two half-pores, represented by R_p and the full throat, represented by R_t. The total resistance of the conduit is given by the sum of these components.

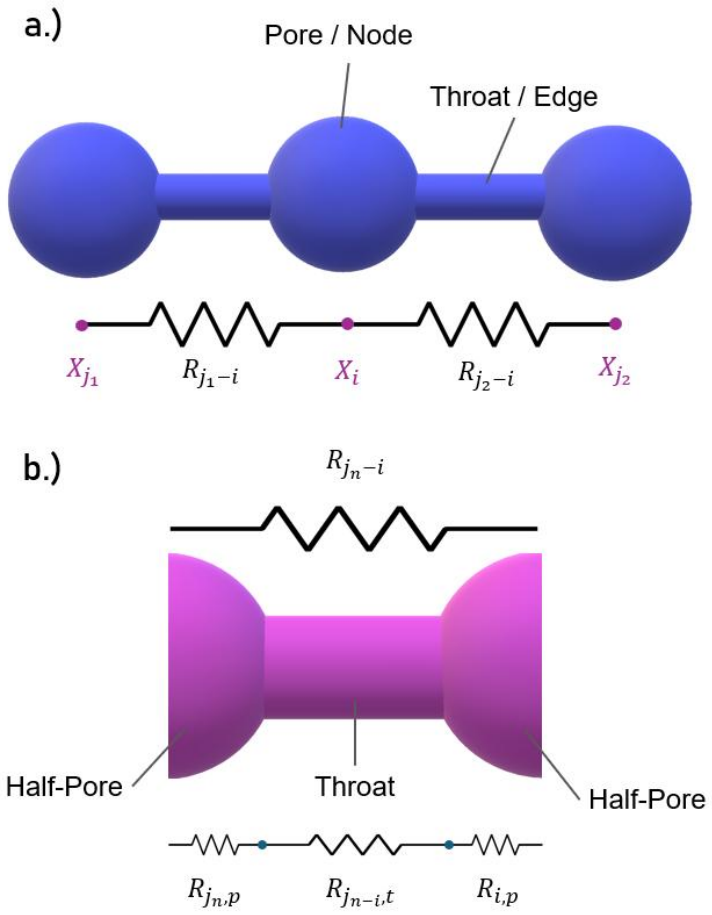


Figure 2-15: a.) Simple three-pore pore network. b.) Pore-throat-pore conduit

With appropriate boundary conditions applied at the network boundaries, the governing transport equations can be assembled into a matrix and efficiently solved using standard linear algebra techniques. This formulation allows pore network models to utilize existing numerical solvers while maintaining a physically meaningful representation of transport within the porous structure.

Pore network modeling is applicable to a wide range of transport processes, including diffusion, electrical conduction, heat transfer, and fluid flow, and can be formulated for both steady-state and transient problems. As a result, pore network models offer a favorable balance between computational efficiency and physical representativity, particularly in cases where resolving fully detailed spatial gradients is unnecessary.

Chapter 3
Simulating Transient Pore-Scale Behaviour of Platinum Degradation in PEM Fuel Cells

3.1 Overview

This study addresses the lack of pore-scale modeling frameworks for transient platinum degradation in the literature by developing a two-dimensional pore network model (PNM) of the cathode catalyst layer that couples transport with platinum dissolution and oxidation kinetics. Sadeghi et al. [132] previously demonstrated the feasibility of using PNM to predict PEMFC performance and degradation effects by reconstructing a pore network from a volumetric image of the catalyst layer and simulating cathode performance that closely matched the experimental data reported by Braaten et al. [135]. While their work included a simplified degradation analysis by selectively removing platinum sites based on experimentally measured ECSA loss distributions (e.g., higher loss near the membrane), degradation processes were not modeled explicitly. The present work extends this by introducing a fully coupled degradation model incorporating degradation kinetics and ion transport, allowing dynamic tracking of catalyst evolution and providing insight into spatial and temporal degradation trends.

To balance computational feasibility with physical representativity, it should be noted that this work employs a two-dimensional pore network to demonstrate the feasibility of simulating platinum degradation at the pore scale within a coupled performance-degradation framework. While the 2D model cannot fully reproduce 3D effects, the essential transport-reaction coupling is preserved. The predicted spatial trends in species transport, overpotential, and platinum loss are thus expected to hold qualitatively in 3D.

The present work, to the best of our knowledge, represents the first transient pore-scale model of platinum degradation in a PEM fuel cell catalyst layer. Unlike prior transient continuum models, this model explicitly resolves transport and degradation reactions within a pore network, allowing site-specific analysis of surface area loss and directly linking catalyst layer morphology with the degradation behavior.

The work presented begins by detailing the generation of the pore network geometry. The modeling strategy is then introduced, highlighting the coupling between a performance solver, which simulates the oxygen reduction reaction, and a degradation solver, which simulates the platinum degradation reactions. The model is then calibrated to available experimental data, followed by an analysis of the simulation results. These include insights into degradation trends and the effect of the porous CCL structure. It is hoped that this model will serve as a foundation for evaluating pore-scale mitigation strategies and guiding the synthesis of more durable fuel cell catalyst layers.

3.2 Geometry Generation

3.2.1 Network Generation

3.2.1.1 Pore Network Description

To investigate platinum degradation in the cathode catalyst layer, this model focuses on the transport of dissolved species within the ionomer phase, which plays a critical role in the fuel cell performance and degradation mechanisms. Thus, the developed pore network represented pores of the ionomer phase within the catalyst layer. The void phase and carbon particles were not directly modeled, but they were considered as described below.

Figure 3-1 illustrates the pore network approximation used to represent the CCL. The network represents the solid phase of the CCL, while the void phase is ignored, and rapid transport of oxygen in the gas phase is assumed. The nodes and edges of the network represent the ionomer phase, where all ion transport is confined, while the spaces between the nodes and edges of the network contain the carbon support, though these are not explicitly modeled. The network is a regular square lattice with a portion of the nodes removed to create the macro-structure arising from the presence of void space. The spatial distribution of the removed nodes is determined from an artificial binary 2D image of the catalyst layer, as detailed in the next section. This representation captures the morphology of carbon-ionomer agglomerates, where ionomer forms interconnected pathways around carbon particles. As a result, the model inherently accounts for tortuosity effects both within and between agglomerates. It should be noted that in this work, the term ‘pore’ specifically refers to the ionomer nodes of the pore network.

Within each ionomer pore, platinum particles are modeled implicitly to represent the surrounding platinum sites embedded in the ionomer and attached to nearby carbon particles. This approach avoids the computational cost of explicitly resolving individual nanoparticles while still preserving pore-scale heterogeneity in the platinum distribution.

Since species transport is affected by concentration and potential gradients along the x-direction, and boundary conditions are applied at both ends of the CCL, the full thickness of the catalyst layer is considered in the model domain. Due to computational limitations, the y-dimension is limited to match the pixel count of the x-direction, resulting in a 2D strip that is assumed sufficient to represent the CCL's geometry. Extending the model to 3D is explored in Chapter 4, while the focus of the present work is on developing the framework and validating the outputs to as large an extent as possible.

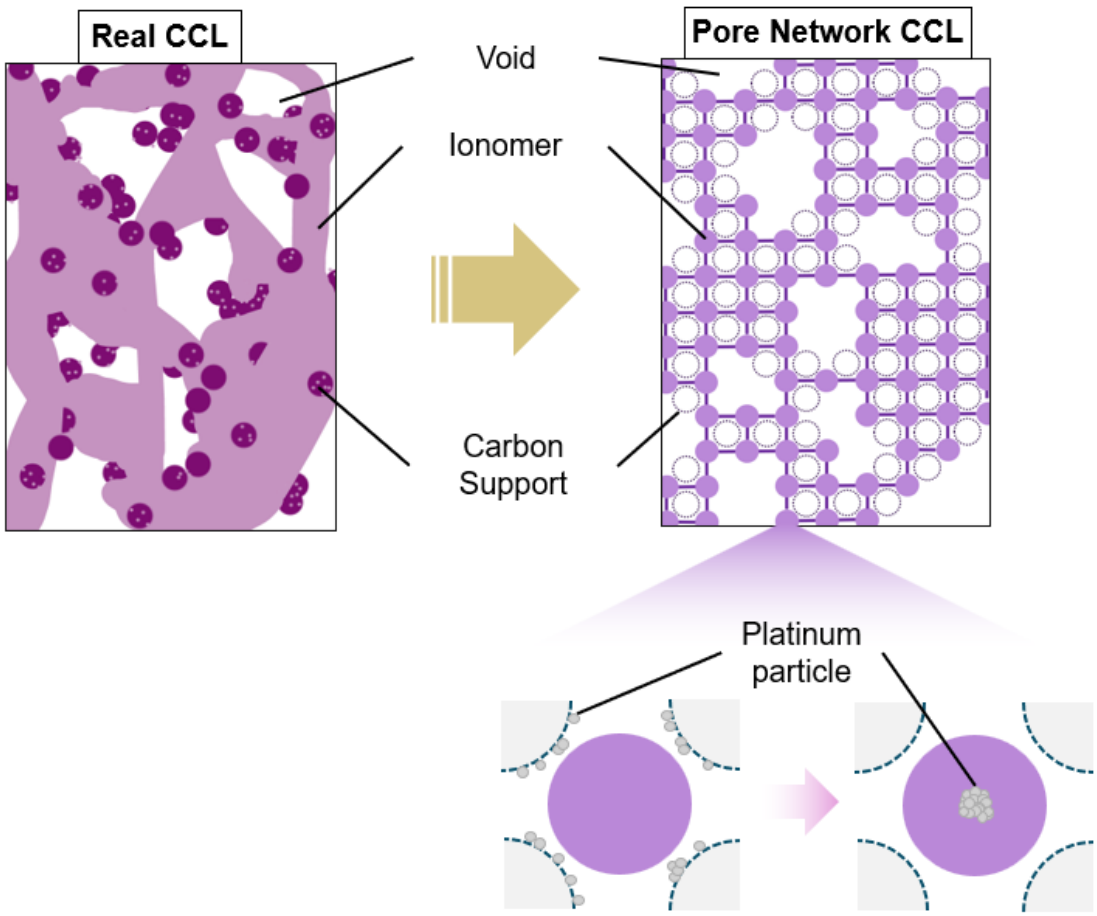


Figure 3-1: Pore network approximation of the CCL

3.2.1.2 Network Topology Construction and Network Properties

The network generation procedure in this section was carried out using PoreSpy [136], while the pore network construction and physical simulations in this work were implemented using OpenPNM [124]. Both are open-source Python libraries designed for pore-scale modeling of porous materials.

An artificial 2D image representing a strip of the catalyst layer was generated using the algorithm illustrated in Figure 3-3 Note that an image was generated, rather than using a 2D slice through experimentally obtained volumetric images such as those used by Sadeghi et al. [132], because the connectivity of the solid phase in 2D is not guaranteed in those images. The 2D images used here were generated to have similar transport properties to those of 3D images. The process begins by generating an array of random numbers between 0 and 1, where each number represents a pixel. A Gaussian blur was then applied using the variance parameter, σ. Next, a threshold was applied to remove pixels with values below the specified threshold

parameter, τ. Finally, the main solid representing a percolating path between the two ends of the image is identified, and any solids not connected to this main solid were removed.

Once the image was generated, a simple check was performed to ensure that it satisfied the geometric constraints. First, the porosity was calculated as the ratio of the number of void pixels to the total number of pixels and compared to the target porosity of the CCL. Next, the image was checked to ensure that no large pores exist from the last step of the algorithm. This was done by measuring the chord lengths of the void phase, defined as the number of continuous void pixels along the x and y-directions for each row or column. These measurements represent the straight-line distances through connected void regions and were used to detect unphysically huge pores. The chord lengths were checked if the largest chord exceeds a maximum allowable size, which was arbitrarily set to one-third of the total length of the catalyst layer. The algorithm was repeated iteratively by adjusting the values of the Gaussian blur parameter, σ, and the threshold, τ, until the porosity and maximum chord length requirements were met.

For the constructed 2D image, the size distribution of the solid agglomerate phase was determined using a local thickness filter. This distribution was then compared with that obtained from an experimentally reconstructed CCL reported by Epting and Lister [137], as shown in . The comparison reveals similar profiles and average agglomerate diameters, suggesting that the generated image is reasonably representative of an actual catalyst layer microstructure.

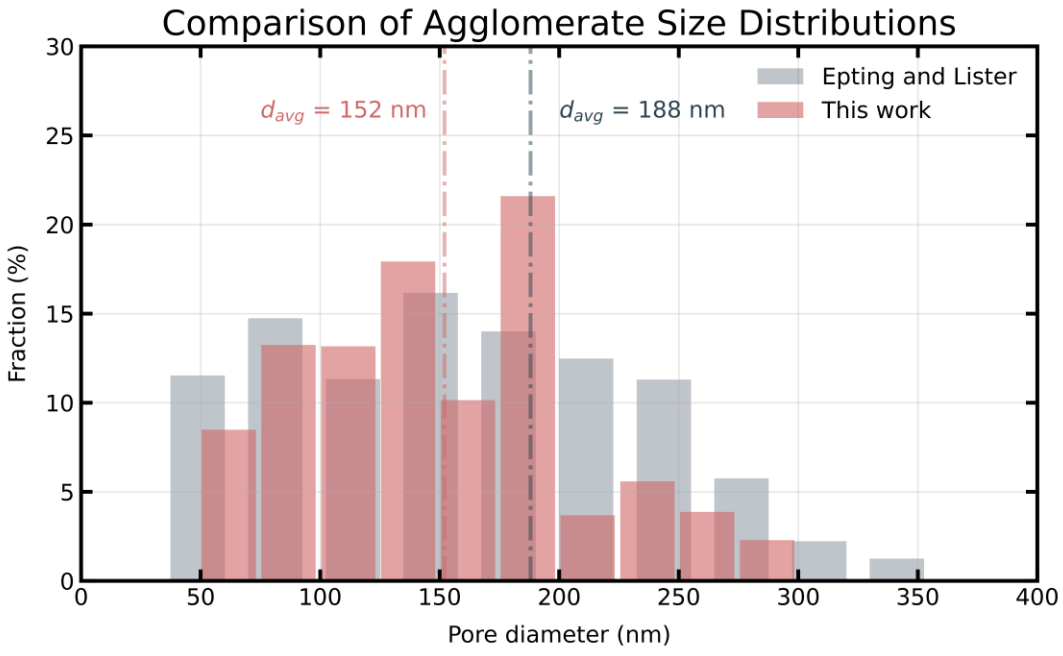


Figure 3-2: Comparison of agglomerate size distributions between the generated structure used in this work and a reconstructed catalyst layer from Epting and Lister

To relate network properties to the macroscopic characteristics of the CCL, the following set of equations was employed based on three bulk parameters: the CCL length, L_{CCL}, the carbon particle size, r_c, and the ionomer-to-carbon weight ratio, ξ.

The ionomer-to-carbon weight ratio was expressed in terms of pore network properties as:

$$\xi = \frac{\rho_{ionomer}\left(\frac{n_t}{n_p}\pi {r_t}^2 l_t + \frac{4}{3}\pi {r_p}^3\right)}{\rho_{carbon}\left(\frac{4}{3}\pi {r_c}^3\right)} \tag{21}$$

where n_t is the total number of throats, n_p is the total number of pores, $\rho_{ionomer}$ is the ionomer density, ρ_{carbon} is the carbon density, r_t is the throat radius, l_t is the throat length, and r_p is the pore radius.

The relationship between the catalyst layer thickness and the network geometry is given by:

$$L_{CCL} = n_{px}(2r_p + l_t) \tag{22}$$

where n_{px} is the number of pixels in the x-direction. The throat size was constrained within the following range:

$$0.9 * \min(r_p) > r_t > 0.1 * \min(r_p)$$

where r_p corresponds to the minimum of the pore radii that the throat is connected to. This limit will be validated in the next section. With the throat size specified, the throat length and pore size can both be determined using Equations (21) and (22).

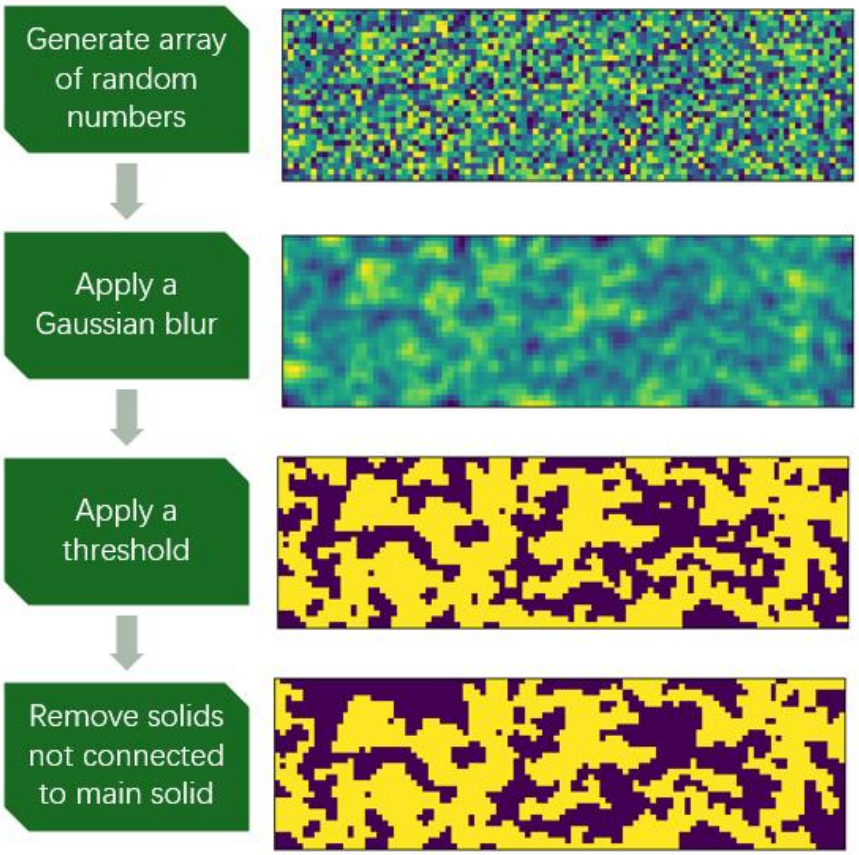


Figure 3-3: Algorithm used to generate an artificial image of the CCL

3.2.2 Network Validation

It should be noted that utilizing an artificial image can introduce morphological artifacts, such as simplified geometries that may not fully reflect those observed in experimentally reconstructed catalyst layers. Therefore, we validate our generated network by comparing its effective proton conductivity against the expected range for the CCL. First, the bulk conductivity, σ_{bulk}, is calculated from the following equation [138]:

$$\sigma_{bulk} = 100 \cdot (0.005139\lambda - 0.00326) \cdot exp\left(1268 \cdot \left[\frac{1}{303} - \frac{1}{T}\right]\right) \quad (23)$$

where T is the temperature in Kelvin and λ represents the water content, which is related to the relative humidity, RH, using [139]:

$$\lambda = 0.3 + 10.8RH - 16RH^2 + 14.1RH^3 \quad (24)$$

Next, an ohmic conduction simulation was performed on the network. A fixed voltage was applied to the leftmost pores, E_{left}, and zero voltage was applied on the rightmost pores. The resulting current, I, from the simulation was then used to compute the effective conductivity, σ_{eff}, as follows:

$$\sigma_{eff} = \frac{L_{CCL}\, I}{A_{CCL}\, E_{left}} \tag{25}$$

where A_{CCL} is the cross-sectional area of the CCL.

Olbrich et al. [140] investigated the relationship between the ionomer structure and proton conductivity, developing a model that relates ionomer morphology to conductivity. They presented their results using the dimensionless ratio, g (the ratio of effective to bulk conductivity) and the ionomer volume fraction, x_{ion}. To enable direct comparison, the same variables were adopted and defined by the following equations:

$$g = \frac{\sigma_{eff}}{\sigma_{bulk}} \tag{26}$$

$$x_{ion} = \frac{\frac{4}{3}\pi \sum_i^{n=n_p} {r_{p,i}}^3 + \pi \sum_i^{n=n_t} {r_{t,i}}^2 l_{t,i}}{A_{CCL} L_{CCL}} \tag{27}$$

A parametric study was conducted by varying the throat radius r_t, for the two limits in the imposed range: $r_t = 0.9 * \min(r_p)$, and $r_t = 0.1 * \min(r_p)$, corresponding to wide and narrow throats, respectively. For each case, the ionomer-to-carbon ratio was adjusted to explore different ionomer volume fractions and construct a g vs. x_{ion} curve.

The geometry used for validation in this study and the subsequent studies in this work follows the configuration reported by Braaten et al. [135], which was similarly used in validation by Sadeghi et al. [132]. They had a catalyst layer length of 6.4 μm. Based on this length, the number of pixels in the network was estimated to be:

$$n_{px} \approx \frac{L_{CCL}}{2r_c} = 128 \approx 130$$

Hence, a 130x130 binary image was generated. Following the approach of Sadeghi et al. [132], the target porosity of 0.45 was used, which was achieved by setting the image generation parameters to $\sigma = 1.2$ and $\tau = 0.4825$.

The resulting proton conductivity values are displayed in Figure 3-4. The results show that the wide-throat case results in higher conductivity, as a smaller throat size constricts the transfer of protons in the ionomer. The 2D nature of the pore network prevents the network from reaching the upper end of the conductivity

range. This is an expected limitation caused by percolation constraints, and their position in the lower part of the range is consistent with the expected effect of percolation in two-dimensional systems. Both cases fall within the range of proton conductivities in the CCL, demonstrating that the constructed pore network model of the CCL is sufficient to model the transport behaviors in the ionomer. Furthermore, the results indicate that the throat size and ionomer-to-carbon ratio in this model can both serve as fitting parameters to construct the network if the ionomer morphology, as described by [140], is known. For all further simulations in this work, the throat radius was chosen to be $r_t = 0.9 * \min(r_p)$ to model a case representative of mid-range conductivity values reported by Olbrich et al., while the ionomer-to-carbon ratio is chosen to be $\xi = 0.8$, as indicated in Braaten et al. [135]. This data point is also shown in Figure 3-4.

The parameters used for geometry generation, as well as the operating conditions, are shown in Table 3.1.

Table 3.1: Parameters used in geometry generation, along with the operation conditions

Symbol	Description	Value	Units	Reference
$\boldsymbol{\rho_{ionomer}}$	Ionomer density	1900	kg m^{-3}	[141]
$\boldsymbol{\rho_{carbon}}$	Carbon density	1950	kg m^{-3}	[141]
$\boldsymbol{\rho_{H_2O}}$	Water density	1000	kg m^{-3}	Assumed
$\boldsymbol{RH}$	Relative humidity	1.0	–	–
$\boldsymbol{T}$	Temperature	367.15	K	–
$\boldsymbol{P}$	Pressure	250	kPa	–

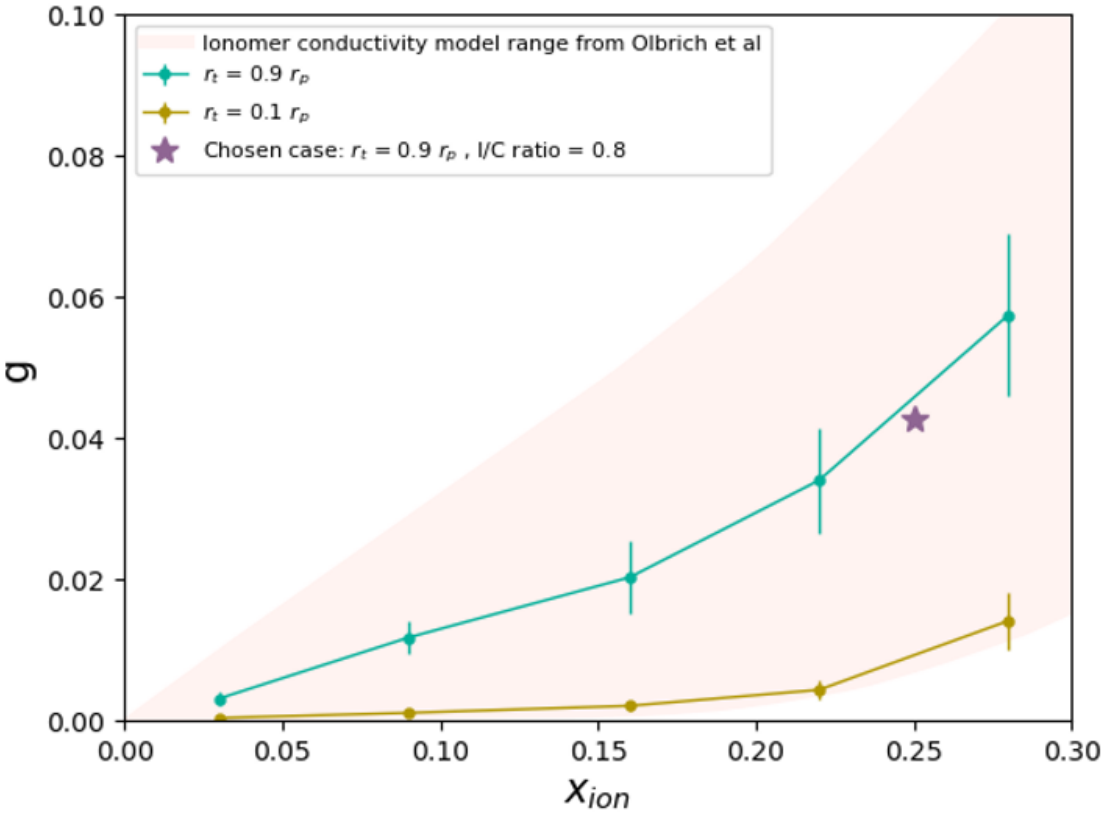


Figure 3-4: Ionomer conductivity curves for rt =0.9*min(rp) and rt =0.1*min(rp) and the chosen case compared to the conductivity range in Olbrich et al.'s model

3.2.3 Addition of Platinum Particles

As shown in Figure 3-1, each ionomer pore is assumed to implicitly contain multiple platinum nanoparticles, representing the surrounding platinum sites. To simplify the calculations, the particles in each pore are assigned uniform properties (e.g., same sizes, location, oxide coverage, etc.), while a particle size distribution is applied spatially as detailed in the next sections. The number of platinum nanoparticles in each pore, $n_{Pt,i}$, was varied and assumed to have a normal distribution and is randomly distributed spatially.

The number of particles was obtained from the platinum catalyst loading, λ_{Pt} through the following equation:

$$n_{Pt,i} = \frac{A_{CCL}\lambda_{Pt}}{n_p \rho_{Pt} V_{Pt}} \tag{28}$$

where V_{Pt} is the volume of a platinum particle, calculated assuming that the particles are spherical with radius r_{Pt}.

3.3 Model Development

3.3.1 Modelling Strategy

Figure 3-5 presents the modelling strategy used in this work. The degradation model takes a voltage vs. time profile as an input representing the vehicle's load demand over time. In degradation studies in the literature, this input comes from accelerated stress tests (ASTs) which vary across studies [142] and must therefore be specified by the user. Additional required inputs include the initial condition of the catalysts at the beginning of life (BOL) and the concentration and voltage boundary conditions.

The degradation model itself consists of two coupled solvers: a performance solver, which simulates the ORR, and a degradation solver, which models the platinum degradation reactions as a function of the local overpotential distributions coming from the previous step. In turn, the performance solver requires information on the available catalyst surface area, which is continuously updated by the degradation solver as platinum dissolves or oxidizes. This interdependence necessitates the coupling of the two solvers as shown in Figure 3-5.

Ultimately, the model outputs the temporal and spatial evolution of the platinum catalysts within each pore, allowing for the observation of pore-scale degradation behaviour throughout the catalyst layer.

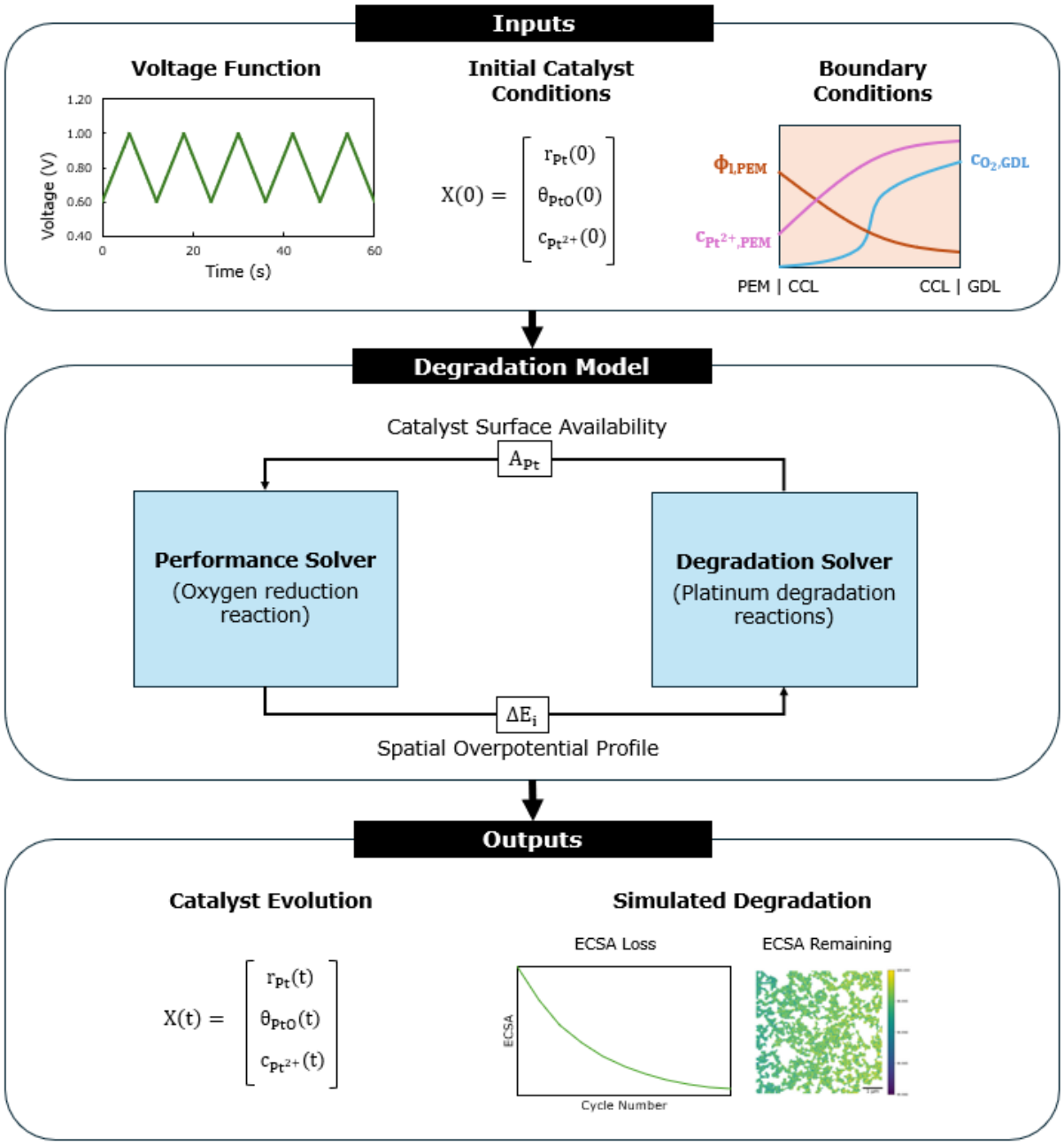


Figure 3-5: Outline of the degradation modelling strategy employed

3.3.2 Performance Solver

3.3.2.1 Solution Framework

The performance solver is designed to compute the spatial overpotential profile of the pore network by calculating the local ORR rate at each pore at an applied cell voltage.

The following assumptions were made:

- The crossover of oxygen into the PEM is neglected, and a zero-diffusion boundary condition is applied to the pores in the PEM-CCL interface.
- The void phase in the CCL has a uniform O_2 concentration, which is calculated by solving the diffusion of oxygen through the GDL at each overpotential.
- Since the conductivity of electrons in the solid phase is around three orders of magnitude higher compared to the protonic conductivity in the electrolyte phase [132], the voltage drop in the solid phase was assumed to be negligible and equal to the cell voltages.
- Formation of liquid water was assumed to be negligible, as the voltage cycling operates at lower current densities and the cell temperature is 94 °C.

The solution algorithm involves an iterative process, as shown in Figure 3-6. The process, along with the equations used for each step, is described in the next section.

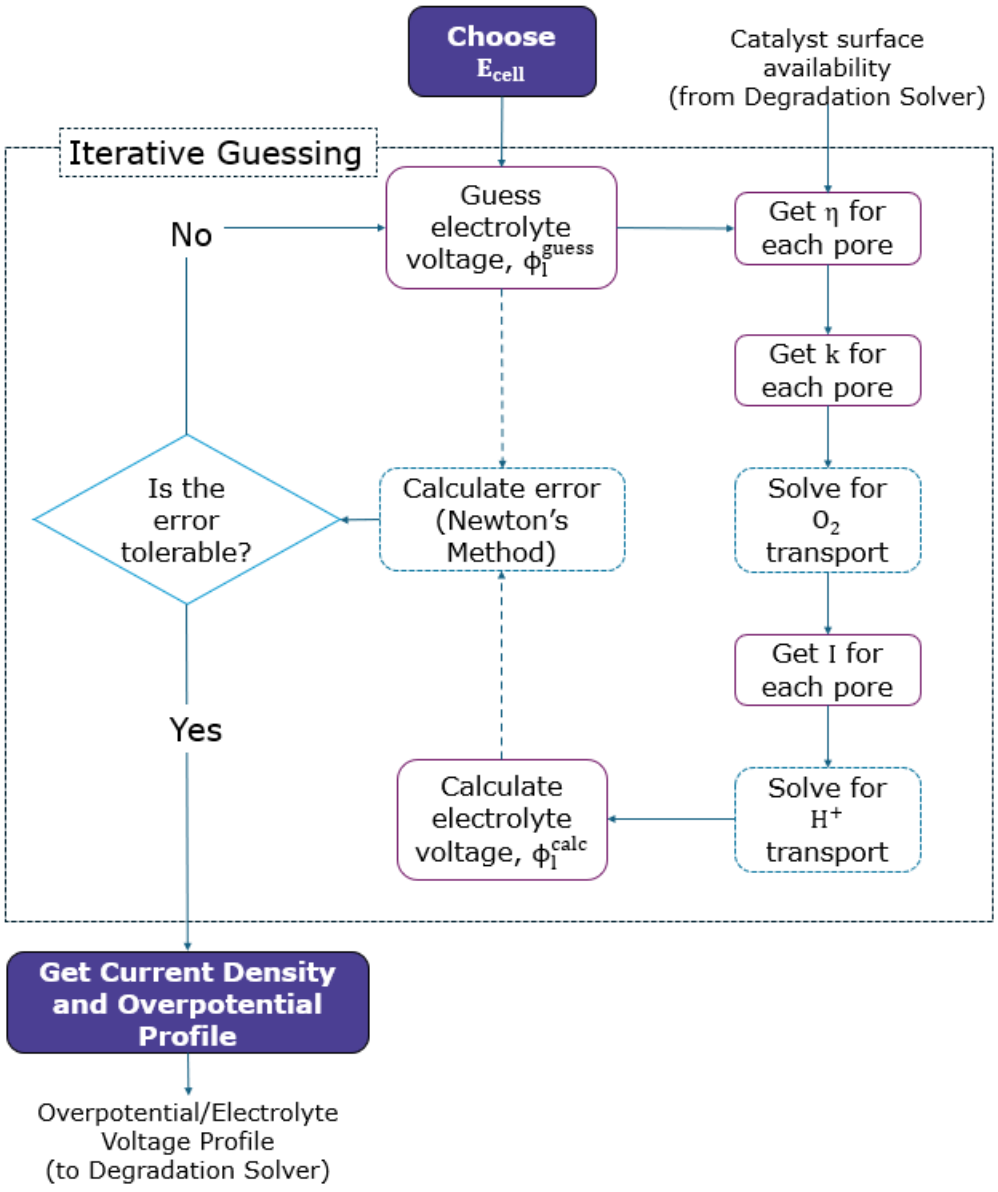


Figure 3-6: Flowchart of the algorithm used for the performance solver

3.3.2.2 Model Equations

For each cell voltage, an initial guess is first set for the electrolyte voltage, ϕ_l. The overpotential, η, for each pore i, is calculated using:

$$\eta_i = \phi_{s,i} - \phi_{l,i} - E_{eq} \tag{29}$$

where ϕ_s is the potential of the solid phase and E_{eq} is the open-circuit voltage.

The oxygen reduction reaction rate equation is assumed to follow Butler-Volmer kinetics in the following form [132]:

$$R_i = k_i c_i \tag{30}$$

where k_i is found from:

$$k_i = \frac{j_0}{c_0}\frac{A_{Pt,i}}{nF}\left[exp\left(\frac{\alpha_{a,ORR} zF}{RT}\eta_i\right) - exp\left(-\frac{\alpha_{c,ORR} zF}{RT}\eta_i\right)\right] \tag{31}$$

Here, c_i is the dissolved oxygen concentration at pore i, j_0 is the exchange current density, c_0 is the reference oxygen concentration, n is the number of electrons transferred in the overall reaction, F is the Faraday's constant, $\alpha_{a,ORR}$ and $\alpha_{c,ORR}$ are the anodic and cathodic transfer coefficients, respectively, z is the number of electrons transferred in the rate-determining step, R is the universal gas constant, and T is the temperature.

The catalytically active surface area of the platinum sites of the catalysts at pore i, $A_{Pt,i}$ is defined as:

$$A_{Pt,i} = n_{Pt,i}\left[4\pi {r_{Pt,i}}^2\left(1 - \theta_{vac,i}\right)\right] \tag{32}$$

where n_{Pt} is the number of platinum sites, r_{Pt} is the platinum radius

θ_{vac} is the fraction of vacant sites in the platinum surface, defined in this work as:

$$\theta_{vac} = \begin{cases} 1 - \theta_{PtO}, & \theta_{PtO} < 1 \\ 0, & \theta_{PtO} \geq 1 \end{cases} \tag{33}$$

θ_{PtO} is the platinum oxide coverage. The radius and oxide coverage are obtained from the degradation solver.

Using the calculated k_i, the oxygen transport in the CCL's ionomer phase can be solved using the pore network reaction-diffusion equation:

$$\sum_j G_{ij}\left(c_j - c_i\right) = k_i c_i \tag{34}$$

where the summation is done on the neighboring pores of pore i, c_j is the concentration of the neighbouring pores, and G_{ij} is the diffusive conductance of the pore-throat-pore conduit between pores i and j. This is given by:

$$G_{ij} = \left(\frac{1}{g_{pore\ i}} + \frac{1}{g_{throat\ i,j}} + \frac{1}{g_{pore\ j}}\right)^{-1} \tag{35}$$

where $g_{pore\ i}$ and $g_{pore\ j}$ is the conductance in the half-pore of pores i and j, respectively:

$$g_{pore\ i} = \frac{D_{O_2,ion} A_{p,i}}{r_{p,i}} \tag{36}$$

and $g_{throat\ i,j}$ is the throat conductance:

$$g_{throat\ i,j} = \frac{D_{O_2,ion} A_{t,ij}}{l_{t,ij}} \tag{37}$$

In these equations, $D_{O_2,ion}$ is the oxygen diffusivity in the ionomer, $A_{p,i}$ is the cross-sectional area of the half-pore, $A_{t,ij}$ is the cross-sectional area of the throat, $r_{p,i}$ is the pore radius, and $l_{t,ij}$ is the throat length.

Outer pores are the ionomer pores that are exposed to the void phase. In addition to transport between the ionomer pores, the model solves for oxygen transport in the GDL as well as the transport of oxygen from the void phase (as a gas) into the centre of the outer pores (as dissolved oxygen). For these pores, the following diffusive conductance term will need to be added in the conductance-in-series calculation:

$$G_{i,GDL}\left(c_{outside} - H_{O_2,ion} c_i\right) \tag{38}$$

where $c_{outside}$ is the concentration of oxygen entering the GDL (set as a boundary condition), $H_{O_2,ion}$ is the dimensionless Henry's constant that relates the concentrations of oxygen gas and dissolved oxygen at equilibrium in the void-ionomer interface:

$$H_{O_2,ion} = \frac{c^*_{air}}{c^*_{ionomer}} \tag{39}$$

To determine the value of the Henry's constant, a correlation for operating temperatures of 45 to 100 °C was used [143], which expresses the solubility of oxygen in ionomer as a function of temperature. This expression is modified to be expressed as the dimensionless Henry's constant in the following expression:

$$H_{O_2,ion} = \frac{2.087 \cdot 10^5}{RT} exp\left(-\frac{500}{T}\right) \tag{40}$$

$G_{i,GDL}$ is the combined diffusive conductance in the GDL and the half-pore:

$$G_{i,GDL} = \left(\frac{1}{g_{GDL}} + \frac{H_{O_2,ion}}{g_{pore,i}}\right)^{-1} \tag{41}$$

and g_{GDL} is the GDL diffusive conductance, defined as:

$$g_{GDL} = D_{O_2,air} \frac{\varepsilon_{GDL}}{\tau_{GDL}} \frac{A_{CCL}}{L_{GDL}} \tag{42}$$

where $D_{O_2,air}$ is the diffusivity of oxygen in air, ε_{GDL} is the GDL porosity, τ_{GDL} is the GDL tortuosity, A_{CCL} is the cross-sectional area of the CCL, and L_{CCL} is the length of the GDL.

The boundary condition is calculated using the ideal gas law and accounting for the water content in air:

$$c_{outside} = 0.209 \left[1 - RH \frac{P_{v,H_2O}}{P}\right] \frac{P}{RT} \tag{43}$$

P_{v,H_2O} is the vapour pressure of water, and is determined using the Antoine equation [144]:

$$\log\left(P_{v,H_2O}\right) = 5.40221 - \frac{1838.675}{T - 31.737} \tag{44}$$

The resulting system of equations is then solved to determine the dissolved oxygen concentration in each pore.

Once the oxygen concentration is obtained, the resulting current is computed for each pore:

$$I_i = k_i c_i n F \tag{45}$$

This current is used to obtain the resulting electrolyte potential in each pore by performing a charge balance around each node:

$$\sum_j Q_{ij}\left(\phi_j - \phi_i\right) = -I_i \tag{46}$$

Similar to the diffusion equation, the summation is done on the neighboring pores of pore i, ϕ_j is the electrolyte voltage of the neighboring pores, and Q_{ij} is the protonic conductance of the pore-throat-pore conduit, described by the following equation:

$$Q_{ij} = \left(\frac{1}{q_{pore\,i}} + \frac{1}{q_{throat\,i,j}} + \frac{1}{q_{pore\,j}}\right)^{-1} \tag{47}$$

where $q_{pore\,i}$ and $q_{pore\,j}$ is the conductance in the half-pore of pores i and j, respectively:

$$q_{pore} = \frac{\sigma_{bulk} A_{p,i}}{r_i} \tag{48}$$

where σ_{bulk} is described in Equation (23) and $q_{throat\,i,j}$ is the throat conductance:

$$q_{throat} = \frac{\sigma_{bulk} A_{t,ij}}{l_{ij}} \tag{49}$$

For pores on the left boundary, the following term is added to Eq. (47) to account for the transport of protons in the membrane:

$$Q_{i,PEM}(\phi_{PEM} - \phi_i) \tag{50}$$

where ϕ_{PEM} is the ionomer voltage on the left boundary of the membrane (set to 0 V as a boundary condition), and $Q_{i,PEM}$ is the protonic conductance of the membrane:

$$Q_{i,PEM} = \frac{\sigma_{bulk} A_{CCL}}{L_{PEM}} \tag{51}$$

where L_{PEM} is the membrane thickness.

Similar to solving for oxygen concentrations, the resulting system of equations is solved using a matrix solver to determine the electrolyte voltage at each pore.

The error between the calculated electrolyte voltage, ϕ_l^{calc}, and the guessed electrolyte voltage, ϕ_l^{guess} computed as:

$$\varepsilon\left(\phi_l^{guess}\right) = \phi_l^{guess} - \phi_l^{calc} \tag{52}$$

The tolerance for the error was set to $1 \cdot 10^{-5} V$ so that the loop will continue until the following condition is met:

$$\left| max\left(\varepsilon\left(\phi_l^{guess}\right)\right) \right| < 1 \cdot 10^{-5} V$$

Otherwise, Newton's method was used to determine the values of the next guess. This involves doing a second set of iterations with the guessed electrolyte voltage incremented by a small value, Δ, as follows

$$\phi_{l+\Delta}^{guess} = \phi_{l+\Delta}^{guess} + \Delta \tag{53}$$

Repeating the above process with the new guessed value will result in a new set of calculated electrolyte voltages, $\phi_{l+\Delta}^{calc}$. The error, $\varepsilon\left(\phi_{l+\Delta}^{guess}\right)$, was similarly calculated. The derivative of the error is estimated using the following equation:

$$\varepsilon'^{\left(\phi_{l+\Delta}^{guess}\right)} = \frac{\varepsilon\left(\phi_{l+\Delta}^{guess}\right) - \varepsilon\left(\phi_l^{guess}\right)}{\Delta} \tag{54}$$

The next guess is then calculated using the following equation:

$$\phi_l^{guess,next} = \phi_l^{guess} \frac{\varepsilon\left(\phi_l^{guess}\right)}{\varepsilon'\left(\phi_l^{guess}\right)} \tag{55}$$

The process repeats for the new ϕ_l^{guess}. Once the condition is satisfied, the algorithm exits the loop, and the current density at the specified cell voltage is recorded, along with the corresponding overpotential profile.

3.3.3 Degradation Solver

3.3.3.1 Solution Framework

Three degradation reactions were included in this model, based on the framework proposed by Darling and Meyers [51]. These are:

1. Electrochemical dissolution of platinum:

$$\mathrm{Pt} \rightleftharpoons \mathrm{Pt^{2+}} + 2\mathrm{e^-} \tag{56}$$

2. Electrochemical oxidation of platinum:

$$\mathrm{Pt} + \mathrm{H_2O} \rightleftharpoons \mathrm{PtO} + 2\mathrm{H^+} + 2\mathrm{e^-} \tag{57}$$

3. Chemical dissolution of platinum oxide:

$$\mathrm{PtO} + 2\mathrm{H^+} \rightleftharpoons \mathrm{Pt^{2+}} + \mathrm{H_2O} \tag{58}$$

Additionally, the degradation model accounts for the effects of platinum loss into the membrane, where a platinum band is known to form over time and significantly contributes to degradation [145].

The solution algorithm involves solving for three key variables which are properties of the platinum sites in each pore in the network: the platinum radius, r_{Pt}, which represents the size of the platinum sites within the pore, the platinum oxide coverage, θ_{PtO}, defined as the fraction of the platinum site surface that has oxidized, and the platinum ion concentration, $c_{Pt^{2+}}$, which captures the net effect of platinum dissolution and redeposition occurring within the pore as well as the influence of ion diffusion throughout the ionomer phase. An illustration of the model framework of the degradation model is shown in Figure 3-7.

Some additional assumptions for the degradation solver are:

- The transport of platinum ions is primarily driven by diffusion, and the contribution of migration is negligible. This assumption was similarly made by Bi and Fuller [58] due to the weak potential field at low current densities, which is the case for the operating voltage of the AST (1.0 to 0.6 V), as seen in Figure 3-8a.
- Surface area loss due to the effects of carbon corrosion (e.g., particle detachment and coalescence) when the interaction between the catalyst and support weakens over time, is not included in the model, and is assumed to have negligible effects on degradation at the current conditions. This follows Meyers and Darling [42], who reported that carbon corrosion becomes significant only over longer timescales and at higher potentials. Moreover, its effects can be mitigated by modifying operating strategies, such as maintaining uniform fuel distribution and performing nitrogen purging.
- Platinum loss by dissolution into the water phase and subsequent transport to the GDL is neglected.
- The platinum band is assumed to be very thin, have a constant location, and completely consume platinum ions as a mass sink, where platinum ions are assumed to be permanently lost as they precipitate to the membrane band.

It should be noted that the added complexity of simulating the nanoscale diffusion of Pt ion species introduces numerical stiffness, which requires the timestep to be below 1 μs for the system to be stable. As a result, the degradation solver is computationally expensive, and only a limited number of cycles can be simulated within a reasonable time frame. However, this limitation is offset by the model's ability to resolve pore-scale degradation behaviour. By explicitly representing the microstructure, the model captures the influence of local geometry on degradation dynamics. Furthermore, the temporal resolution enables the observation of transient degradation processes that are otherwise difficult to access in coarser or steady-state models. The numerical solver used in this work is an explicit fourth-order Runge-Kutta scheme (RK4). Improvements to the numerical methods used might provide some relief, but this is left for future work. This could include implementing implicit time-integration schemes to better handle the stiffness of the problem, and leveraging iterative solvers that can take advantage of parallel and GPU-based computing.

The model equations follow the formulation proposed by Darling and Meyers [51], where each rate is expressed as a function of these three variables and the local potential difference between the solid and electrolyte phases, ΔE. The evolution of each of the three variables with time is also dependent on the rate equations, resulting in a system of coupled, nonlinear, time-dependent differential equations. These equations are solved numerically using an iterative solver scheme, and the governing equations are detailed in the following section.

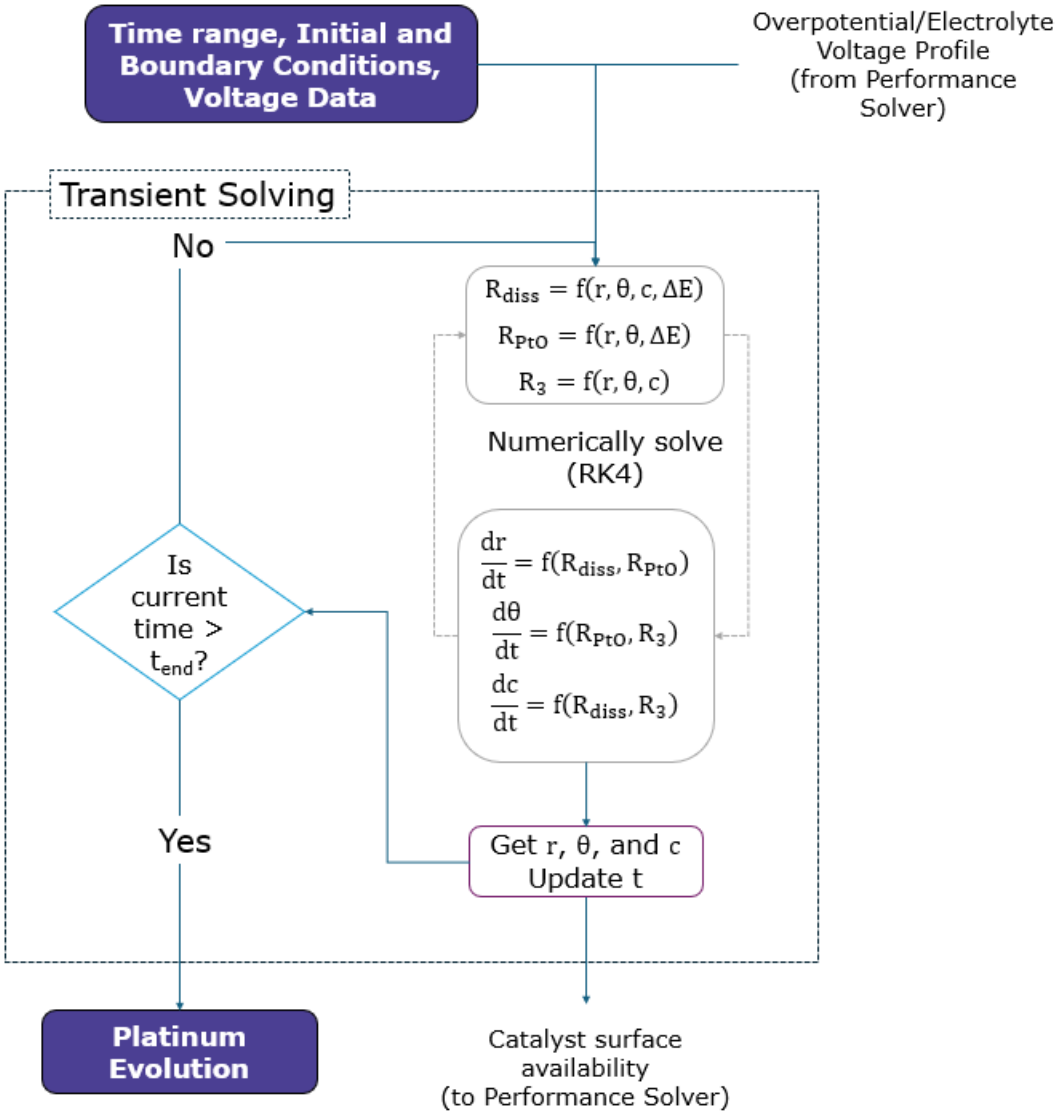


Figure 3-7: Flowchart of the algorithm used for the degradation solver

3.3.3.2 Model Equations

The rate of platinum dissolution, R_{diss}, involves a Butler-Volmer rate equation, described by the following equation:

$$R_{diss} = k_{diss}\theta_{vac}\left[exp\left(\frac{\alpha_{diss,a}n_{diss}F}{RT}\left(\Delta E - U_{diss}(r)\right)\right) - \left(\frac{c_{Pt^{2+}}}{c_{Pt^{2+}}^{ref}}\right)exp\left(-\frac{\alpha_{diss,c}n_{diss}F}{RT}\left(\Delta E - U_{diss}(r)\right)\right)\right] \quad (59)$$

where k_{diss} is the rate constant, $\alpha_{diss,a}$ is and $\alpha_{diss,c}$ are the anodic and cathodic transfer coefficient, respectively, n_{diss} is the number of electrons transferred in the reaction, $c_{Pt^{2+}}^{ref}$ is the reference concentration of platinum ions, ΔE is the difference between the solid and electrolyte voltage,

$$\Delta E = \phi_s - \phi_l \tag{60}$$

and $U_{diss}(r)$ is the size-dependent reversible potential for dissolution, defined as:

$$U_{diss}\,(r) = U_{diss}^{\theta} - \frac{\sigma_{Pt} M_{Pt}}{2\rho_{Pt} F}\frac{1}{r_{Pt}} \tag{61}$$

where U_{diss}^{θ} is the standard thermodynamic potential for the dissolution reaction, σ_{Pt} is the surface tension of platinum, M_{Pt} is the molar mass of platinum, and ρ_{Pt} is the platinum density.

The rate of platinum oxide formation, R_{PtO}, is similarly defined using a Butler-Volmer rate law:

$$\begin{aligned} R_{PtO} = k_{PtO}\Bigg[& exp\left(-\frac{\omega_{PtO}\theta_{PtO}}{RT}\right) exp\left(\frac{\alpha_{PtO,\,a} n_{PtO} F}{RT}\left(\Delta E - U_{PtO}(r)\right)\right) \\ & - \theta_{PtO}\left(\frac{c_{H^+}}{c_{H^+}^{ref}}\right)^2 exp\left(-\frac{\alpha_{PtO,\,c} n_{PtO} F}{RT}\left(\Delta E - U_{PtO}(r)\right)\right)\Bigg] \end{aligned} \tag{62}$$

where k_{PtO} is the rate constant, ω_{PtO} is the PtO interaction coefficients, $\alpha_{PtO,\,a}$ and $\alpha_{PtO,\,c}$ are the anodic and cathodic transfer coefficients, respectively, n_{PtO} is the number of electrons transferred in the reaction, $c_{H^+}^{ref}$ is the reference proton concentration, c_{H^+} is the proton concentration defined as:

$$c_{H^+} = \frac{1}{\left(\frac{EW}{\rho_{ion}} + \frac{\lambda M_{H_2O}}{\rho_{H_2O}}\right)} \tag{63}$$

where EW is the equivalent weight of the ionomer, M_{H_2O} is the molar mass of water, and ρ_{H_2O} is the density of water. The same ionomer water content, λ, as defined in the Network Validation section, is used.

$U_{PtO}(r)$ is the size-dependent reversible potential for oxidation, defined as:

$$U_{PtO}\,(r) = {U_{PtO}}^{\theta} + \left(\frac{\Delta\mu_{PtO}^0}{2F} + \frac{\sigma_{PtO} M_{PtO}}{2\rho_{PtO} F} - \frac{\sigma_{Pt} M_{Pt}}{2\rho_{Pt} F}\right)\frac{1}{r_{Pt}} \tag{64}$$

where ${U_{PtO}}^{\theta}$ is the standard thermodynamic potential for the oxidation reaction, $\Delta\mu_{PtO}^0$ is the chemical potential shift, σ_{PtO} is the surface tension of platinum oxide, M_{PtO} is the molar mass of platinum, and ρ_{PtO} is the platinum oxide density.

Both potential terms for the dissolution reaction in Eq. (61) and the oxide formation reaction in Eq. (64) are size-dependent due to the Gibbs-Thomson effect. As a result, smaller particles, with higher surface energies, are more prone to dissolution and oxidation, and the model naturally captures electrochemical Ostwald ripening effects.

The rate of the chemical dissolution of platinum oxide is described by the following rate law equation:

$$R_3 = k_3 \left[\theta_{PtO} c_{H^+}^2 - \frac{c_{Pt^{2+}}}{K_3} \right] \tag{65}$$

where k_3 is the rate constant, and K_3 is the equilibrium constant, defined as:

$$K_3 = exp\left[\frac{F}{RT} \left(n_{diss} U_{diss}\,(r) - n_{PtO} U_{PtO}\,(r) \right) \right] \tag{66}$$

The evolution of the three variables in each pore is defined by a set of differential equations. The platinum radius evolution is a function of the platinum dissolution rate, described in the following equation:

$$\frac{dr_{Pt}}{dt} = -\frac{M_{Pt}}{\rho_{Pt}} R_{diss} \tag{67}$$

The change in the platinum oxide coverage with time is a function of both the platinum oxide formation and dissolution rates:

$$\frac{d\theta_{PtO}}{dt} = \frac{R_{PtO} - R_3}{\Gamma} - \frac{2\theta_{PtO}}{r_{Pt}} \frac{dr_{Pt}}{dt} \tag{68}$$

where Γ is the maximum platinum oxide sites at the surface.

The change in concentration is a function of the platinum dissolution and platinum oxide dissolution rates. The equation was set to include the diffusion of platinum ions in the ionomer pore network, as well as the diffusion from the CCL-PEM boundary into the membrane which accounted for the platinum band formation. Thus, the following pore network discretization of the transient reaction-diffusion equation, for a pore i and neighbours j, was used:

$$\frac{dc_{Pt^{2+},i}}{dt} = \frac{1}{V_{p,i}} \left[\sum_j G_{ij} \left(c_{Pt^{2+},j} - c_{Pt^{2+},i} \right) + n_{Pt,i} A_{Pt,i} \left(R_{diss,i} + R_{3,i} \right) + Y_i \right] \tag{69}$$

where V_p is the pore volume and $n_{Pt,i}$ is the number of platinum particles in each pore. The active platinum area, $A_{Pt,i}$, and the diffusive conductance, G_{ij}, is defined previously in the performance model section. In this case, the diffusivity of platinum ions in the ionomer, $D_{Pt^{2+},ion}$, is used.

Y_i is an added term that accounts for the diffusion of platinum ions into the membrane band which is located at a distance x_{band} away from the CCL, where precipitation of platinum occurs.

$$Y_i = \begin{cases} -D_{Pt^{2+},ion} A_{CCL} \dfrac{c_i}{x_{band}}, & i \text{ in the membrane boundary} \\ 0, & \text{otherwise} \end{cases} \quad (70)$$

3.4 Results and Discussion

3.4.1 Model Calibration

3.4.1.1 Performance Solver Calibration

The performance solver was calibrated to match the experimental data reported by Braaten et al. [135], specifically on the performance of the Vulcan-supported platinum catalysts (Pt/Vu). This is achieved by fitting to the polarization curve at BOL conditions. The resulting fitted polarization curve is shown in Figure 3-8a, and the parameters used for the performance solver are shown in Table 3.2.

Note that the accuracy in the mass transfer loss region (i.e., at voltages below 0.4 V) was not prioritized during fitting, as no experimental data is available in this region and AST protocols typically do not operate at voltages below 0.4 V.

Table 3.2: Parameters used in performance solver

Symbol	Description	Value	Units	Reference
$\boldsymbol{D_{O_2,ion}}$	Oxygen diffusivity in the ionomer	$7.0 \cdot 10^{-10}$	$m^2\ s^{-1}$	[146]
$\boldsymbol{\alpha_{a,ORR}}$	Anodic charge transfer coefficient of the ORR reaction	1.0	–	[132]
$\boldsymbol{\alpha_{c,ORR}}$	Cathodic charge transfer coefficient of the ORR reaction	0.95	–	[132]
$\boldsymbol{n}$	Number of electrons transferred in the overall reaction	4	–	–
$\boldsymbol{z}$	Number of electrons transferred in the rate limiting step	1	–	–

$\boldsymbol{\phi_{PEM}}$	Potential at the ACL-membrane interface	0	V	Assumed
$\boldsymbol{E_{eq}}$	Open-circuit voltage	1.2	V	–
$\boldsymbol{L_{PEM}}$	Membrane thickness	20	µm	[135]
$\boldsymbol{L_{GDL}}$	GDL thickness	270	µm	[135]
$\boldsymbol{\lambda_{Pt}}$	Platinum loading	0.1	mg cm^{-2}	[135]
$\boldsymbol{\varepsilon_{GDL}}$	GDL porosity	0.8	–	Assumed
$\boldsymbol{\tau_{GDL}}$	GDL tortuosity	3.0	–	Assumed
$\boldsymbol{\frac{j_0}{c_0}}$	Exchange current density and reference oxygen concentration ratio	$2.14 \cdot 10^{-4}$	A m mol^{-1}	Fitted

3.4.1.2 Degradation Solver Calibration

As highlighted earlier, the high diffusivity of platinum species at the nanoscale causes numerical stiffness, requiring small timesteps and increased computational cost. Thus, analyses were limited to five cycles. While this restricts long-term prediction, the model can still resolve early-stage degradation, and five cycles were sufficient to reveal these trends.

To calibrate the degradation solver with Braaten et al. [135], an empirical model was created from interpolated catalyst data at different cycles. Mass loss was chosen as the calibration basis. While ECSA loss shows similar trends under cycling [58] and could also be used for fitting, mass loss was deemed more appropriate as it directly captures dissolution-driven mechanisms and platinum loss to the membrane band. In contrast, ECSA loss is additionally influenced by long-term mechanisms such as particle coalescence and detachment due to carbon corrosion, which are not included in this model and are assumed to be negligible over the short timescales considered. Consequently, calibration using mass loss provides a more direct representation of the modeled degradation mechanisms.

An empirical expression developed for ECSA loss [43] describing exponential decay toward a non-zero asymptote, was adapted for mass loss:

$$M = (1 - M_{min})\, exp[-kN] + M_{min} \tag{71}$$

where M is the fraction of mass remaining and M_{min} and k are parameters. Fitting to experimental data gave $M_{min} = 0.882$ and $k = 1.77 \cdot 10^{-4}$. The empirical model was then used to calibrate degradation solver parameters. The solver was run with the AST protocol of Braaten et al. [135] which consisted of a

trapezoidal voltage cycle with lower and upper potential limits of 0.6 and 0.95 V, respectively, with 2.5 s of hold time and 0.5 s of ramp time. The platinum band location was also obtained from the data from Braaten et al. [135], showing a platinum band formation after 30k cycles at around 3.2 μm away from the CCL. The fitted mass loss simulation is shown in Figure 3-8b, and the parameters used for the degradation solver are shown in Table 3.3.

Table 3.3: Parameters used in the degradation solver

Symbol	Description	Value	Units	Reference
k_{diss}	Rate constant of dissolution	$5.25 \cdot 10^{-7}$	mol m^{-2}s^{-1}	Fitted
$\alpha_{diss,a}$	Anodic transfer coefficient for the dissolution reaction	0.5	–	[51]
$\alpha_{diss,c}$	Cathodic transfer coefficient for the dissolution reaction	0.5	–	[51]
n_{diss}	Number of electrons transferred in the dissolution reaction	2	–	–
$c_{Pt^{2+}}^{ref}$	Reference platinum ion concentration	1000	mol m^{-3}	[58]
U_{diss}^{θ}	Standard potential for the dissolution reaction	1.188	V	[51]
σ_{Pt}	Surface tension of platinum	2.37	J mol^{-1}	[51]
M_{Pt}	Molar mass of platinum	0.195	kg mol^{-1}	–
ρ_{Pt}	Density of platinum	$2.145 \cdot 10^{4}$	kg m^{-3}	–
k_{PtO}	Rate constant of platinum oxide formation	$1.5 \cdot 10^{-7}$	mol m^{-2}s^{-1}	Fitted
ω_{PtO}	Platinum oxide interaction parameter	$3 \cdot 10^{4}$	J mol^{-1}	[51]
$\alpha_{PtO,a}$	Anodic transfer coefficient for the oxide formation reaction	0.35	–	[51]
$\alpha_{PtO,c}$	Cathodic transfer coefficient for the oxide formation reaction	0.15	–	[51]
n_{PtO}	Number of electrons transferred in the oxide formation reaction	2	–	–

$c_{H^+}^{ref}$	Reference proton concentration	375	mol m^{-3}	Fitted
EW	Equivalent weight of the ionomer	1.1	kg mol^{-1}	[76]
M_{H_2O}	Molar mass of water	0.018	kg mol^{-1}	–
$U_{PtO}{}^{\theta}$	Standard potential for the oxide formation reaction	0.98	V	[51]
$\Delta\mu_{PtO}^{0}$	Chemical potential shift	$-4.23 \cdot 10^{4}$	J mol^{-1}	[51]
σ_{PtO}	Surface tension of platinum oxide	1.00	J mol^{-1}	[51]
M_{PtO}	Molar mass of platinum oxide	0.211	kg mol^{-1}	–
ρ_{PtO}	Density of platinum	$1.4 \cdot 10^{4}$	kg m^{-3}	–
k_3	Rate constant of the oxide dissolution reaction	$3.2 \cdot 10^{-20}$	mol $m^{-2}s^{-1}$	[51]
Γ	Maximum oxide sites at platinum surface	$2.18 \cdot 10^{-5}$	mol m^{-2}	[58]
$D_{Pt^{2+},ion}$	Diffusivity of platinum ions in the ionomer	$4 \cdot 10^{-11}$	m^2 s^{-1}	[147]
x_{band}	Location of the platinum band (distance from the PEM-CCL interface)	3.2	µm	Measured from [135]

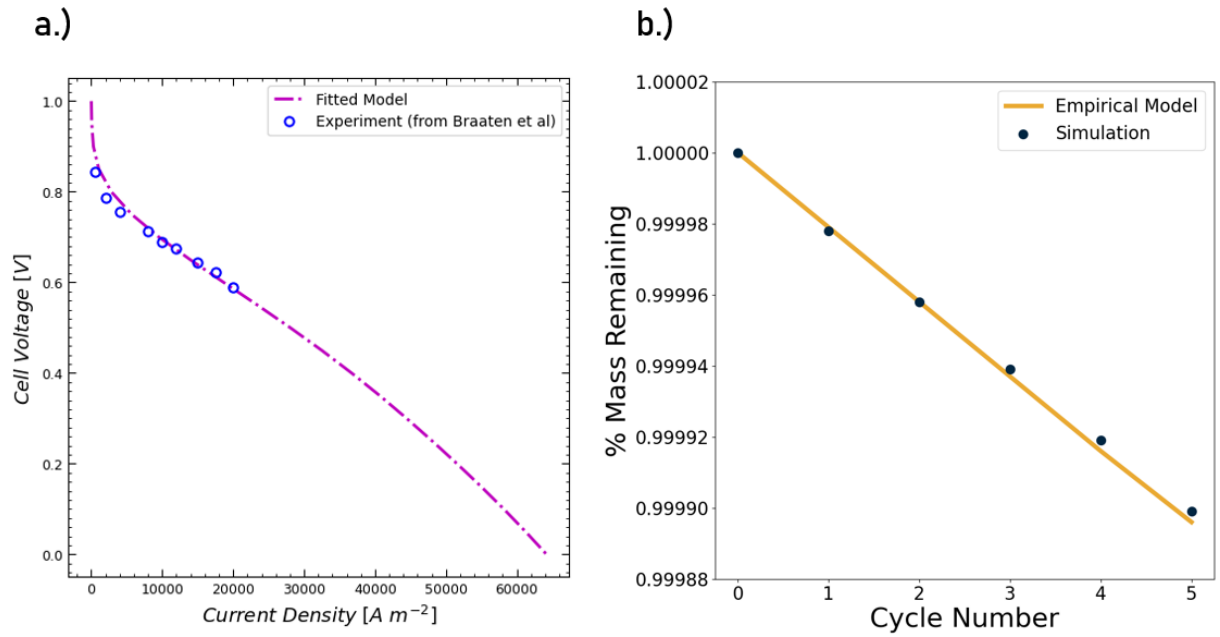


Figure 3-8: a.) Polarization curve of the fitted model compared to experimental data from Braaten et al. b.) Empirical mass loss model curve in the first five cycles plotted with the fitted mass loss simulation data from the degradation model

3.4.2 Oxygen Transport and Overpotential at Different Voltages

Pore-scale variations in oxygen concentration and overpotential are resolved using the performance solver. Figure 3-9a shows the spatial distribution of oxygen concentration within the CCL at various cell voltages. As the current density increases (i.e, as the cell voltage decreases), two key trends emerge: (1) oxygen depletion becomes more significant near the CCL-PEM interface due to higher local proton concentrations, leading to increased ORR reaction rates, and (2) pores located near or directly connected to the void phase exhibit higher dissolved oxygen concentrations than interior pores, demonstrating the effect of intra-agglomerate oxygen transport. This highlights the ability of the model to resolve variations in oxygen concentration within individual agglomerates. Figure 3-9b shows the overpotential distribution of the pore network at different voltages. The overpotential is consistently higher near the CCL-GDL interface, where the longer proton transport paths result in increased ohmic losses. Furthermore, the overall overpotential decreases as cell voltage is reduced, with the gradient across the network becoming steeper. Since the platinum degradation reactions are driven by the potential difference between the solid and electrolyte phases (i.e., the overpotential subtracted by the open-circuit voltage), the degradation model will also capture the spatial variations in reaction rates, which will be more pronounced at lower voltages.

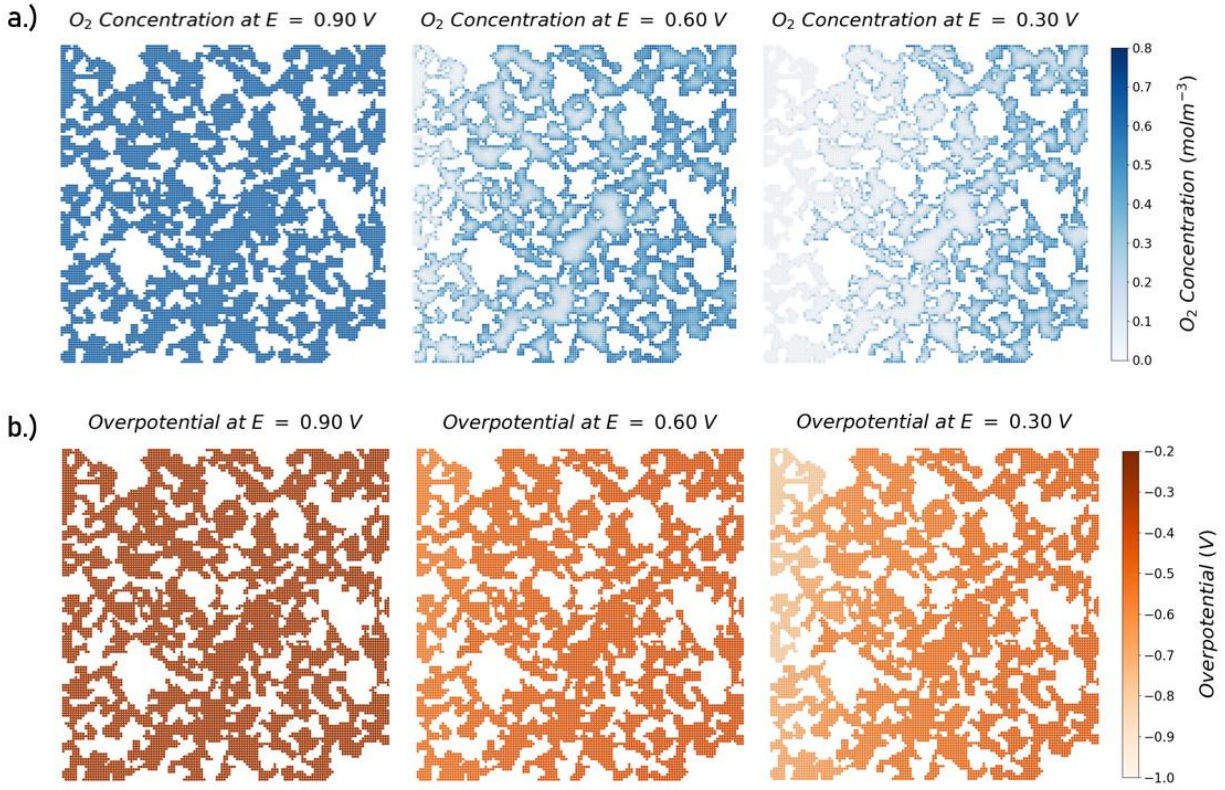


Figure 3-9: Images of the pore network CCL showing a.) oxygen concentration and b.) overpotential for each pore at cell voltages of 0.9 V, 0.6 V, and 0.3 V. The left side of each image corresponds to the PEM-CCL interface, while the right side corresponds to the CCL-GDL interface

3.4.3 Temporal and Spatial Trends of Degradation

To observe the degradation behaviour and platinum loss, a simulation was run for five cycles using the same trapezoidal AST protocol used in the degradation solver calibration.

After optimizing data storage and processing, each degradation cycle (6 seconds) currently requires approximately 30 minutes of computation time using the current solvers. The simulations (performed on a network with ~9,300 pores) were run on a workstation equipped with an Intel Core i9-14900F processor and 64.0 GB of RAM. About 85% of this runtime is attributed to the degradation solver, owing to the stiffness and interdependence of the transient equations. Possible improvements to the solvers are discussed in the Conclusions.

For the initial conditions, the platinum oxide coverage and platinum ion concentrations were both set to 0, and the platinum size PSD was assumed to have a mean platinum radius of 2.4 nm (calculated using ECSA

data at BOL), and follow a lognormal distribution ($\mu = 2.4$, $\sigma^2 = 0.1$) with the particles ranging from ~1.5 nm to ~3.5 nm. The platinum sizes are randomly distributed spatially.

The degradation behaviour predicted by the model is shown in terms of the evolution and variation of surface area loss, platinum oxide coverage, and platinum ion concentration. Each of these is discussed in turn below.

3.4.3.1 Surface Area Loss

Figure 3-10 shows the evolution of the platinum surface area in each pore normalized by the initial surface area (at BOL). With each subsequent cycle, the total surface area of platinum sites decreases due to dissolution and loss of platinum into the membrane. However, this surface area loss is not distributed uniformly. First, there are significant variations in surface area loss even within individual agglomerates and between neighboring pores. This is a result of the imposed random spatial distribution of platinum particle sizes. Due to electrochemical Ostwald ripening, smaller particles have a higher tendency to dissolve than larger ones, and leads to larger particles dissolving less or even gaining surface area over time. Second, a noticeable drop in surface area is observed in pores close to the PEM-CCL interface (left side of each image). This is attributed to platinum loss into the membrane. These two effects correspond to the primary cause of platinum surface area loss identified by Shao-Horn et al. [41].

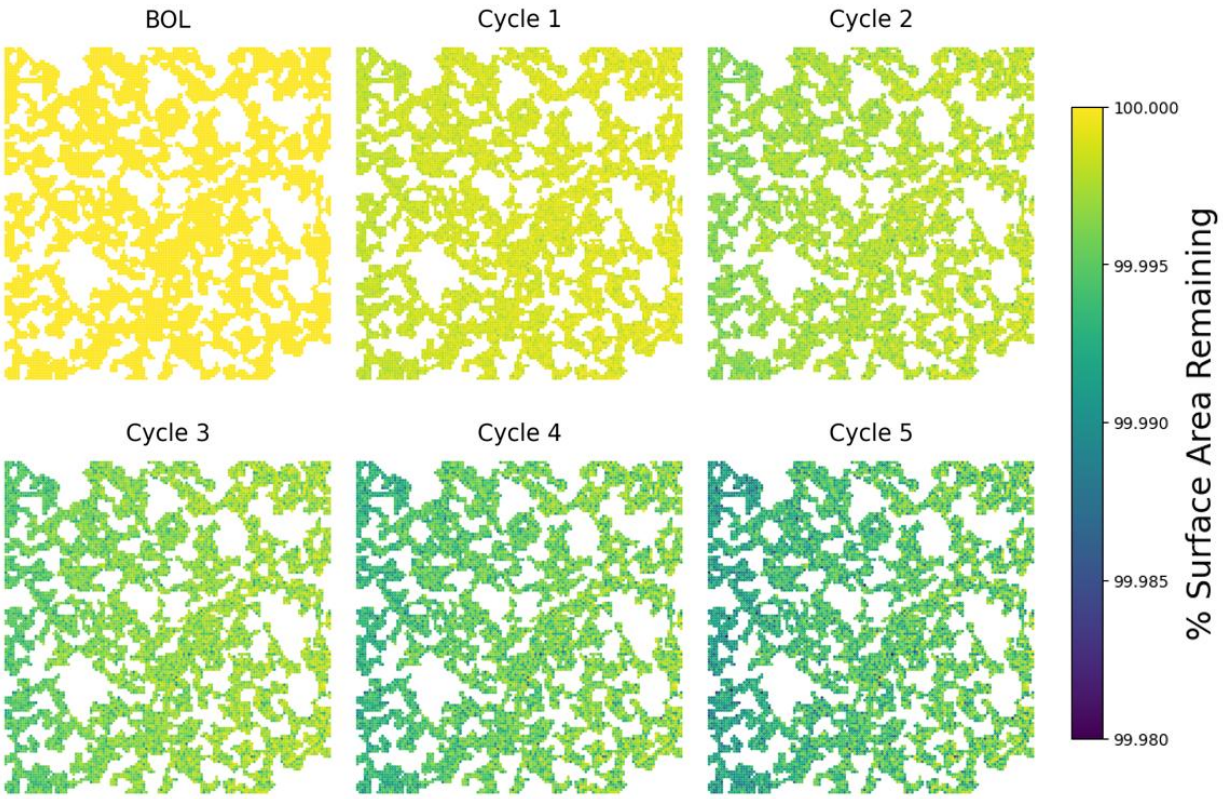


Figure 3-10: Map of the CCL by cycle in terms of surface area remaining for the platinum sites in each pore, relative to the initial surface area. The PEM-CCL interface is on the left side of each image and the CCL-GDL interface is on the right.

The surface area profiles are shown in Figure 3-11a, which plots the slice-averaged percent platinum surface area (i.e., percent surface area averaged within each x-position voxel) as a function of distance from the membrane. These results support the visual observations from Figure 3-10, confirming that surface area loss is most pronounced near the PEM-CCL interface, and is consistent with previously reported trends [81], [132]. Figure 3-11b presents a 3D surface plot of the percentage of slice-averaged surface area loss as a function of both time and distance from the membrane. This plot illustrates how surface area evolves during each AST cycle, particularly as the cell voltage oscillates between the upper and lower potential limits (UPL and LPL, respectively). The figure shows that surface area loss predominantly occurs during the UPL phase, when the platinum dissolution rate is elevated, whereas the surface area remains relatively stable during the LPL phase due to suppressed dissolution.

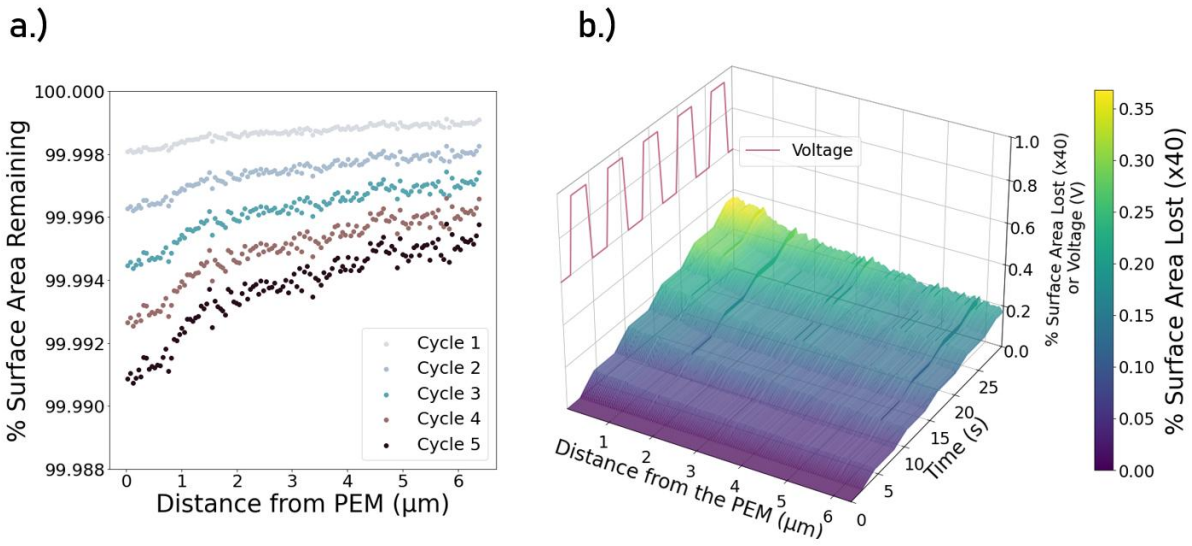


Figure 3-11: Profiles of slice-averaged surface area remaining plotted by distance from PEM at the end of each cycle. b.) 3D surface plot representing the slice-averaged surface area lost plotted with distance from the membrane and time. The surface area lost is multiplied by a factor of 40 and the voltage cycling is displayed on the y=0 plane to show the effects of voltage cycling on surface area lost

3.4.3.2 PtO Formation and Pt^{2+} Concentration

In addition to surface area loss, cyclic trends in oxide coverage and platinum ion concentration are important, as both species influence the dissolution rate during voltage cycling[50].

Figure 3-12a shows the average oxide coverage in the first cycle, plotted with the cell voltage. Coverage remains near zero until the voltage rises from the LPL to the UPL, then increases steadily, reflecting the stronger driving force for oxide formation. Upon returning to the LPL, coverage decreases slowly, indicating sluggish reduction kinetics at the selected conditions. Figure 3-12b shows spatial maps at discrete time points. Coverage is mostly uniform, though by 6 s, pores near the PEM-CCL interface show slightly lower coverage than those farther away. This can be attributed to the electrolyte potential gradient where pores located farther from the membrane experience higher overpotentials, enhancing the kinetics of PtO formation. However, since the oxide coverage does not exceed 1, full passivation is not achieved, and higher dissolution rates are expected to occur at the upper potential limit (UPL). The lower coverage near the membrane also means more surface remains exposed, causing stronger degradation in this region.

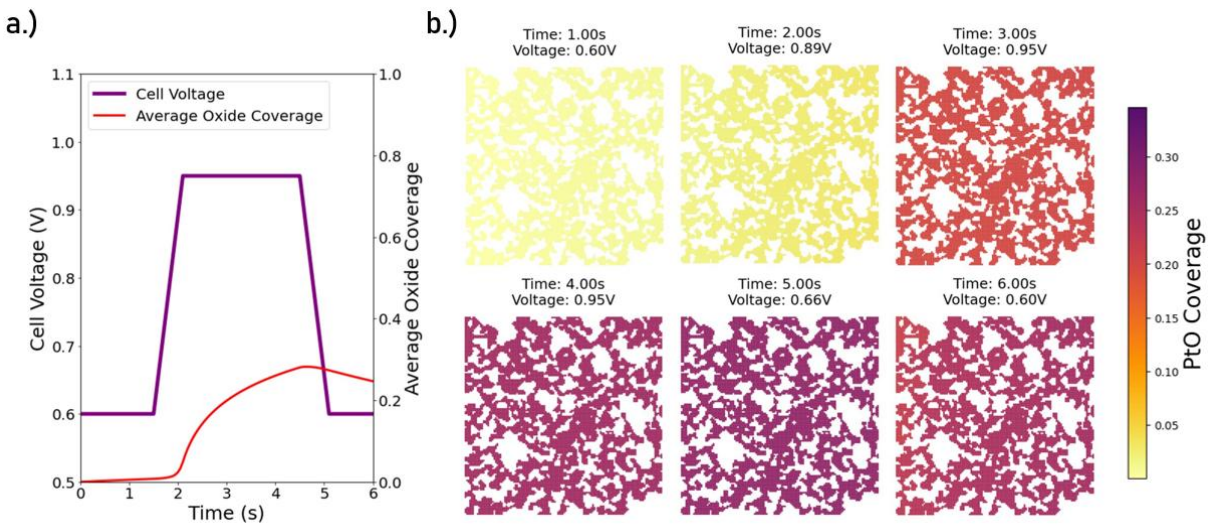


Figure 3-12: The a.) average oxide coverage of the platinum sites in the CCL during the first cycle is shown along with the b.) oxide coverage map of the CCL at discrete time points of 1, 2, 3, 4, 5, and 6 seconds. The PEM-CCL interface is on the left side of each image and the CCL-GDL interface is on the right.

Figure 3-13a plots the average platinum ion concentration over time. During the LPL, concentrations stay near zero, indicating minimal dissolution. As the voltage shifts to the UPL, concentrations rise sharply, then decline during the UPL hold, likely due to diffusion into the membrane and band deposition. When the voltage returns to the LPL, concentrations again approach zero. Figure 3-13b displays spatial concentration maps at the same time intervals. Notably, at 3 and 4 seconds, which are during the UPL phase, a concentration gradient forms, with the platinum concentration being higher near the GDL and lower near the membrane. This demonstrates ion transport toward the membrane, consistent with platinum loss into the band. Low ion accumulation near the PEM reduces the likelihood of redeposition, suppressing Ostwald ripening and further accelerating degradation near the interface [81].

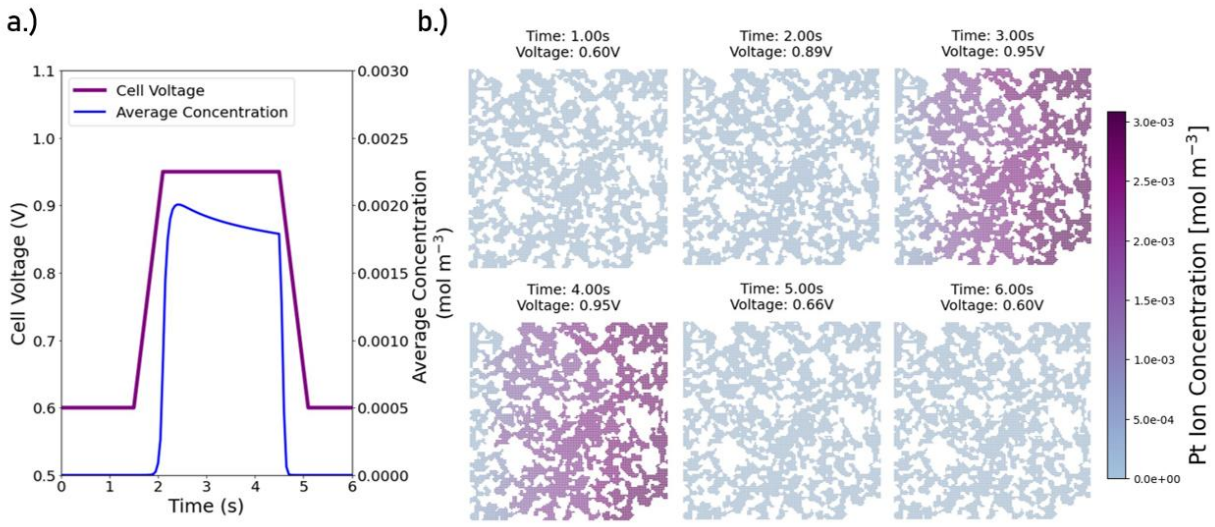


Figure 3-13: The a.) average platinum ion concentration in the CCL during the first cycle is shown along with the b.) platinum ion concentration map of the CCL at discrete time points of 1, 2, 3, 4, 5, and 6 seconds. The PEM-CCL interface is on the left side of each image and the CCL-GDL interface is on the right.

The temporal trends in Figure 3-12a and Figure 3-13a are consistent with observations by Zhang et al. [50]. The present model provides additional resolution in Figure 3-12b and Figure 3-13b by revealing the spatial and temporal behavior of oxide formation and platinum ion distribution within the CCL during cycling. To further visualize the cyclic effects, Figure 3-14a presents the slice-averaged platinum oxide coverage as a function of distance from the membrane and time, while Figure 3-14b shows the corresponding slice-averaged platinum ion concentration. These 3D surface plots show comparable behavior to the 1D continuum model of Kovtunenko and Karpenko-Jereb [82] who simulated square-wave voltage cycling using the Holby-Morgan [77] kinetic model of platinum dissolution and oxidation. Although their cycling parameters and operating conditions, such as catalyst layer thickness, platinum loading, and temperature, differ slightly from those used in this work, the spatial trends in PtO coverage, Pt ion concentration, and surface area loss (reflected by decreasing platinum particle diameter) are qualitatively similar. In both models, greater surface area loss and lower Pt ion concentrations occur near the membrane, while PtO coverage remains approximately uniform across the catalyst layer. The smoother spatial profiles in Kovtunenko and Karpenko-Jereb's surface plots stem from their 1D continuum representation, whereas the present 2D pore-scale approach captures node-level variations and local heterogeneity within the structure. This comparison highlights the added value of resolving degradation at the pore scale, where localized transport and reaction can be explicitly visualized.

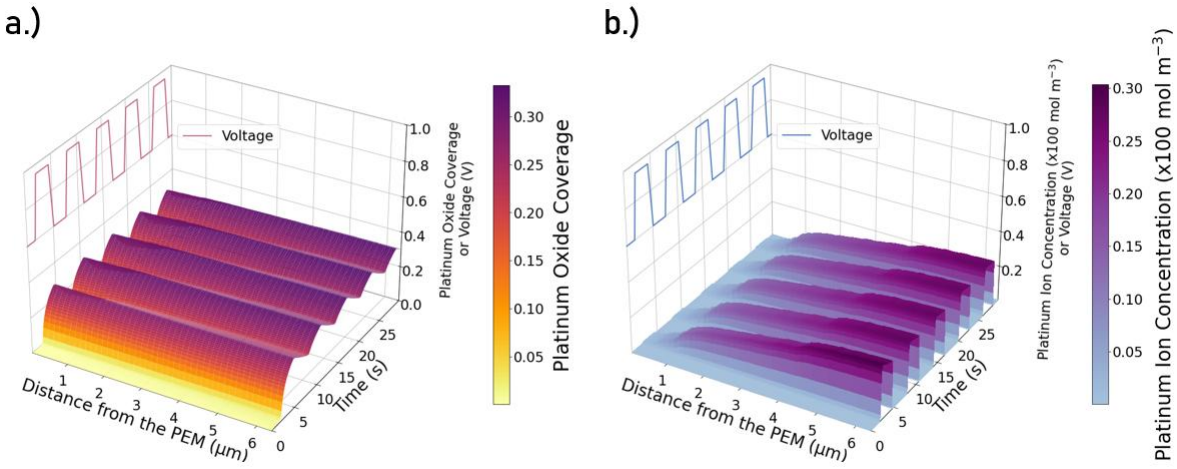


Figure 3-14: 3D surface plots with distance from the PEM and time of a.) oxide coverage and b.) platinum ion concentration (multiplied by a factor of 100), both averaged in the x-position. In both graph, the voltage cycling is displayed on the y=0 plane to show the effects of voltage cycling

3.4.4 Effects of the Pore Structure

In addition to reproducing known degradation trends at pore-scale resolution, the present model also reveals how pore structure influences degradation. Key insights from the geometry studied include higher degradation in agglomerates near the membrane and a correlation between degradation and platinum ion transport length.

3.4.4.1 Agglomerate Constrictions

Figure 3-15 shows the surface area remaining after cycle 5, with part (a) displaying the spatial map and part (b) the slice-averaged profile versus distance from the PEM-CCL interface. A more intense colormap was chosen to emphasize differences, and a moving average highlights trends. A distinct increase in surface area loss is observed near the PEM, with a steeper slope indicating stronger degradation in this region. Figure 3-15a, further shows that agglomerates directly connected to the PEM lose surface area more sharply than the rest of the CCL, highlighted by red dashed lines in both panels. Closer examination of the map reveals the presence of constricted pathways between PEM-connected agglomerates and its connected agglomerates. The constricted pathways between agglomerates are localized transport limitations arising within the generated 2D structure. Similar narrow connections between agglomerates can be observed in 3D structures [148], though their effect is expected to be less pronounced due to higher connectivity in 3D.

This suggests that agglomerate constrictions can spatially confine degradation effects within the conditions and assumptions of the model. The reduced surface area loss in the interior of the CCL can be attributed to

increased transport resistance for platinum ions in those constrictions, limiting their diffusion toward the membrane and subsequent loss. This insight implies that intentionally introducing transport bottlenecks near the membrane could help mitigate losses related to platinum dissolution by slowing ion migration and reducing membrane loss. This conclusion assumes that other degradation mechanisms affecting the pore structure, such as carbon corrosion, remain minimal under the studied conditions, and future work will be needed to examine how these processes may interact with the observed effect.

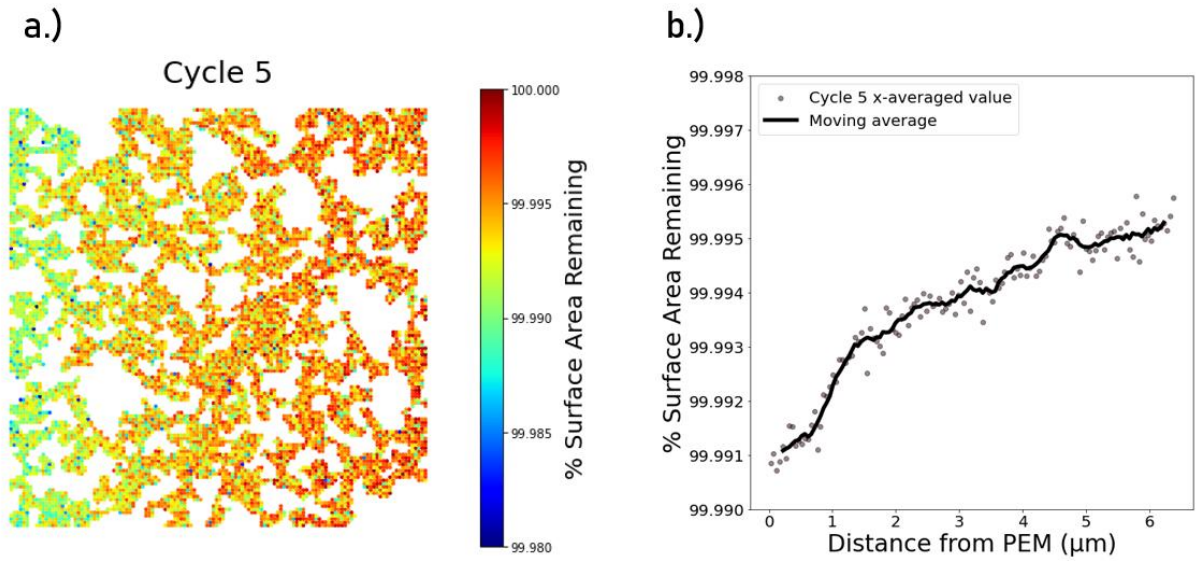


Figure 3-15: a.) Map of the surface area remaining after cycle five and b.) scatter plots of the slice-averaged surface area values at each x-coordinate, together with their moving average. In both plots, the red dashed line represents the location at which there is an observed shift in the degradation behaviour, with the pores on the left of the line showing a steeper and more drastic degradation

3.4.4.2 Influence of Transport Length

Because platinum ion transport plays a key role in degradation, and given the complex porous nature of the CCL, the actual transport length between the membrane and each pore was computed to help correlate local structure with degradation behavior. This differs from simply measuring the straight-line x-distance, as transport paths in porous media are longer due to tortuous geometries. Analysis in terms of actual transport length offers a more physically representative metric for degradation correlation and is only accessible through a full pore-scale model.

Transport length was calculated using Dijkstra's algorithm to find the shortest distance from each pore to the membrane boundary pores. Figure 3-16a shows calculated lengths, which generally increase with

distance from the interface but also vary locally; some agglomerates show particularly long lengths due to tortuous pathways.

To examine the effect of transport length on degradation, Figure 3-16b presents a scatter plot of surface area remaining after five cycles as a function of transport length. Here, several trends emerge. First, the points are colored by initial particle size, showing that larger particles degrade less and smaller particles lose more surface area through electrochemical Ostwald ripening. Second, most particles experience surface area loss, with only a few particles exhibiting size increase due to redeposition. This indicates that platinum dissolution and subsequent transport toward the membrane dominate over Ostwald ripening at these conditions. Third, there is a general inverse trend, where pores with shorter transport lengths tend to experience more surface area loss. This aligns with earlier observations that degradation is more severe near the PEM interface. Notably, the pores with the least degradation exhibit both long transport lengths and large particle sizes. These figures highlight how the model could enable a more nuanced and statistical analysis of degradation patterns, providing site-specific insights and observations on degradation behaviour.

It should be noted that the 2D model has inherent limitations, as it cannot fully capture the three-dimensional connectivity and structure of the catalyst layer. In 3D networks, each node has more possible connections, leading to more percolation pathways. For the same network generation parameters, this improved connectivity will likely result in lower tortuosity and, consequently, shorter transport lengths. Due to better connectivity, the constrictions between agglomerates may also play a lesser role in isolating localized degradation effects. As a result, the observed behaviors are expected to differ quantitatively between 2D and 3D domains. Nevertheless, the underlying trends observed in this work are expected to remain qualitatively valid in three-dimensional catalyst layers, albeit with reduced magnitude.

Together, the effects of constrictions and transport length suggest that tortuous ion pathways suppress degradation. This is counterintuitive, as high tortuosity also hinders oxygen and proton transport, which are critical to the ORR. Thus, there is an important design trade-off to be analyzed between minimizing degradation and maintaining performance. This highlights the need for the optimization of CCL microstructures to balance durability and performance.

Additionally, the observed relationship between surface area loss, transport length, and platinum particle size suggests that the catalyst layer could benefit from an engineered spatial distribution of platinum sizes. Specifically, placing larger, more stable particles in regions with shorter transport lengths and smaller particles where ion transport paths are longer may reduce overall degradation. A simplified version of this strategy has been implemented in gradient catalyst layers [113], [149], where larger particles are placed

near the membrane to mitigate platinum loss. With the current model, it becomes possible to derive a more detailed and quantitative relationship between transport length and optimal platinum size. This can inform the design of more sophisticated spatial distribution schemes that account for the CCL's pore structure and its influence on localized degradation.

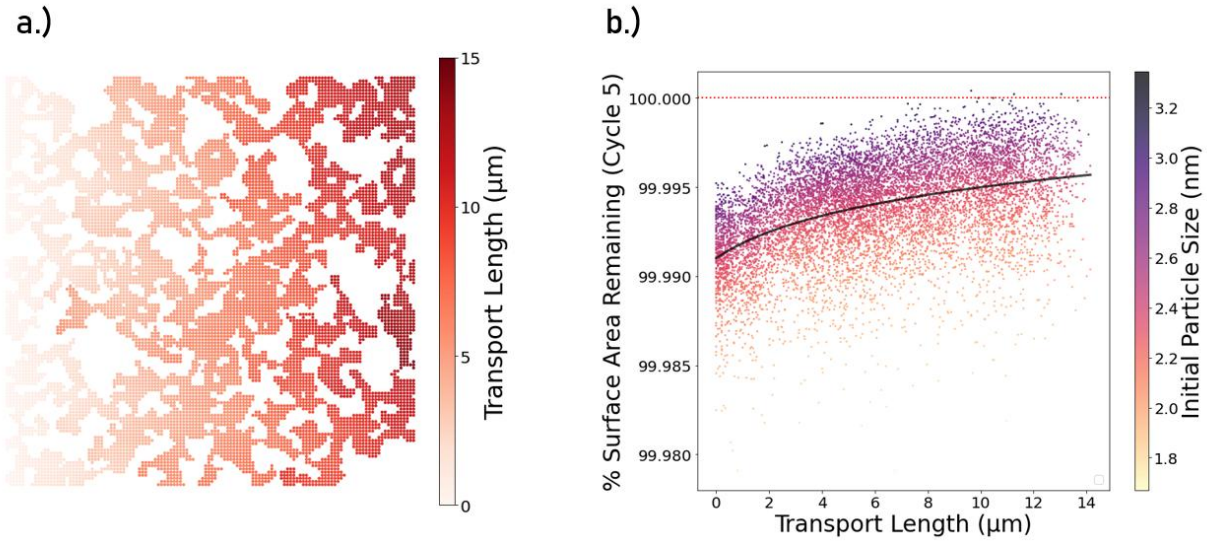


Figure 3-16: a.) Coloured map of the transport length values for each pore in the CCL. b.) Surface area remaining for each pore plotted with the transport length and coloured by initial platinum size.

3.5 Conclusions

In this work, a transient two-dimensional pore-scale model was developed to simulate platinum degradation in the CCL of PEMFCs. The model was constructed using pore network modeling, with the CCL represented as a single-phase ionomer network. Each pore contained platinum catalyst sites, allowing the simulation of both platinum ion transport and the dynamic evolution of local catalyst properties. The CCL geometry was artificially generated using a structure generation algorithm and validated by comparing the effective ionomer conductivity against values reported in the literature. The model incorporates a coupled performance-degradation framework where a performance solver computes local reaction rates for the ORR, while a degradation solver simulates platinum dissolution, oxide formation, and oxide dissolution. Platinum membrane loss was modeled by imposing a constant sink term at the membrane to represent Pt band formation. The model was calibrated using experimental polarization data at BOL conditions and mass loss data over five AST cycles, fitted through an empirical degradation equation.

The simulation results reproduce key previously observed degradation trends, now with pore-scale resolution. These include greater degradation near the membrane, preferential loss of smaller particles

(indicative of Ostwald ripening), and spatial variations in platinum oxide coverage and ion concentration. In addition to these known trends, the model provides new structural insights. For instance, degradation was found to be more pronounced in membrane-connected agglomerates that are separated by constrictions, suggesting that geometric bottlenecks can localize degradation. Further, when controlled for the platinum size, an inverse correlation was observed between degradation and transport length, which is the tortuous path platinum ions must travel to reach the membrane. These observations suggest that more tortuous or constricted microstructures may suppress platinum loss, though this optimization will need to be balanced with possible performance losses due to increased transport resistance.

This framework therefore offers a pathway toward optimizing CCL design. Future studies could employ it in multi-objective optimization schemes that minimize degradation while maximizing performance by tuning design parameters such as the ionomer-to-carbon ratio, agglomerate and pore size distributions, and ionomer coverage, as well as examining their dependence on operating and cycling conditions through systematic parametric analyses. The result also implies that tailoring the spatial distribution of platinum particle sizes based on local transport lengths can reduce degradation. This insight can support the design of engineered catalyst size distributions beyond current implementations, such as gradient structures, by accounting for pore-level transport behavior.

Despite these promising results, the model has several limitations. The present implementation is restricted to two dimensions, which limits connectivity and percolation behavior. While the 2D model cannot fully reproduce 3D transport pathways, the qualitative trends are expected to hold, albeit with reduced magnitude. Extending the framework to 3D will allow quantitative analysis of transport and degradation interactions. The model is also computationally intensive due to the small timesteps required for stability at nanoscale transport rates, limiting the number of simulated cycles. Additionally, other degradation mechanisms such as particle coalescence and detachment are not included. These mechanisms typically become more pronounced only after extended cycling and significant structural or support degradation, and thus are not expected to affect the short-term behavior captured in this study. Their inclusion in future work will allow accurate prediction of longer-term surface area loss.

These limitations motivate several directions for future work. Implementing implicit or iterative solvers, parallel and GPU computation, and model-order reduction can improve the model's computational efficiency. Expanding to 3D and simulating longer degradation periods would enable the study of evolving performance losses, such as changes in reactant transport pathways and gas-phase resistance as catalyst utilization decreases. Further extensions may also incorporate additional degradation mechanisms, structural evolution, and coupled physics that account for water and gas transport. In future work, this

framework could also be directly linked with experimental observations, for instance by comparing simulated degradation behaviour and patterns with operando tomography or degradation mapping.

Ultimately, the utility of the current model lies less in reaching end-of-life predictions and more in providing qualitative insights into the relationship between the catalyst layer structure, catalyst degradation, and fuel cell performance – something that is not captured by continuum and lumped models. This offers a powerful tool for investigating how modifications to CCL pore structure or catalyst placement strategies can mitigate platinum degradation and guide the design of more durable PEM fuel cells.

Chapter 4
Model-Informed Strategies for Mitigating Platinum Loss in PEM Fuel Cells

4.1 Overview

Building upon the previously developed transient pore network model in Chapter 3, this study then systematically investigated different microstructural and spatial design strategies enabled by the model's pore-scale resolution in order to investigate platinum degradation mitigation strategies while taking into account the fuel cell performance.

Several platinum degradation mitigation strategies have been explored in the literature, including both operational changes and material modification approaches [150]. On the materials side, experimental efforts have focused on modifying the electrode and catalyst structure, including graded cathode catalyst layers [151], [152], core-shell catalyst materials [153], [154], and replacement of platinum with platinum group metal-free catalysts [155]. Mitigation strategies have also been proposed through modeling studies. For instance, Zheng et al. [156] developed a one-dimensional continuum model and showed that reducing platinum ion transport into the membrane by shifting the platinum band away from the cathode or decreasing platinum ion diffusivity can enhance ECSA retention. Similarly, Baricci et al. [113] and later Zheng et al. [149] used a 1D continuum model to demonstrate that graded catalyst layers with larger platinum particles or higher platinum loading near the membrane can reduce degradation. The vast majority of existing platinum degradation models in literature use continuum modeling, which does not explicitly resolve porous microstructure of the CCL [157]. This limits the ability of modeling studies to investigate the role of detailed morphological features in the CCL. To the best of our knowledge, systematic investigations of the effects of cathode catalyst layer structure and structural properties on platinum degradation at the pore scale remain limited. A small number of studies have addressed related aspects. For example, Saeidfar et al. [158] examined the influence of bulk properties such as catalyst layer thickness, platinum loading, and platinum-to-carbon ratio on platinum degradation. However, the effects of explicit structural features such as porosity, pore size distribution, and spatial platinum placement have not been systematically isolated and studied even in experiments, as independently tuning these parameters in catalyst layers is challenging.

In Chapter 3, we developed a pore-scale model that simulates the transient degradation behaviour of platinum catalysts and is capable of explicitly resolving transport and degradation phenomena within the CCL [159]. This framework enables modification of pore-scale features while holding all other

parameters constant, which is difficult to achieve experimentally but straightforward through artificial geometry generation. In the present study, we focus on two types of degradation mitigation strategies that directly leverage the pore-scale resolution of the model: microstructural modification strategies and platinum placement strategies. While these approaches are not impossible to do with continuum-scale models, their implementation and interpretation are easier and more direct at the pore scale, where local transport pathways and degradation mechanisms can be explicitly resolved. The work in this chapter thus provides one of the first modeling insights into how explicit CCL structural features influence platinum degradation.

4.1.1 Hypotheses

For microstructural modifications, two approaches are examined: modifying catalyst layer porosity while keeping agglomerate size approximately constant, and modifying agglomerate size while keeping porosity constant. Platinum placement strategies are investigated by spatially varying the platinum loading while keeping the total platinum loading constant. Based on existing literature and understanding of transport behaviour on porous media, the next subsections outline our hypotheses.

4.1.1.1 Porosity Strategies

We hypothesize that increasing porosity will reduce platinum loss by increasing transport resistance for dissolved platinum species, particularly when high-porosity regions are located near the membrane, based on results from the previous modeling study. However, increased porosity and associated transport constrictions are also expected to hurt the initial performance due to increased mass transport and ohmic resistance. To examine this trade-off, three porosity modification strategies are considered: spatially uniform porosity, spatially graded porosity, and stepwise porosity changes representing localized geometric constrictions at different parts of the CCL. For all cases, higher porosity, especially near the membrane, is hypothesized to reduce platinum degradation while negatively affecting performance.

4.1.1.2 Agglomerate Size Strategies

We hypothesize that variations in agglomerate size will not significantly affect platinum degradation when porosity and ionomer content are held constant and agglomerate sizes remain within a practical range. Under these conditions, network connectivity and percolation are preserved, and transport pathways for dissolved platinum species are expected to remain largely unchanged. This assumption is consistent with classical porosity-tortuosity relationships [160], [161], [162] and packed-bed analogies [163] for self-similar porous media, in which tortuosity is governed by porosity rather than the pore sizes. Although, we expect that smaller agglomerate sizes will improve initial performance by enhancing

oxygen accessibility to catalytic sites and increasing agglomerate surface area for oxygen dissolution [164]. These performance benefits may allow agglomerate size reduction to be combined with porosity-based strategies to improve durability without sacrificing initial performance.

4.1.1.3 Platinum Placement Strategies

Previous studies by Yu and Baricci et al. [113], [151], [152] on graded catalyst layers have demonstrated improved durability when platinum loading is increased near the membrane, either through larger particle sizes or higher particle number density, although these studies didn't control for overall platinum loading which would have enhanced comparability. Motivated by these findings, two platinum placement strategies are examined here: spatial variation of platinum loading via particle size variation and via particle number density variation. We hypothesize that both approaches will reduce platinum degradation relative to a uniform loading case.

Following the formulation of these hypotheses, the methods for geometry generation and model implementation are described, and a validated and calibrated base case is established. Each strategy is first examined in isolation to identify its individual impact on performance and degradation behavior, followed by a case study that combines selected strategies. The limitations of the modeling approach are then discussed, and the study concludes with recommendations and opportunities for future work aimed at improving catalyst layer durability.

4.2 Methods

The methods used in this study, including geometry generation, governing equations and assumptions, and calibration procedures, largely follow those presented in Chapter 3. The primary difference is that the present study employs a three-dimensional catalyst layer geometry, rather than the simplified two-dimensional geometry used in the previous study. This modification was introduced to capture a more realistic representation of catalyst layer morphology. All model components and procedures were readily extended to the 3D geometry.

4.2.1 Base Case

A base case is first constructed to serve as the reference configuration against which the effects of various strategies on performance and platinum loss are evaluated. This base case is calibrated to experimental data and is largely based on the previous study, which follows the results of Braaten et al. [135]. The base case is defined by a spatially uniform porosity of 0.45, an average agglomerate diameter of approximately 180 nm, an ionomer-to-carbon ratio of 0.8, a spatially uniform platinum loading of 0.1 mg cm^{-2}, and an

average platinum particle radius of 2.4 nm, resulting in an average number density of ~26 platinum particles for each ionomer pore.

4.2.2 Catalyst Layer Construction and Validation

4.2.2.1 Image Generation

An artificial catalyst layer microstructure is first generated using PoreSpy [136] using the `blobs` function. This algorithm generates a random noise field over an image domain, applies a Gaussian blur, and then thresholds the result to produce a binary image consisting of solid and void phases. The algorithm inputs the following parameters: the porosity, ε, which defines the void fraction of the image, and a blobiness parameter, β, which controls the characteristic size of the generated features. In the context of this study, the blobiness parameter is related to the size of the solid ionomer agglomerates, with larger β yielding more agglomerates of smaller size.

To ensure comparability between different microstructures, particularly when assessing mitigation strategies that modify the catalyst layer morphology, the blob generation algorithm was slightly modified. Instead of thresholding the entire image to obtain a specific porosity, the algorithm applied the same threshold to each layer in the through-plane direction ensure the porosity profile was constant throughout the domain. This approach enables controlled investigation of both uniform and spatially varied porosity profiles across the catalyst layer thickness. This modification was verified to result in tortuosity distributions comparable to those produced by the original blob algorithm, as demonstrated through multiple test simulations. Additional details and validation of this modification are provided in Appendix A.

4.2.2.2 Network Construction and Validation

The same assumptions and procedures used in the previous study were applied to network construction. Each voxel of the generated image is treated as an ionomer node with implicitly modeled platinum particles. Voxels removed from the image correspond to the void phase, while carbon particles are represented implicitly as the spaces between ionomer nodes and edges. Figure 4-1a shows the resulting 3D geometry of the base case, which has a voxel resolution of 130x15x15. This resolution was assumed to be sufficient to capture the transport properties of the CCL while preserving meaningful morphological features, particularly in the through-plane direction, without introducing additional network complexity or computational cost.

The constructed network and geometry are validated using two independent criteria. First, effective protonic conductivity curves are evaluated to confirm that the 3D network reproduces realistic ionomer conductivity behavior, following the model range in Olbrich et al. [140]. The results are shown in Figure 4-1b. The free geometric parameter in this validation is the throat radius, r_t, which is varied between $r_t =$ 0.1*min(r_p) and $r_t = 0.8$*min(r_p), where min(r_p) is the radius of the smaller pore in the pore-throat-pore conduit. This was the range that was identified to keep it geometrically consistent, since the throat radius range is restricted by the I/C ratio, and extreme values of the throat radius can force compensating changes in throat length that produce unphysical geometries. Compared to the 2D geometry used previously [159], the feasible throat radius range is slightly higher due to the increased connectivity and percolation inherent to the 3D structure. Nevertheless, it remains within the feasible range. An intermediate value of $r_t = 0.5$*min(r_p) is arbitrarily selected for the base case. Second, the agglomerate size distribution is evaluated to ensure that the generated microstructure represents typical catalyst layer morphology. The agglomerate size distribution is computed using PoreSpy's local thickness filter applied to the solid phase. Figure 4-1c compares the resulting distribution to experimental agglomerate size data reported by Epting and Lister [137], obtained via nano-computed tomography of a cathode catalyst layer. The base case geometry exhibits an average agglomerate diameter of 182 nm, in close agreement with the experimentally reported value of 188 nm, indicating that the morphology is representative of a CCL.

4.2.3 Degradation Model Description and Calibration

As described in the previous work the model used in this study consists of a coupled performance solver and degradation solver using OpenPNM [124], [165]. The performance solver solves for the oxygen reduction reaction, while the degradation solver solves for platinum degradation mechanisms, including platinum dissolution, platinum oxide formation, and platinum oxide dissolution. Platinum mass loss through the membrane is also included in the degradation framework. The model is driven by a voltage function, represented by an accelerated stress test (AST). In this study, the U.S. Department of Energy (DOE) electrocatalyst testing protocol was employed, which was the same protocol used by Braaten et al. [135], consisting of a trapezoidal voltage cycling profile with lower and upper potential limits of 0.6 and 0.95 V, respectively, including a 2.5 s hold time at each potential and a 0.5 s ramp time between potentials.

The platinum catalyst particles initially follow a lognormal size distribution ($\mu = 2.4$ nm, $\sigma^2 = 0.1$), with particle radii ranging from approximately 1.5 nm to 3.5 nm. At the start of the simulation, no platinum oxide coverage is present, and the ionomer phase contains zero dissolved platinum ions.

Note that the model is limited to simulating five degradation cycles within a computationally feasible time due to the numerical stiffness of the coupled performance and degradation solvers. This is a known limitation of the framework, and substantial improvements to the solver would be required to enable long-term simulations. Therefore, the present model is not intended to directly predict long-term degradation behavior, nor does it capture phenomena dominant at extended timescales such as particle coalescence, complete particle dissolution, and carbon corrosion [42], [166]. Nevertheless, the insights obtained here remain meaningful as the model reproduces key spatial trends in platinum surface area loss and dominant degradation mechanisms, including platinum dissolution and Ostwald ripening, consistent with continuum models applied over similarly limited cycling durations [82]. Similar spatial degradation patterns and heterogeneities have also been reported in continuum-scale studies extended to thousands of cycles that likewise neglect the longer-timescale mechanisms mentioned [94]. In those cases, the same trends are observed but are more pronounced due to the extended cycling duration. Taken together, the results indicate that the model can reliably assess the relative impact of different mitigation strategies on general degradation trends. Importantly, the pore-scale resolution enables explicit modification of microstructural and spatial effects that are inaccessible to continuum models. Within the assumptions of the framework, the model provides comparative trends that may help compare structural design strategies. Nevertheless, the implications of the model's limitations are discussed further in the Results and Discussion section.

Model calibration was performed by fitting both performance and degradation to experimental data. Figure 4-1d shows the fitted polarization curve at beginning-of-life (BOL), while Figure 4-1e presents the platinum mass loss evolution fitted to empirical degradation data. Good agreement is observed in both cases, demonstrating the model's ability to capture the performance and degradation trends. The fitting parameters used in this study are summarized in Table 4.1. All remaining parameters are identical to those reported in the original work.

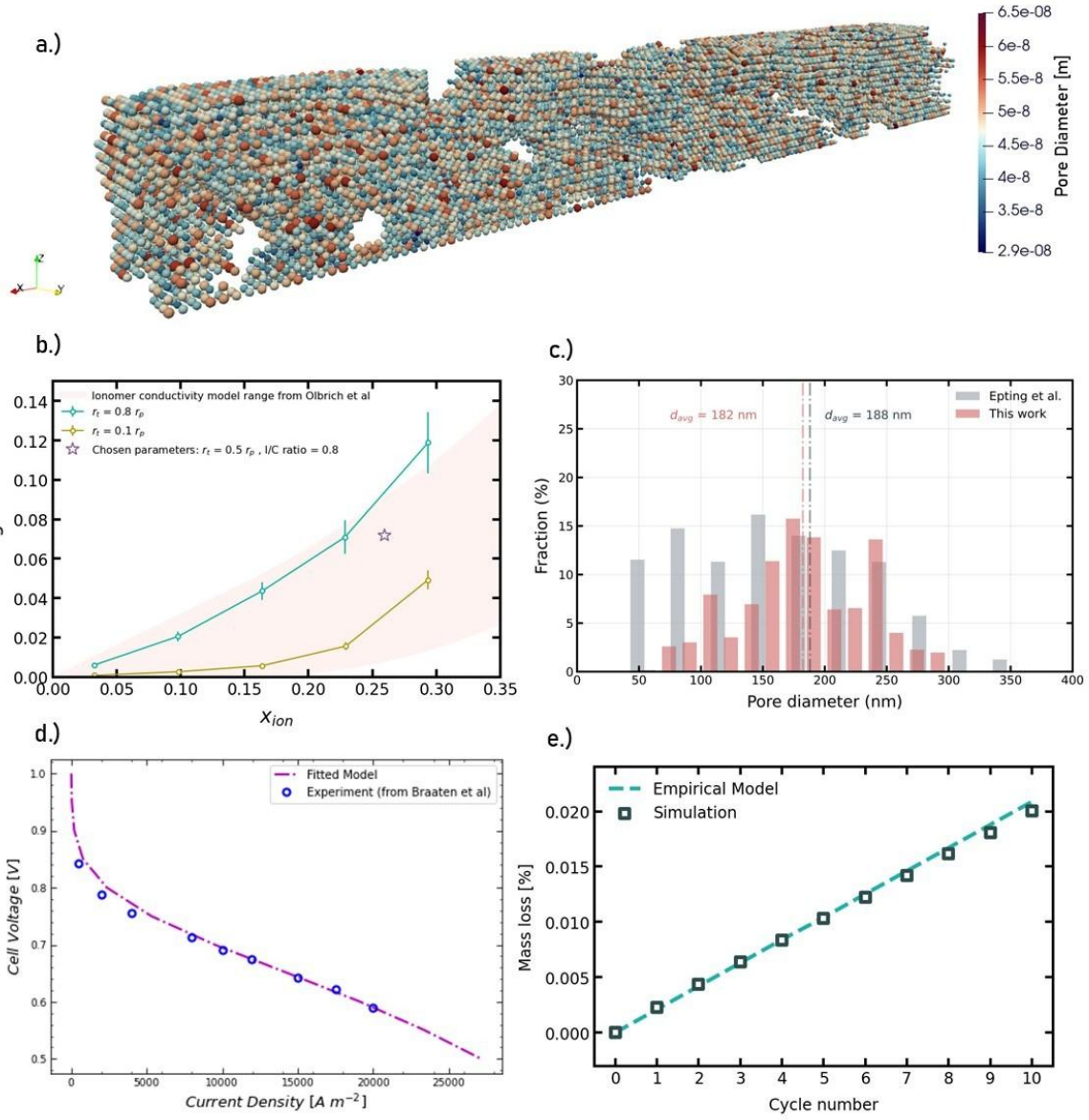


Figure 4-1: a.) 3D pore connectivity of the generated base-case CCL geometry. b.) Ionomer conductivity curves for the 3D networks generated with throat radii r_t=0.8*r_p and r_t=0.1*r_p, plotted together with the chosen parameter set applied in all simulations and overlaid with the ionomer conductfivity model range reported by Braaten et al. [135]. c.) Agglomerate size distribution of the base case compared with experimentally reported agglomerate size distribution data from Epting and Lister [137]. d.) Polarization curve fitted with experimental data from Braaten et al. [135]. e.) Mass loss curve fitted from empirical model [159]

Table 4.1 Fitting parameters from with the calibrated values used in this study

Fitting Parameter	Value	Unit
Exchange current density and reference oxygen concentration ratio, $\frac{j_0}{c_0}$	$7.14 \cdot 10^{-4}$	A m mol^{-1}
Rate constant of dissolution, k_{diss}	$5.50 \cdot 10^{-7}$	mol m^{-2} s^{-1}
Rate constant of oxide formation, k_{PtO}	$1.50 \cdot 10^{-7}$	mol m^{-2} s^{-1}
Reference proton concentration, k_{PtO}	375	mol m^{-3}

4.2.4 Metrics

To evaluate and compare the different strategies, we identified three independent criteria that should be assessed for each strategy relative to the base case: performance improvement, degradation reduction, and degradation homogeneity. Together, these metrics serve as indicators of a strategy's ability to improve both fuel cell durability and performance. Performance improvement was quantified by measuring current density at 0.6 V, degradation reduction was quantified by measuring the total electrochemically active surface area loss, and degradation homogeneity was evaluated using the coefficient of variation (CoV) of ECSA loss along the through-plane direction, where degradation heterogeneities are most pronounced. The rationale for selecting these metrics and their detailed definitions are provided in Appendix B.

4.2.5 Analysis

The following outlines the analyses performed for each category of strategy investigated in this study.

4.2.5.1 Microstructural Modification Strategies: Porosity (P)

For all porosity-based strategies, the catalyst layer (CCL) porosity was constrained to a practical range of 0.35-0.65 [167], [168], [169], and all generated geometries were maintained above the percolation threshold.

Three porosity modification approaches were considered:

- Uniform porosity variation (P-U): The porosity was varied uniformly across the entire CCL thickness in increments of 0.05.

- Spatially varied porosity (P-V): A linear porosity gradient was imposed along the through-plane (x) direction while maintaining a constant average porosity of 0.45. Both increasing and decreasing gradients from the PEM interface to the GDL interface were examined.
- Constriction strategies (P-C): Localized regions of reduced porosity were introduced at different through-plane locations within the CCL. Specifically, constrictions were placed at the PEM interface (P-CPEM), the middle of the CCL (P-Cmid), and the GDL interface (P-CGDL). The constricted region had a porosity of 0.65 and a width corresponding to 20% of the CCL thickness, while the remaining region had a porosity of 0.40, preserving an overall average porosity of 0.45.

To ensure consistency across all microstructural variations, the blobiness parameter used during geometry generation was adjusted as needed to maintain comparable agglomerate sizes across different porosity cases. Any resulting variation in agglomerate size was limited to ±2 nm relative to the base case.

4.2.5.2 Microstructural Modification Strategies: Agglomerate Size (A)

Agglomerate size distributions with different mean diameters were generated to examine their impact on performance and degradation. Spatial variation in agglomerate size was not considered, as such distributions cannot be reliably generated within the available domain size. Reported agglomerate sizes in the literature span a wide range, from approximately 100 nm to micrometers [164]. In this study, the mean agglomerate diameter was restricted to a narrower yet still practical range of 120-225 nm, varied in increments of approximately 15 nm (with deviations limited to ±2 nm). Agglomerate sizes that are too small introduce discretization artifacts in the pore-network representation while larger agglomerates are not adequately representative of the CCL within the domain size. The selected range, therefore, balances numerical accuracy and geometric fidelity.

4.2.5.3 Platinum Placement (L)

The effects of spatial platinum placement were investigated by varying the local platinum loading while maintaining a constant overall loading of 0.1 mg cm^{-2}. Spatial variations were imposed using a linear distribution along the through-plane direction. Two platinum placement strategies were considered:

- Size-varied placement (L-SV): Platinum particle sizes were varied spatially based on the loading while maintaining the particle number density.
- Number-varied placement (L-SN): The number density of platinum per ionomer pore was varied spatially based on the loading while maintaining the particle size.

Note that for spatially varying cases, strategies are labeled according to the platinum loading specified at the PEM interface (e.g., L-SV0.05 indicates a platinum loading of 0.05 mg cm^{-2} at the PEM-CCL interface, with the spatial variation implemented through changes in particle size).

Table 4.2 provides an overview of the base case and all simulation cases, detailing the porosity profiles, agglomerate size information, and platinum loading profiles considered in this study.

Table 4.2: Summary of simulation cases analyzed in this study with varying porosity profiles, mean agglomerate sizes, and spatial platinum loading distributions

Simulation	Porosity Profile $\boldsymbol{\varepsilon(x)}$	Agglomerate Size	Pt Loading Profile $\boldsymbol{l(x)}$ [mg cm^{-2}]
Base Case	$\varepsilon(x) = 0.45$ Uniform	$d_{agg}^{mean} = 182$ nm $\beta = 0.60$	$l(x) = 0.1$ Uniform size and amount
P-U0.55	$\varepsilon(x) = 0.55$ Uniform	$d_{agg}^{mean} = 182$ nm $\beta = 0.50$	$l(x) = 0.1$ Uniform size and amount
P-U0.50	$\varepsilon(x) = 0.50$ Uniform	$d_{agg}^{mean} = 182$ nm $\beta = 0.55$	$l(x) = 0.1$ Uniform size and amount
P-U0.40	$\varepsilon(x) = 0.40$ Uniform	$d_{agg}^{mean} = 181$ nm $\beta = 0.70$	$l(x) = 0.1$ Uniform size and amount
P-U0.35	$\varepsilon(x) = 0.35$ Uniform	$d_{agg}^{mean} = 181$ nm $\beta = 0.80$	$l(x) = 0.1$ Uniform size and amount
P-V0.55	$\varepsilon(x) = -0.2x + 0.55$ Spatially varied	$d_{agg}^{mean} = 183$ nm $\beta = 0.60$	$l(x) = 0.1$ Uniform size and amount
P-V0.50	$\varepsilon(x) = -0.1x + 0.50$ Spatially varied	$d_{agg}^{mean} = 183$ nm $\beta = 0.60$	$l(x) = 0.1$ Uniform size and amount

P-V0.40	$\varepsilon(x) = 0.1x + 0.40$ Spatially varied	$d_{agg}^{mean} = 181$ nm $\beta = 0.60$	$l(x) = 0.1$ Uniform size and amount
P-V0.35	$\varepsilon(x) = 0.2x + 0.35$ Spatially varied	$d_{agg}^{mean} = 181$ nm $\beta = 0.60$	$l(x) = 0.1$ Uniform size and amount
P-CPEM	$\varepsilon(x) = \begin{cases} 0.40, & 1 \geq x \geq 0.2 \\ 0.65, & 0.2 > x \geq 0 \end{cases}$ Constriction (PEM-side)	$d_{agg}^{mean} = 181$ nm $\beta = 0.65$	$l(x) = 0.1$ Uniform size and amount
P-Cmid	$\varepsilon(x) = \begin{cases} 0.40, & 1.0 \geq x \geq 0.6 \\ 0.65, & 0.6 > x \geq 0.4 \\ 0.40, & 0.4 > x \geq 0 \end{cases}$ Constriction (middle)	$d_{agg}^{mean} = 182$ nm $\beta = 0.65$	$l(x) = 0.1$ Uniform size and amount
P-CGDL	$\varepsilon(x) = \begin{cases} 0.65, & 1 \geq x \geq 0.8 \\ 0.40, & 0.8 > x \geq 0 \end{cases}$ Constriction (GDL-side)	$d_{agg}^{mean} = 181$ nm $\beta = 0.65$	$l(x) = 0.1$ Uniform size and amount
A-d225	$\varepsilon(x) = 0.45$ Uniform	$d_{agg}^{mean} = 224$ nm $\beta = 0.48$	$l(x) = 0.1$ Uniform size and amount
A-d210	$\varepsilon(x) = 0.45$ Uniform	$d_{agg}^{mean} = 210$ nm $\beta = 0.50$	$l(x) = 0.1$ Uniform size and amount
A-d195	$\varepsilon(x) = 0.45$ Uniform	$d_{agg}^{mean} = 195$ nm $\beta = 0.55$	$l(x) = 0.1$ Uniform size and amount
A-d165	$\varepsilon(x) = 0.45$ Uniform	$d_{agg}^{mean} = 165$ nm $\beta = 0.70$	$l(x) = 0.1$ Uniform size and amount
A-d150	$\varepsilon(x) = 0.45$ Uniform	$d_{agg}^{mean} = 152$ nm $\beta = 0.80$	$l(x) = 0.1$ Uniform size and amount
A-d135	$\varepsilon(x) = 0.45$ Uniform	$d_{agg}^{mean} = 135$ nm $\beta = 0.90$	$l(x) = 0.1$ Uniform size and amount
A-d120	$\varepsilon(x) = 0.45$ Uniform	$d_{agg}^{mean} = 122$ nm $\beta = 1.00$	$l(x) = 0.1$ Uniform size and amount
L-SV0.05	$\varepsilon(x) = 0.45$ Uniform	$d_{agg}^{mean} = 182$ nm $\beta = 0.60$	$l(x) = 0.1x + 0.05$ Spatially varied size, Uniform amount
L-SV0.075	$\varepsilon(x) = 0.45$ Uniform	$d_{agg}^{mean} = 182$ nm $\beta = 0.60$	$l(x) = 0.05x + 0.075$ Spatially varied size, Uniform amount
L-SV0.125	$\varepsilon(x) = 0.45$ Uniform	$d_{agg}^{mean} = 182$ nm $\beta = 0.60$	$l(x) = -0.05x + 0.125$ Spatially varied size, Uniform amount
L-SV0.15	$\varepsilon(x) = 0.45$ Uniform	$d_{agg}^{mean} = 182$ nm $\beta = 0.60$	$l(x) = -0.1x + 0.15$ Spatially varied size, Uniform amount

L-NV0.05	$\varepsilon(x) = 0.45$ Uniform	$d_{agg}^{mean} = 182$ nm $\beta = 0.60$	$l(x) = 0.1x + 0.05$ Spatially varied amount, Uniform size
L-NV0.075	$\varepsilon(x) = 0.45$ Uniform	$d_{agg}^{mean} = 182$ nm $\beta = 0.60$	$l(x) = 0.05x + 0.075$ Spatially varied amount, Uniform size
L-NV0.125	$\varepsilon(x) = 0.45$ Uniform	$d_{agg}^{mean} = 182$ nm $\beta = 0.60$	$l(x) = -0.05x + 0.125$ Spatially varied amount, Uniform size
L-NV0.15	$\varepsilon(x) = 0.45$ Uniform	$d_{agg}^{mean} = 182$ nm $\beta = 0.60$	$l(x) = -0.1x + 0.15$ Spatially varied amount, Uniform size

4.3 Results and Discussion

4.3.1 Microstructural Modification: Porosity Effects

4.3.1.1 Changing the Porosity Uniformly

Figure 4-2a shows the solid fraction (complement of porosity) profiles in the through-plane direction after geometry generation for cases with different, spatially uniform solid fractions. Minor local dips in solid fraction are observed due to the geometry generation step that removes unconnected solid regions. However, the profiles remain approximately uniform overall.

As shown in Figure 4-2b, performance decreases with increasing porosity, with P-U0.55 exhibiting the largest reduction relative to the base case (17%). This decrease is attributed to the increase in tortuosity of the transport pathways for dissolved oxygen and protons to reach the catalyst sites. However, higher porosity also leads to reduced overall surface area loss, as shown in Figure 4-2c. While surface area loss near the membrane is similar across cases, higher-porosity geometries exhibit a greater reduction in surface area loss toward the GDL. This trend is consistent with increased transport resistance due to tortuous pathways. Thus, P-U0.55 also shows the largest reduction in surface area loss (4.7% relative to the base case). A consequence of this degradation mitigation, however, is increased spatial heterogeneity in degradation at higher porosity. We have shown that a more uneven platinum loss profile will negatively impact long-term performance in Appendix C. Overall, these results support the hypothesis that increased porosity reduces total degradation at the cost of performance.

4.3.1.2 Changing the Porosity Spatially

For spatially varying porosity, Figure 4-2d shows the varying linear solid fraction profiles of each simulation in the through-plane direction, where the overall porosity is maintained at 0.45. Figure 4-2e and Figure 4-2f shows the corresponding effects on performance and degradation, respectively.

Cases with higher porosity (lower solid fraction) near the membrane with the porosity decreasing toward the GDL are the most effective at reducing surface area loss. Among these, P-V0.55 achieves the largest reduction in ECSA loss (12%). This is because increased porosity near the membrane introduces more tortuous transport pathways for platinum ions in the membrane interface, the region where platinum loss is most pronounced. Similar to the uniformly varied porosity cases, the configurations with the greatest degradation reduction also exhibit the largest performance decrease. P-V0.55 shows a 22% reduction in performance. This behavior can be attributed to the increase in ohmic losses caused by constricted proton transport pathways from the membrane interface into the catalyst layer. Similar to the uniform porosity modifications, increased heterogeneity is also another undesirable side effect of increased degradation reduction.

4.3.1.3 Introducing Geometric Constrictions

Figure 4-2g shows catalyst layer geometries with localized constrictions represented by reduced solid fraction at the membrane interface, mid-CCL, and GDL interface, all plotted alongside the base case. All configurations maintain the same overall porosity of 0.45.

The degradation profiles shown in Figure 4-2i reveal that the PEM-interface constriction results in the largest reduction in surface area loss, with an ECSA loss reduction of 16.5%, the highest among all porosity-based strategies. This result indicates that geometric constrictions can be highly effective at mitigating platinum loss. However, this configuration also exhibits the most severe performance degradation (39%), as shown in Figure 4-2h. It also results in the highest degradation heterogeneity due to the sharp drop-off near the membrane. In contrast, the mid-CCL constriction case shows a more gradual surface area loss profile until the constriction location, followed by a secondary sharp decrease. Beyond this point, the surface area loss remains relatively uniform toward the GDL. Importantly, Figure 4-2h shows that performance is only mildly affected for this configuration (3.3% loss).

Overall, the porosity-based strategies that are effective in reducing surface area loss do so by increasing platinum ion transport resistance in the ionomer, but they also inherently result in worse performance as the same mechanisms affect proton and dissolved oxygen transport. Additionally, surface area loss in the membrane interface ($x = 0$) appears to be nearly constant across all cases, which implies that porosity-based strategies do not reduce surface area loss in the membrane interface and that reductions in total degradation necessarily increase spatial heterogeneity. This suggests that local electrochemical conditions dominate over structural modifications in the region near the membrane and highlights the need to couple porosity-based approaches with additional mitigation strategies to address both performance loss and degradation heterogeneity.

Among the cases showing ECSA loss reduction are those with uniformly increased porosity (P-U0.50, P-U0.55), spatially graded porosity with higher porosity near the membrane (P-V0.50, P-V0.55), and geometries with constrictions at the membrane interface (P-CPEM) and mid-CCL (P-Cmid). All of these cases exhibit performance losses relative to the base case, revealing an inverse relationship between performance and degradation mitigation.

Notably, P-Cmid shows the smallest performance reduction (3.26%) while still achieving a degradation reduction of 2.6%, exceeding that of P-V0.50 (1.1%) and P-U0.05 (0.61%), which both had higher performance reductions (6.4% and 5.3%, respectively). As a result, P-Cmid is selected for combination with other mitigation strategies in the subsequent case study.

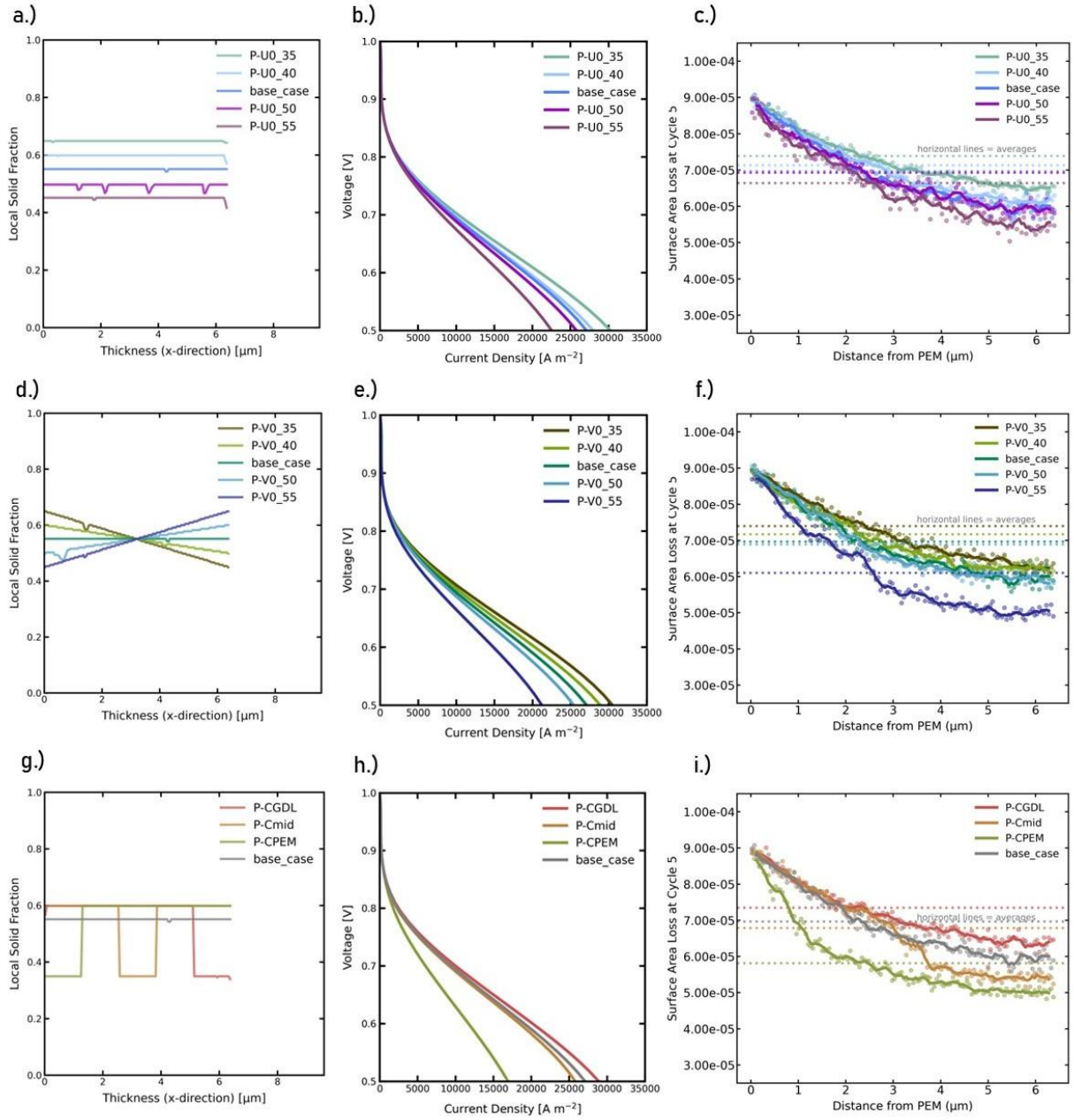


Figure 4-2: Left panel: slice-averaged porosity profiles in the through-plane direction for the a.) uniformly-varied porosity, d.) spatially-varied porosity, and g.) applied constrictions. Centre panel: polarization curves representing the initial performance for the b.) uniformly-varied porosity, e.) spatially-varied porosity, and h.) porosity constrictions. Right panel: slice-averaged surface area loss in the through-plane direction and overall surface area loss (dotted horizontal lines) for the c.) uniformly-varied porosity, f.) spatially-varied porosity, and i.) porosity constrictions. The base case is plotted in all plots for comparison.

4.3.2 Microstructural Modification: Agglomerate Size Effects

Figure 4-3a shows the agglomerate size distributions obtained from the simulations, plotted together with fitted Gaussian curves and with the corresponding mean agglomerate diameters displayed. As the mean agglomerate size decreases, the variance of the distribution also decreases which reflects the reduced range of possible agglomerate sizes in the cases with smaller agglomerates.

Figure 4-3b and Figure 4-3c show the corresponding polarization curves and degradation profiles, respectively. The degradation profiles are nearly identical across all agglomerate sizes, which shows that both the total surface area loss and the spatial homogeneity of degradation are not affected by agglomerate size within the range studied. In contrast, a clear dependence on agglomerate size is observed in the performance. Larger agglomerates lead to reduced performance, with A-d225 exhibiting a 6% decrease relative to the base case, while smaller agglomerates improve performance, with A-d120 showing performance increases of around 8%. This behavior supports the hypothesis that reducing agglomerate size increases the interfacial surface area between the gas phase and ionomer and therefore enhances access to platinum sites and lowers mass transport resistance for dissolved oxygen within the catalyst layer [170]. Importantly, this trend suggests that agglomerate size reduction can be effectively combined with porosity-based strategies, which reduce degradation but worsens performance. By improving performance without significantly affecting degradation, smaller agglomerates provide a means to offset the performance losses associated with porosity-driven mitigation approaches. Based on these results, A-d120, being the smallest agglomerate size in the range, is selected as the optimal agglomerate size strategy.

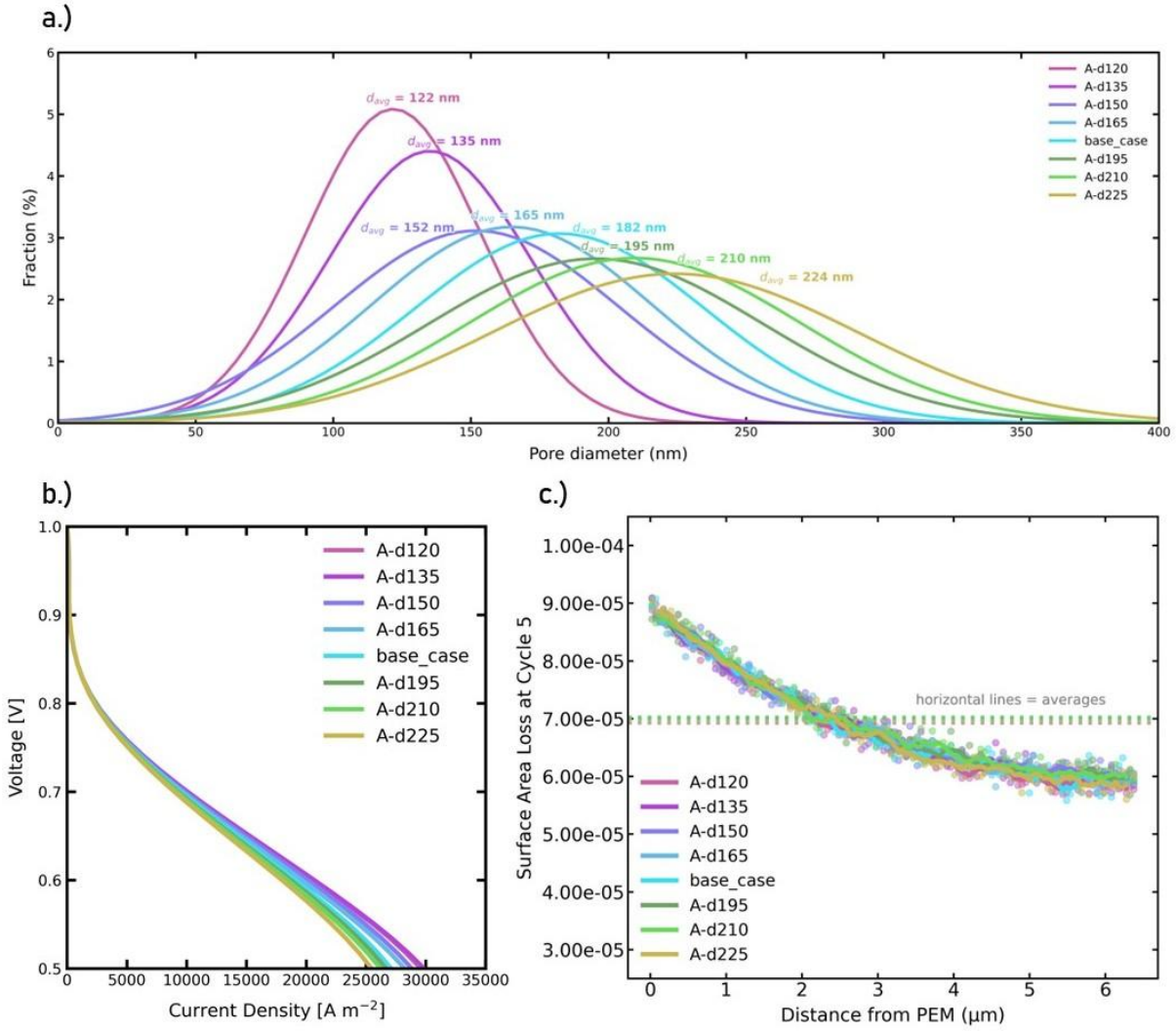


Figure 4-3: a.) Fitted Gaussian distribution of different geometries with varied agglomerate sizes, along with the average agglomerate diameter. b.) Polarization curves representing the initial performances. c.) Slice-averaged surface area loss in the through-plane direction and overall surface area loss (dotted horizontal lines). The base case is plotted for comparison.

4.3.3 Platinum Placement Effects

4.3.3.1 Size-Varied Spatial Platinum Loading

Figure 4-4a and Figure 4-4b show the platinum particle number density and size profiles for the size-varied spatial loading cases. The number density of platinum particles per pore remains uniform, while particle size varies spatially according to the imposed loading profile. Note that although the platinum

loading varies linearly, the resulting particle size distribution exhibits a nonlinear profile due to the cubic relationship between platinum loading and particle radius ($l_{Pt} \propto r_{Pt}^3$).

Figure 4-4c and Figure 4-4d show the corresponding polarization curves and surface area loss profiles, representing performance and degradation, respectively. Differences in the performance among these cases are negligible, with only minor increases in ohmic losses observed when smaller platinum particles are placed near the membrane due to reduced local catalyst availability and increased proton transport distances, although the imposed loading gradients are not large enough to cause huge differences in performance. In contrast, the degradation profiles exhibit pronounced differences in shape. In L-SV0.05, where the smallest platinum particles are located near the membrane, surface area loss is stronger in this region as smaller particles are more vulnerable to dissolution and platinum mass loss. Conversely, L-SV0.15 shows increased degradation at the GDL interface, resulting in an inverted degradation profile. All size-varied cases exhibit worse overall degradation reduction compared to the base case, particularly for the extreme loading gradients. Under fixed total platinum loading, size-varied spatial profiles inevitably create regions with particles smaller than the base case average, which are more susceptible to dissolution and therefore increase total degradation [59]. Despite this, the strong sensitivity of the degradation profile shape on the size-varied loading profile demonstrates that spatial platinum size distributions can be used to actively control degradation homogeneity. Among all cases, L-SV0.125 results in the most uniform degradation profile, improving degradation homogeneity by 43% relative to the base case, although heterogeneity is not completely eliminated. This supports the hypothesis that placing larger platinum particles near the membrane can counteract the inherently higher degradation rates in this region.

Similar strategies involving increased platinum particle size near the membrane have been reported in continuum modeling studies by Baricci et al. [113] and observed experimentally by Yu et al. [151], further supporting this strategy. These results suggest that an optimized, potentially nonlinear spatial platinum loading with larger particles near the PEM and smaller particles toward the GDL could produce a more uniform degradation profile. However, this strategy does result in an increase in total degradation (1.7% for L-SV0.125) and therefore needs to be combined with complementary mitigation approaches. Importantly, this strategy is the first approach considered in this work that directly targets degradation homogeneity.

4.3.3.2 Number-Varied Spatial Platinum Loading

Figure 4-4e and Figure 4-4f show the spatial platinum profiles for the number-varied loading cases, in which the platinum particle size is held constant while the number density of particles per ionomer pore is

varied to impose a linear loading gradient. As expected, regions with higher platinum loading correspond to increased particle number density, while maintaining uniform particle sizes across the domain. Figure 4-4g presents the corresponding polarization curves, which show that performance is not significantly affected by the imposed loading gradients, with increases in ohmic losses observed for cases with reduced platinum loading near the membrane. Again, these loading gradients are not large enough to result in huge performance losses. In contrast, the degradation behavior exhibits some dependence on the platinum placement strategy. As shown in Figure 4-4h, configurations with higher platinum loading near the membrane exhibit increased surface area loss, with L-NV0.15 showing the largest overall ECSA loss (5.5% relative increase compared to the base case). This trend arises because regions with higher platinum number density have more initial surface area, leading to larger absolute surface area loss. The configurations that improve degradation homogeneity also exhibit higher total ECSA loss.

This behavior appears to contradict our hypothesis that increased platinum loading near the membrane improves durability, as previously reported by Yu et al. [152] and modeled by Baricci et al. [113]. However, when the degradation timescale is considered, the observed trends are consistent with these prior studies. Yu et al. [152] showed that graded catalyst layers with higher platinum loading near the membrane exhibit greater ECSA loss during the first several thousand cycles, with a crossover occurring at approximately 10,000 cycles. Beyond this point, the graded layer configuration degrades more slowly and shows improved long-term ECSA retention. This transition was attributed to enhanced platinum homogeneity and particle growth near the membrane, which stabilizes degradation at later stages. Our analysis of homogeneity effects (Appendix C) supports this interpretation. We believe that beyond mid-stage degradation, longer-term mechanisms such as particle agglomeration and coalescence, detachment, and complete dissolution of platinum sites become dominant, leading to more severe mass transport losses. Under these conditions, heterogeneous configurations with regions of inaccessible platinum sites are more susceptible to performance degradation. For this reason, degradation homogeneity is introduced as a complementary metric to total ECSA loss, serving as a proxy for assessing long-term durability beyond the simulated cycles. Total surface area loss reflects the severity of early-stage degradation, whereas homogeneity captures how degradation is distributed spatially and thus provides insight into longer-term stability. Thus, these two degradation metrics should be evaluated jointly rather than in isolation to capture both early- and late-stage degradation behavior.

Guided by this framework, number-varied platinum loading strategies were not selected for the combined case study. Although these configurations improve degradation homogeneity, they do so at the expense of increased early-stage degradation. Instead, strategies that simultaneously improve performance, reduce

total degradation, and enhance spatial uniformity were prioritized, as explored in the following case study.

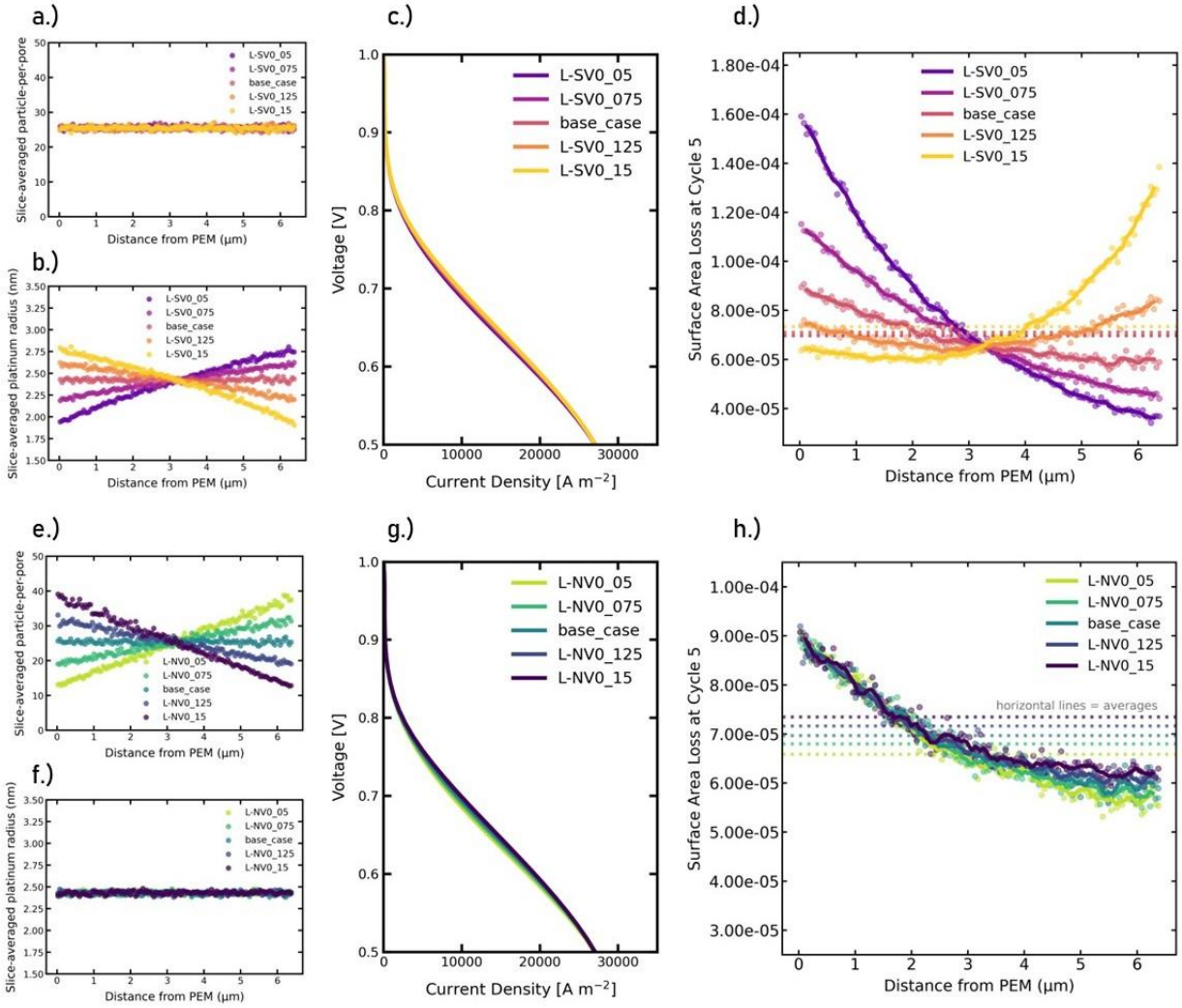


Figure 4-4: Left panel: slice-averaged number density of particle per pore for the a.) size-varied loading and e.) number-varied loading; with the slice-averaged platinum radius for the b.) size-varied loading and f.) number-varied loading. Centre panel: Polarization curves representing the initial performances for c.) size-varied loading and g.) number-varied loading. Right panel: Slice-averaged surface area loss in the through-plane direction and overall surface area loss (dotted horizontal lines) for the d.) size-varied loading and h.) number-varied loading

4.3.4 Case Study: Combined Strategies

We selected a combined configuration consisting of mid-layer porosity constriction (P-Cmid), the smallest agglomerate size in our range (A-d120), and a size-varied platinum loading profile that yields the highest degree of homogeneity (L-SV0.125). This configuration was chosen with the aim of achieving balanced improvements across all selected metrics. To account for the randomness and variability inherent in the pore network generation, five simulations with identical settings were conducted to better demonstrate trends.

Figure 4-5a and Figure 4-5b present the initial polarization curves, representing performance, and the corresponding degradation profiles, representing durability, respectively, in comparison with the base case. All five simulations exhibit improved initial performance relative to the base case, with performance increases of approximately 10-13%. This enhancement is primarily attributed to the reduction in agglomerate size, which improves reactant accessibility and effective catalyst utilization. In addition, all cases show reduced overall degradation, with a 1.6-3.7% decrease in total ECSA loss, indicating improved stability during early-stage degradation.

Importantly, degradation homogeneity is also significantly improved, with a 34-49% reduction in the coefficient of variation (CoV) of ECSA loss compared to the base case. This improvement suggests that the combined strategy not only stabilizes early-stage degradation but also mitigates localized degradation, which is critical for long-term durability. However, the degradation profiles exhibit a non-monotonic spatial trend, characterized by a pronounced decrease in ECSA loss in the mid-region of the cathode catalyst layer, followed by an increase toward the gas diffusion layer (GDL). This behavior indicates that a simple linear platinum loading gradient may be insufficient to achieve spatially uniform degradation. These observations point to the need for more sophisticated platinum loading profiles. Nonlinear profiles such as exponential or step-wise distributions may offer improved control over spatial ECSA loss and further enhance degradation uniformity across the CCL.

Figure 4-5c and Figure 4-5d provide a graphical representation of the trade-offs between performance and durability based on the values from Table 4.3. Figure 4-5c plots the increase in current density against the reduction in total ECSA loss, while Figure 4-5d relates overall degradation reduction to improvements in degradation homogeneity (CoV reduction), with the base case located at the origin. These plots show that the combined-strategy cases are the only configurations that consistently occupy the positive quadrants in both metrics. This indicates that simultaneous improvements in performance, overall durability, and degradation uniformity are achievable only through the integration of multiple design strategies. In the case-study configuration, the mid-layer porosity constriction alters local transport pathways and partially

isolates degradation, reduced agglomerate size enhances reactant accessibility and catalytic utilization, and size-varied platinum placement redistributes degradation more uniformly across the catalyst layer thickness.

These results suggest that a spatially graded catalyst layer design may provide a pathway to simultaneously balance performance, total degradation, and degradation homogeneity. The combined strategies essentially partition the catalyst layer into regions with distinct functional roles. A physically consistent interpretation of the results is that a mid-layer constriction, coupled with larger platinum particles near the membrane and smaller particles toward the GDL, can balance local degradation susceptibility with catalytic accessibility. Larger particles in the PEM side reduce rapid surface area loss, while smaller particles in the GDL side maintain high utilization where degradation is isolated from the constriction. Reduced agglomerate size further improves oxygen transport and reaction accessibility, helping offset performance losses introduced by the structural modifications. Together, these features indicate that optimal durability may emerge from tailoring local structure to match the dominant local transport and electrochemical conditions. This motivates further discussion of future work in the Conclusions.

While these analyses represent a limited set of cases, the results demonstrate the potential of combined structural and compositional modifications to the CCL. With careful engineering of porosity, agglomerate morphology, and platinum loading distributions, it may be possible to mitigate catalyst degradation and address durability limitations in PEM fuel cells. Spatially resolved fabrication of catalyst layer structure and platinum distribution can be achieved [171], for instance, using existing advanced printing techniques such as inkjet printing [172], spray coating [173], slot-die coating [174], screen printing [175], and roll coating [176]. These enable experimental implementation of the spatial design strategies investigated in this work.

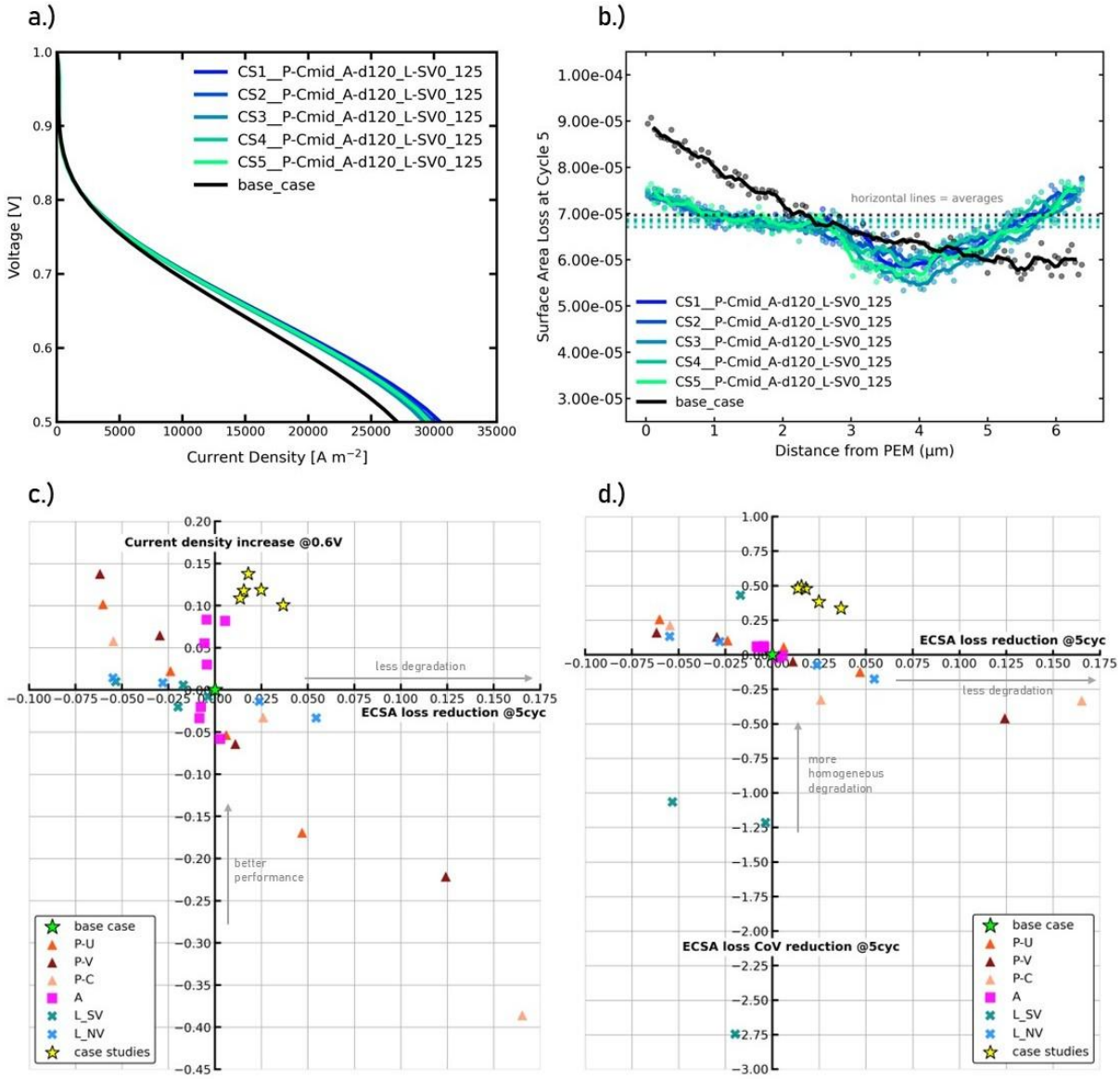


Figure 4-5 a.) Initial performances for the case study simulations compared to the base case. b.) Slice-averaged surface area loss in the through-plane direction and overall surface area loss (dotted horizontal lines) for the case study simulations compared to the base case. c.) Current density increase plotted vs. ECSA loss reduction for all simulations run. d.) ECSA loss CoV reduction plotted vs. ECSA loss reduction for all simulations run

Table 4.3: Table of simulation results

Simulation	Current density @ 0.6V	ECSA loss @ 5cyc	ECSA loss CoV @ 5cyc	Current density increase @ 0.6 V	ECSA loss reduction @ 5cyc	ECSA loss CoV reduction @ 5cyc
Base Case	1.91E+04	6.97E-05	1.30E-01	0.00	0.00	0.00
P-U0.55	1.59E+04	6.64E-05	1.46E-01	-0.1693	0.0469	-0.1246
P-U0.50	1.81E+04	6.93E-05	1.23E-01	-0.0534	0.0061	0.0557
P-U0.40	1.95E+04	7.13E-05	1.17E-01	0.0224	-0.0239	0.1034
P-U0.35	2.10E+04	7.39E-05	9.66E-02	0.1017	-0.0602	0.2574
P-V0.55	1.49E+04	6.10E-05	1.90E-01	-0.2214	0.1242	-0.4599
P-V0.50	1.79E+04	6.89E-05	1.36E-01	-0.0641	0.0110	-0.0482
P-V0.40	2.03E+04	7.17E-05	1.13E-01	0.0647	-0.0296	0.1300
P-V0.35	2.17E+04	7.40E-05	1.09E-01	0.1377	-0.0618	0.1612
P-CPEM	1.17E+04	5.82E-05	1.73E-01	-0.3859	0.1653	-0.3320
P-Cmid	1.85E+04	6.79E-05	1.72E-01	-0.0326	0.0260	-0.3247
P-CGDL	2.02E+04	7.35E-05	1.02E-01	0.0579	-0.0546	0.2132
A-d225	1.80E+04	6.95E-05	1.33E-01	-0.0581	0.0028	-0.0209
A-d210	1.84E+04	7.03E-05	1.22E-01	-0.0334	-0.0083	0.0601
A-d195	1.87E+04	7.02E-05	1.24E-01	-0.0201	-0.0076	0.0506
A-d165	1.97E+04	7.00E-05	1.23E-01	0.0301	-0.0043	0.0516
A-d150	2.01E+04	7.01E-05	1.23E-01	0.0553	-0.0056	0.0524
A-d135	2.07E+04	7.00E-05	1.22E-01	0.0834	-0.0045	0.0626
A-d120	2.06E+04	6.93E-05	1.31E-01	0.0818	0.0055	-0.0074
L-SV0.05	1.87E+04	7.11E-05	4.87E-01	-0.0202	-0.0198	-2.7460
L-SV0.075	1.89E+04	6.99E-05	2.88E-01	-0.0081	-0.0036	-1.2147
L-SV0.125	1.92E+04	7.09E-05	7.40E-02	0.0057	-0.0170	0.4310
L-SV0.15	1.93E+04	7.34E-05	2.69E-01	0.0098	-0.0533	-1.0659
L-NV0.05	1.84E+04	6.59E-05	1.53E-01	-0.0333	0.0545	-0.1757
L-NV0.075	1.88E+04	6.80E-05	1.40E-01	-0.0135	0.0239	-0.0746
L-NV0.125	1.92E+04	7.16E-05	1.18E-01	0.0084	-0.0280	0.0945
L-NV0.15	1.94E+04	7.35E-05	1.13E-01	0.0142	-0.0548	0.1326
CS1	2.17E+04	6.84E-05	6.80E-02	0.1378	0.0179	0.4771
CS2	2.13E+04	6.86E-05	6.58E-02	0.1176	0.0155	0.4944
CS3	2.10E+04	6.71E-05	8.63E-02	0.1007	0.0367	0.3366
CS4	2.12E+04	6.87E-05	6.76E-02	0.1088	0.0136	0.4807
CS5	2.13E+04	6.80E-05	8.03E-02	0.1186	0.0248	0.3828

4.3.5 Limitations of the Analyses

While the results presented in this work show promising trends and provide a useful first assessment of potential catalyst layer modification strategies, it is important to acknowledge the limitations of the present analyses. This study is intended as an exploratory modeling work to help prioritize and inform future experimental investigations rather than to give definitive predictions of real-world durability.

A primary limitation is the lack of long-term temporal resolution in the modeled degradation behavior. Although the simulations capture early-stage degradation trends, the simplified degradation framework cannot directly extrapolate long-term performance. As a result, certain degradation mechanisms that become dominant at extended cycling durations may not be fully represented. To partially address this limitation, as discussed, degradation homogeneity was introduced as an additional metric to infer long-term stability. While this approach provides insight into later-stage degradation, we acknowledge that it cannot fully substitute for explicit long-term modeling or experimental validation, and some relevant mechanisms may remain unaccounted for.

Several simplifying assumptions were also made in the model formulation. As discussed in the preceding work, liquid water accumulation was neglected since the accelerated stress test conditions considered here involve relatively low current densities and high operating temperature. However, at higher current densities, structural modifications to the cathode catalyst layer (CCL) could potentially influence water transport and flooding behavior, and moreover, the presence of water may exacerbate Pt ion transport. Previous studies suggest that the gas diffusion layer plays a more dominant role in liquid water management [23], but interactions between CCL structure and two-phase transport may require further investigation under different operating conditions.

In addition, although the present model represents an improvement over our earlier work by explicitly resolving three-dimensional transport phenomena, the computational domain was intentionally limited to enable the large number of simulations required for the analyses. This domain reduction may introduce finite-size effects or artifacts associated with smaller spatial sampling, which should be considered when interpreting the results.

Finally, we emphasize that this study is fundamentally a modeling-based investigation aimed at generating physical insight and guiding experimental design. The conclusions drawn here do not claim direct transferability to practical fuel cell systems without experimental validation. Nevertheless, the ability to investigate degradation behavior within a fully three-dimensional pore-scale framework provides valuable insight into the coupled effects of microstructure and catalyst layer configuration. Given the extreme thinness of the CCL and the experimental challenges associated with probing its

internal degradation behavior, we believe that this work represents a meaningful step toward improving the mechanistic understanding of durability in PEM fuel cells.

4.4 Conclusions and Recommendations

Utilizing the previously introduced transient pore-scale model of platinum degradation, this study extended the catalyst layer geometry to three dimensions while retaining the same degradation framework to investigate pore-scale mitigation strategies for platinum degradation. Strategies targeting porosity, agglomerate size, and spatial platinum distribution were evaluated using three complementary metrics: performance, total degradation, and degradation homogeneity. The main findings are summarized as follows:

- Porosity: Modifying porosity effectively reduces total surface area loss but introduces trade-offs with performance and degradation uniformity. Increasing overall porosity or introducing higher porosity near the membrane enhances platinum ion transport resistance and reduces loss to the membrane, but also increases transport limitations for ORR reacting species. Among the tested configurations, a mid-CCL constriction (P-Cmid) provided the most balanced improvement by reducing degradation while minimizing performance loss.
- Agglomerate size: Agglomerate size had negligible influence on total degradation and homogeneity, but strongly affected performance. Smaller agglomerates improved catalytic accessibility and reduced mass transport resistance, leading to higher current density. This suggests that careful engineering of the ionomer agglomerate may serve as an effective strategy to offset performance losses introduced by durability-focused modifications.
- Platinum placement: Varying platinum distribution had a limited impact on performance but significantly altered degradation profiles. Size-varied platinum loading enabled control over degradation homogeneity by redistributing where surface area loss occurs across the catalyst layer thickness. Number-varied loading demonstrated that reducing platinum loading near the membrane decreases surface area loss, while differences between total degradation and spatial homogeneity reflect distinct stages of catalyst aging.

A combined case study integrating a mid-layer porosity constriction, reduced agglomerate size, and size-varied platinum placement demonstrated simultaneous improvements across all evaluated metrics. The combined configuration improved performance, reduced overall degradation, and enhanced degradation uniformity compared with the base case, highlighting the importance of multi-parameter design strategies over isolated modifications.

Several limitations of the analyses were also acknowledged. The simulations focus on early-stage degradation behaviour and did not explicitly resolve long-term mechanisms such as coalescence or structural evolution over thousands of cycles. Simplifications in transport phenomena and domain size were also required to enable systematic parametric exploration. Thus, the results should be interpreted as comparative insights into relative trends. Nevertheless, this work provides a useful exploratory framework for evaluating design strategies and combined approaches that remain largely unexplored in the literature, and could help guide future experimental investigations.

Experimental studies may draw useful insights from this work by treating the proposed configurations as physically motivated hypotheses. The trends observed here suggest that a catalyst layer design combining a mid-CCL porosity constriction or concave porosity profile, larger platinum particles with higher loading near the membrane and smaller particles toward the GDL, and reduced agglomerate sizes may help balance the performance-degradation trade-off. Conceptually, such a design partitions the catalyst layer into regions with distinct functional roles, where membrane-side coarser particles may limit accelerated surface area loss while smaller particles farther from the membrane enhance utilization under less severe degradation conditions. Although not intended as a definitive or optimal configuration, this work provides a framework for targeted experimental exploration. The results further motivate the development of advanced coating and printing techniques capable of fabricating spatially graded catalyst layers with tailored platinum and microstructural property distributions, which could implement the design principles identified here into realistic CCL designs.

Beyond experimental validation, this work also highlights opportunities for future modeling studies. Pore-scale and multiscale approaches, as well as physics-informed data-driven methods, could expand the exploration of unconventional and unexplored mitigation strategies. While many existing models focus primarily on predicting performance or degradation trends, leveraging these tools to actively guide material and structural design may accelerate the development of durable fuel cells, particularly as heavy-duty applications move closer to commercialization.

Chapter 5
Overall Conclusions and Future Work

5.1 Summary and Outcomes

Overall, this thesis contributes to the understanding and modeling of platinum degradation in the cathode catalyst layer (CCL) through three major outcomes: (i) thorough categorization of existing platinum degradation models in literature [157], (ii) development of the first transient pore network model of platinum degradation [159], and (iii) application of the model to investigate the role of microstructural and spatial variables on degradation behavior [177].

5.1.1 Categorization and Evaluation of Platinum Degradation Models

Chapter 2 presented a comprehensive review of platinum degradation models reported in the literature. Existing approaches range from simplified zero-dimensional lumped models to three-dimensional continuum models, multiscale models, and models integrated into full fuel cell system analysis.

Through this review, three dominant modeling frameworks were identified: the Darling-Meyers model, the Holby-Morgan model, and the Rinaldo-Stumper-Eikerling model. These frameworks have shaped much of the current understanding of platinum dissolution and oxidation. To the best of the author's knowledge, this work represents the first structured categorization of platinum degradation models into families of models. This classification provides a foundation for systematic comparison, parametric evaluation, and the potential standardization of different degradation modeling approaches. The review further identified some key gaps in the literature, such as the absence of pore-scale models that are capable of resolving platinum degradation within realistic catalyst layer microstructures.

5.1.2 The First Pore Network Model of Platinum Degradation

Addressing the identified modeling gap, Chapter 3 introduced the first transient pore-scale model of platinum degradation using pore network modeling. As a proof-of-concept work, the analysis was conducted on a two-dimensional pore network representing the cathode catalyst layer.

The geometry generation methodology, and modeling assumptions and simplifications were detailed. The developed model couples a performance solver, which models the oxygen reduction reaction, with a degradation solver that captures platinum dissolution, oxidation, and platinum ion transport toward the membrane. The model was validated using transport and structural data available in the literature, then calibrated against available experimental degradation data. It should be emphasized that the model is computationally inefficient and is currently capable of simulating only a limited number of degradation

cycles within a reasonable computational time. Despite this limitation, the model successfully provides a transient pore-scale view of platinum degradation for the first time. The model reproduces experimentally observed degradation trends and offered spatially resolved insights that are inaccessible in continuum-scale models. In particular, the simulations revealed how local pore structure influences platinum ion transport and spatial degradation distribution within the catalyst layer. This work therefore establishes a modeling framework for future microstructurally resolved degradation studies.

5.1.3 Significance of Microstructural and Spatial Variables on Degradation

With a pore-scale modeling framework established, Chapter 4 utilized the model to investigate how structural and spatial parameters influence platinum degradation behavior. A new 3D pore network model was developed using some modified geometry generation techniques and was recalibrated to be consistent with the 2D model. This enabled the systematic variation of geometry generation parameters and catalyst placement strategies to analyze their effect on degradation and performance.

Three primary modifications were explored: variations in the microstructure through the porosity, variations in the microstructure through the agglomerate size, and variations in platinum placement. Increasing porosity or introducing higher porosity near the membrane reduced platinum surface area loss by limiting ion transport toward the membrane but worsened the performance. A mid-layer porosity constriction provided the most balanced outcome, reducing degradation while minimizing performance penalties. Agglomerate size primarily influenced performance and had a negligible effect on degradation, with smaller agglomerates improving the performance. Platinum spatial distribution through particle size variation significantly altered degradation profiles with negligible impact on performance. In particular, larger platinum near the membrane made the degradation more uniform. Importantly, a combined configuration integrating several strategies achieved simultaneous improvements across all evaluated performance and degradation metrics. The results highlight the importance of multi-parameter and spatially engineered design strategies.

Although the analysis remains model-based and subject to the assumptions and simplifications outlined in earlier chapters, the results provide physics-based insight into how microstructural design choices may impact both durability and performance. This work therefore extends the model utility beyond degradation and performance prediction by using the pore-scale model as a tool to explore potential mitigation strategies.

5.2 Outlook and Perspectives

While several findings and contributions were established, there are also important opportunities that remain for further development and application.

5.2.1 Improving Solver Performance

A primary limitation of the current model is that it is still not computationally efficient enough to simulate full fuel cell lifetimes within a reasonable time. The dominant cause is the numerical stiffness arising from the nanoscale dimensions of the pore network coupled with the relatively fast diffusion of platinum ions, which all requires the timesteps to be very small under the explicit RK4 scheme.

Future work should therefore focus on improving the solver efficiency through:

- Implementation of implicit or semi-implicit solvers, which are more suitable for stiff systems and may enable larger stable timesteps. It should be noted, however, that this will increase memory demands and computational complexity, especially for larger pore networks.
- Parallel computation, particularly for the performance solver with transport and reaction calculations at different cell voltages. Leveraging high-performance computing resources such as GPU-based computation could also significantly reduce simulation time.
- More simplified pore network representations, such as building the pore networks on the ionomer agglomerates (an order of magnitude larger than the current pore dimension) with implicitly modeled platinum and carbon phases. While this may introduce additional errors, it could enable larger domain sizes and faster computation, and therefore, longer simulated cycles.

Overall, improving computational efficiency is essential for extending simulations beyond early-stage degradation.

5.2.2 Extending Model Physics and Coupling

5.2.2.1 Modeling Membrane Platinum Precipitation

In the current model, platinum ion transport toward the membrane is modeled as a boundary condition but does not explicitly resolve the precipitation dynamics within the membrane. Previous studies have shown that platinum band formation depends strongly on hydrogen and oxygen crossover rates, and that band location influences the rate of platinum mass loss from the catalyst layer. Future work could model the membrane as a pore network of hydrated polymer and incorporate platinum nucleation, growth, and

plating reactions. This would allow spatial resolution of band formation behaviour and show its effect on the degradation dynamics.

5.2.2.2 Additional Degradation Mechanisms

Only platinum dissolution and oxidation pathways were considered explicitly as they are the dominant degradation mechanisms. However, incorporating additional mechanisms such as platinum coalescence, agglomeration, detachment, and carbon corrosion would provide a more complete analysis of degradation. For example, coalescence could be modeled implicitly through kinetic equations that would reduce the particle number density and increase the particle size.

5.2.2.3 Water Transport and Multiphases

Water transport was neglected based on operating conditions corresponding to high temperature and relatively low current densities. However, incorporating water effects would improve model robustness. This could range from simplified approaches, such as blocking oxygen transport pathways to represent flooding, to fully coupled multiphase pore networks that include gas, ionomer, carbon, platinum, and water phases. Although computationally demanding, these extensions would enhance physical accuracy.

5.2.3 Optimizing CCL Structure for Durability

The pore-scale framework also provides opportunities for systematic catalyst layer optimization. The parametric studies conducted in this thesis could be extended into a multi-objective optimization problem aimed at maximizing performance and minimizing degradation. Additionally, data-driven methods could be integrated with the pore-scale simulations. For example, regression or machine learning approaches could be trained on simulation outputs to identify correlations between the pore structure and catalyst distribution, and degradation metrics. These can expand the exploration of the design space beyond what is computationally possible using direct simulations alone.

5.2.4 Translating Modeling Insights to Experiment

One of the key insights of this work is that durability improvements may require a combination of microstructural and spatial design strategies rather than individual strategies. In particular, graded porosity, spatially varied platinum loading, and agglomerate size reduction were found to be promising strategies. Future experimental studies could evaluate these using advanced coating or printing techniques that are capable of fabricating these catalyst layers. This could ultimately validate of invalidate these findings. Even partial validation or identification of discrepancies from the model would provide valuable insights and feedback for refining model assumptions and improving its predictive capability.

5.2.5 Final Perspective

In recent years, fuel cell research has been, at times, perceived as losing momentum within the electrochemical community, particularly as other clean energy technologies have advanced more rapidly. However, heavy-duty transportation provided an opportunity in which fuel cells can present a compelling advantage. In this context, the question shifts from whether fuel cells remain a relevant research area to which research approach can best achieve the durability targets for heavy-duty vehicles. Progress in the theoretical understanding of degradation mechanisms as well as materials engineering suggests that the field is entering a more mature and design-driven phase. Current developments indicate a shift toward deeper and more targeted innovation. This thesis and its associated works follow this trend by providing deeper insights into the pore-scale behaviour of platinum degradation and suggesting ways of controlling it through microstructural engineering.

The works presented here, together with the ever-increasing number of research breakthroughs and innovations in the field, suggest that fuel cell research continues to evolve with meaningful opportunities for impact in heavy-duty vehicle decarbonization and beyond.

References

[1] Z. Hausfather, “An assessment of current policy scenarios over the 21st century and the reduced plausibility of high-emissions pathways,” *Dialogues on Climate Change*, vol. 2, no. 1, pp. 26–32, Apr. 2025, doi: 10.1177/29768659241304854.

[2] S. Adak, N. Mandal, A. Mukhopadhyay, P. P. Maity, and S. Sen, “Current State and Prediction of Future Global Climate Change and Variability in Terms of CO2 Levels and Temperature,” in *Enhancing Resilience of Dryland Agriculture Under Changing Climate: Interdisciplinary and Convergence Approaches*, A. Naorem and D. Machiwal, Eds., Singapore: Springer Nature, 2023, pp. 15–43. doi: 10.1007/978-981-19-9159-2_2.

[3] Intergovernmental Panel on Climate Change, “Sixth Assessment Report.” 2021. Accessed: Dec. 24, 2025. [Online]. Available: https://www.ipcc.ch/assessment-report/ar6/

[4] W. Huang, H. Xu, J. Wu, M. Ren, Y. Ke, and J. Qiao, “Toward cleaner air and better health: Current state, challenges, and priorities,” *Science*, vol. 385, no. 6707, pp. 386–390, Jul. 2024, doi: 10.1126/science.adp7832.

[5] M. Brauer *et al.*, “Global burden and strength of evidence for 88 risk factors in 204 countries and 811 subnational locations, 1990–2021: a systematic analysis for the Global Burden of Disease Study 2021,” *The Lancet*, vol. 403, no. 10440, pp. 2162–2203, May 2024, doi: 10.1016/S0140-6736(24)00933-4.

[6] World Resources Institute, “Climate Watch.” Washington, DC, 2024. Accessed: Dec. 25, 2025. [Online]. Available: https://www.climatewatchdata.org/

[7] Environment and Climate Change Canada, “Canada’s Air Pollutant Emissions Inventory Report 2024.” 2024. Accessed: Jan. 25, 2025. [Online]. Available: https://www.canada.ca/en/environment-climate-change/services/air-pollution/publications/emissions-inventory-report-2024/chapter-2-3.html

[8] S. S. Ravi, S. Osipov, and J. W. G. Turner, “Impact of Modern Vehicular Technologies and Emission Regulations on Improving Global Air Quality,” *Atmosphere*, vol. 14, no. 7, p. 1164, Jul. 2023, doi: 10.3390/atmos14071164.

[9] Government of Canada, Statistics Canada, “Vehicle registrations, by type of vehicle and fuel type.” Dec. 01, 2022. Accessed: Dec. 25, 2025. [Online]. Available: https://www150.statcan.gc.ca/t1/tbl1/en/tv.action?pid=2310030801

[10] Environment and Climate Change Canada, “Canada’s official greenhouse gas inventory.” Accessed: Dec. 25, 2025. [Online]. Available: https://www.canada.ca/en/environment-climate-change/services/climate-change/greenhouse-gas-emissions/inventory.html

[11] A. Kusoglu, “Heavy-Duty Transportation in 10 Charts,” *Electrochem. Soc. Interface*, vol. 33, no. 1, p. 26, Mar. 2024, doi: 10.1149/2.F04241IF.

[12] G. Giuliano, M. Dessouky, S. Dexter, J. Fang, S. Hu, and M. Miller, “Heavy-duty trucks: The challenge of getting to zero,” *Transportation Research Part D: Transport and Environment*, vol. 93, p. 102742, Apr. 2021, doi: 10.1016/j.trd.2021.102742.

[13] D. Fan and K. Heminthavong, “Road Transportation: Heavyweight of the Canadian Economy.” Library of Parliament, Parliament of Canada, 2022. Accessed: Dec. 25, 2025. [Online]. Available: https://lop.parl.ca/sites/PublicWebsite/default/en_CA/ResearchPublications/202204E

[14] A. Thiruvengadam, M. Besch, V. Padmanaban, S. Pradhan, and B. Demirgok, “Natural gas vehicles in heavy-duty transportation-A review,” *Energy Policy*, vol. 122, pp. 253–259, Nov. 2018, doi: 10.1016/j.enpol.2018.07.052.

[15] L. A. Graham, G. Rideout, D. Rosenblatt, and J. Hendren, “Greenhouse gas emissions from heavy-duty vehicles,” *Atmospheric Environment*, vol. 42, no. 19, pp. 4665–4681, Jun. 2008, doi: 10.1016/j.atmosenv.2008.01.049.

[16] F. Tong, P. Jaramillo, and I. M. L. Azevedo, “Comparison of Life Cycle Greenhouse Gases from Natural Gas Pathways for Medium and Heavy-Duty Vehicles,” *Environ. Sci. Technol.*, vol. 49, no. 12, pp. 7123–7133, Jun. 2015, doi: 10.1021/es5052759.

[17] C. Cunanan, M.-K. Tran, Y. Lee, S. Kwok, V. Leung, and M. Fowler, “A Review of Heavy-Duty Vehicle Powertrain Technologies: Diesel Engine Vehicles, Battery Electric Vehicles, and Hydrogen Fuel Cell Electric Vehicles,” *Clean Technologies*, vol. 3, no. 2, pp. 474–489, Jun. 2021, doi: 10.3390/cleantechnol3020028.

[18] S. M. Lukic, J. Cao, R. C. Bansal, F. Rodriguez, and A. Emadi, “Energy Storage Systems for Automotive Applications,” *IEEE Transactions on Industrial Electronics*, vol. 55, no. 6, pp. 2258–2267, Jun. 2008, doi: 10.1109/TIE.2008.918390.

[19] V. Malik, S. Srivastava, M. K. Bhatnagar, and M. Vishnoi, “Comparative study and analysis between Solid Oxide Fuel Cells (SOFC) and Proton Exchange Membrane (PEM) fuel cell – A review,” *Materials Today: Proceedings*, vol. 47, pp. 2270–2275, Jan. 2021, doi: 10.1016/j.matpr.2021.04.203.

[20] A. Guo, W. Chen, Q. Li, Z. Liu, and H. Que, “Air flow control based on optimal oxygen excess ratio in fuel cells for vehicles,” *J. Mod. Transport.*, vol. 21, no. 2, pp. 79–85, Jun. 2013, doi: 10.1007/s40534-013-0009-8.

[21] I. Mohamed and N. Jenkins, “Proton exchange membrane (PEM) fuel cell stack configuration using genetic algorithms,” *Journal of Power Sources*, vol. 131, no. 1, pp. 142–146, May 2004, doi: 10.1016/j.jpowsour.2004.01.012.

[22] A. Javed, P. Palafox Gonzalez, and V. Thangadurai, “A Critical Review of Electrolytes for Advanced Low- and High-Temperature Polymer Electrolyte Membrane Fuel Cells,” *ACS Appl. Mater. Interfaces*, vol. 15, no. 25, pp. 29674–29699, Jun. 2023, doi: 10.1021/acsami.3c02635.

[23] Y. Zhang, G. Agravante, T. Kadyk, and M. H. Eikerling, “Modeling water phenomena in the cathode side of polymer electrolyte fuel cells,” *Electrochimica Acta*, vol. 452, p. 142228, Jun. 2023, doi: 10.1016/j.electacta.2023.142228.

[24] M. Sabharwal, J. T. Gostick, and M. Secanell, “Virtual Liquid Water Intrusion in Fuel Cell Gas Diffusion Media,” *J. Electrochem. Soc.*, vol. 165, no. 7, p. F553, May 2018, doi: 10.1149/2.0921807jes.

[25] D. A. Cullen *et al.*, “New roads and challenges for fuel cells in heavy-duty transportation,” *Nat Energy*, vol. 6, no. 5, pp. 462–474, May 2021, doi: 10.1038/s41560-021-00775-z.

[26] F. Zhang *et al.*, “Developing long-durability proton-exchange membrane fuel cells,” *Joule*, vol. 9, no. 3, Mar. 2025, doi: 10.1016/j.joule.2025.101853.

[27] US DOE Hydrogen Program, “M2FCT: Million Mile Fuel Cell Truck Consortium.” 2022. [Online]. Available: https://www.osti.gov/servlets/purl/1863731

[28] V. Patil *et al.*, “Degradation mechanisms in PEM fuel cells: A brief review,” *Materials Today: Proceedings*, Apr. 2023, doi: 10.1016/j.matpr.2023.03.603.

[29] M. Marrony, R. Barrera, S. Quenet, S. Ginocchio, L. Montelatici, and A. Aslanides, “Durability study and lifetime prediction of baseline proton exchange membrane fuel cell under severe operating conditions,” *Journal of Power Sources*, vol. 182, no. 2, pp. 469–475, Aug. 2008, doi: 10.1016/j.jpowsour.2008.02.096.

[30] R. Alink, D. Gerteisen, and M. Oszcipok, “Degradation effects in polymer electrolyte membrane fuel cell stacks by sub-zero operation—An in situ and ex situ analysis,” *Journal of Power Sources*, vol. 182, no. 1, pp. 175–187, Jul. 2008, doi: 10.1016/j.jpowsour.2008.03.074.

[31] D. Qiu, L. Peng, P. Liang, P. Yi, and X. Lai, “Mechanical degradation of proton exchange membrane along the MEA frame in proton exchange membrane fuel cells,” *Energy*, vol. 165, pp. 210–222, Dec. 2018, doi: 10.1016/j.energy.2018.09.136.

[32] J. Zuo, N. Y. Steiner, Z. Li, and D. Hissel, “Degradation root cause analysis of PEM fuel cells using distribution of relaxation times,” *Applied Energy*, vol. 378, p. 124762, Jan. 2025, doi: 10.1016/j.apenergy.2024.124762.

[33] I. Laghryb, M. Malki, N. Yousfi Steiner, C. D. Barrett, and H. El Kadiri, “Catalyst degradation in proton exchange membrane fuel cells: Mechanisms, investigation techniques, and predictive modelling,” *International Journal of Hydrogen Energy*, vol. 145, pp. 496–507, Jul. 2025, doi: 10.1016/j.ijhydene.2025.06.052.

[34] W. He, F. Tang, X. Li, C. Zhang, and P. Ming, “Quantification and evolution on degradation mechanisms of proton exchange membrane fuel cell catalyst layer under dynamic testing

conditions," *International Journal of Hydrogen Energy*, vol. 48, no. 47, pp. 18032–18040, Jun. 2023, doi: 10.1016/j.ijhydene.2023.01.109.

[35] J. C. Meier *et al.*, "Design criteria for stable Pt/C fuel cell catalysts," *Beilstein J. Nanotechnol.*, vol. 5, no. 1, pp. 44–67, Jan. 2014, doi: 10.3762/bjnano.5.5.

[36] S. Zhang, X.-Z. Yuan, J. N. C. Hin, H. Wang, K. A. Friedrich, and M. Schulze, "A review of platinum-based catalyst layer degradation in proton exchange membrane fuel cells," *Journal of Power Sources*, vol. 194, no. 2, pp. 588–600, Dec. 2009, doi: 10.1016/j.jpowsour.2009.06.073.

[37] P. C. Okonkwo *et al.*, "Platinum degradation mechanisms in proton exchange membrane fuel cell (PEMFC) system: A review," *International Journal of Hydrogen Energy*, vol. 46, no. 29, pp. 15850–15865, Apr. 2021, doi: 10.1016/j.ijhydene.2021.02.078.

[38] P. Ren, P. Pei, Y. Li, Z. Wu, D. Chen, and S. Huang, "Degradation mechanisms of proton exchange membrane fuel cell under typical automotive operating conditions," *Progress in Energy and Combustion Science*, vol. 80, p. 100859, Sep. 2020, doi: 10.1016/j.pecs.2020.100859.

[39] J. Wu *et al.*, "A review of PEM fuel cell durability: Degradation mechanisms and mitigation strategies," *Journal of Power Sources*, vol. 184, no. 1, pp. 104–119, Sep. 2008, doi: 10.1016/j.jpowsour.2008.06.006.

[40] N. Yousfi-Steiner, Ph. Moçotéguy, D. Candusso, and D. Hissel, "A review on polymer electrolyte membrane fuel cell catalyst degradation and starvation issues: Causes, consequences and diagnostic for mitigation," *Journal of Power Sources*, vol. 194, no. 1, pp. 130–145, Oct. 2009, doi: 10.1016/j.jpowsour.2009.03.060.

[41] Y. Shao-Horn, W. C. Sheng, S. Chen, P. J. Ferreira, E. F. Holby, and D. Morgan, "Instability of Supported Platinum Nanoparticles in Low-Temperature Fuel Cells," *Top Catal*, vol. 46, no. 3, pp. 285–305, Dec. 2007, doi: 10.1007/s11244-007-9000-0.

[42] J. P. Meyers and R. M. Darling, "Model of Carbon Corrosion in PEM Fuel Cells," *J. Electrochem. Soc.*, vol. 153, no. 8, p. A1432, Jun. 2006, doi: 10.1149/1.2203811.

[43] M. K. Debe, A. K. Schmoeckel, G. D. Vernstrom, and R. Atanasoski, "High voltage stability of nanostructured thin film catalysts for PEM fuel cells," *Journal of Power Sources*, vol. 161, no. 2, pp. 1002–1011, Oct. 2006, doi: 10.1016/j.jpowsour.2006.05.033.

[44] W. Bi, Q. Sun, Y. Deng, and T. F. Fuller, "The effect of humidity and oxygen partial pressure on degradation of Pt/C catalyst in PEM fuel cell," *Electrochimica Acta*, vol. 54, no. 6, pp. 1826–1833, Feb. 2009, doi: 10.1016/j.electacta.2008.10.008.

[45] H.-L. Nguyen, S.-M. Lee, and S. Yu, “A Comprehensive Review of Degradation Prediction Methods for an Automotive Proton Exchange Membrane Fuel Cell,” *Energies*, vol. 16, no. 12, p. 4772, Jan. 2023, doi: 10.3390/en16124772.

[46] K. Foniok, L. Drozdova, L. Prokop, F. Krupa, P. Kedron, and V. Blazek, “Mechanisms and Modelling of Effects on the Degradation Processes of a Proton Exchange Membrane (PEM) Fuel Cell: A Comprehensive Review,” *Energies*, vol. 18, no. 8, p. 2117, Jan. 2025, doi: 10.3390/en18082117.

[47] D. A. J. Rand and R. Woods, “A study of the dissolution of platinum, palladium, rhodium and gold electrodes in 1 *m* sulphuric acid by cyclic voltammetry,” *Journal of Electroanalytical Chemistry and Interfacial Electrochemistry*, vol. 35, no. 1, pp. 209–218, Mar. 1972, doi: 10.1016/S0022-0728(72)80308-5.

[48] K. Kinoshita, J. T. Lundquist, and P. Stonehart, “Potential cycling effects on platinum electrocatalyst surfaces,” *Journal of Electroanalytical Chemistry and Interfacial Electrochemistry*, vol. 48, no. 2, pp. 157–166, Nov. 1973, doi: 10.1016/S0022-0728(73)80257-8.

[49] H. Xu, R. Kunz, and J. M. Fenton, “Investigation of Platinum Oxidation in PEM Fuel Cells at Various Relative Humidities,” *Electrochem. Solid-State Lett.*, vol. 10, no. 1, p. B1, Nov. 2006, doi: 10.1149/1.2372230.

[50] H. Zhang, H. Haas, J. Hu, S. Kundu, M. Davis, and C. Chuy, “The Impact of Potential Cycling on PEMFC Durability,” *J. Electrochem. Soc.*, vol. 160, no. 8, p. F840, May 2013, doi: 10.1149/2.083308jes.

[51] R. M. Darling and J. P. Meyers, “Kinetic Model of Platinum Dissolution in PEMFCs,” *J. Electrochem. Soc.*, vol. 150, no. 11, p. A1523, Sep. 2003, doi: 10.1149/1.1613669.

[52] P. Bindra, S. J. Clouser, and E. Yeager, “Platinum Dissolution in Concentrated Phosphoric Acid,” *J. Electrochem. Soc.*, vol. 126, no. 9, p. 1631, Sep. 1979, doi: 10.1149/1.2129345.

[53] R. Borup *et al.*, “Scientific Aspects of Polymer Electrolyte Fuel Cell Durability and Degradation,” *Chem. Rev.*, vol. 107, no. 10, pp. 3904–3951, Oct. 2007, doi: 10.1021/cr0501821.

[54] P. W. Voorhees, “The theory of Ostwald ripening,” *J Stat Phys*, vol. 38, no. 1, pp. 231–252, Jan. 1985, doi: 10.1007/BF01017860.

[55] C. T. Campbell, S. C. Parker, and D. E. Starr, “The Effect of Size-Dependent Nanoparticle Energetics on Catalyst Sintering,” *Science*, vol. 298, no. 5594, pp. 811–814, Oct. 2002, doi: 10.1126/science.1075094.

[56] S. Cherevko, N. Kulyk, and K. J. J. Mayrhofer, “Durability of platinum-based fuel cell electrocatalysts: Dissolution of bulk and nanoscale platinum,” *Nano Energy*, vol. 29, pp. 275–298, Nov. 2016, doi: 10.1016/j.nanoen.2016.03.005.

[57] L. Tang, X. Li, R. C. Cammarata, C. Friesen, and K. Sieradzki, “Electrochemical Stability of Elemental Metal Nanoparticles,” *J. Am. Chem. Soc.*, vol. 132, no. 33, pp. 11722–11726, Aug. 2010, doi: 10.1021/ja104421t.

[58] W. Bi and T. F. Fuller, “Modeling of PEM fuel cell Pt/C catalyst degradation,” *Journal of Power Sources*, vol. 178, no. 1, pp. 188–196, Mar. 2008, doi: 10.1016/j.jpowsour.2007.12.007.

[59] E. F. Holby, W. Sheng, Y. Shao-Horn, and D. Morgan, “Pt nanoparticle stability in PEM fuel cells : influence of particle size distribution and crossover hydrogen,” *Energy & Environmental Science*, vol. 2, no. 8, pp. 865–871, 2009, doi: 10.1039/B821622N.

[60] X. Wang, R. Kumar, and D. J. Myers, “Effect of Voltage on Platinum Dissolution: Relevance to Polymer Electrolyte Fuel Cells,” *Electrochem. Solid-State Lett.*, vol. 9, no. 5, p. A225, Mar. 2006, doi: 10.1149/1.2180536.

[61] S. G. Rinaldo, J. Stumper, and M. Eikerling, “Physical Theory of Platinum Nanoparticle Dissolution in Polymer Electrolyte Fuel Cells,” *J. Phys. Chem. C*, vol. 114, no. 13, pp. 5773–5785, Apr. 2010, doi: 10.1021/jp9101509.

[62] S. G. Rinaldo *et al.*, “Theoretical analysis of electrochemical surface-area loss in supported nanoparticle catalysts,” *Phys. Chem. Chem. Phys.*, vol. 16, no. 48, pp. 26876–26886, Nov. 2014, doi: 10.1039/C4CP03349C.

[63] J. A. S. Bett, K. Kinoshita, and P. Stonehart, “Crystallite growth of platinum dispersed on graphitized carbon black: II. Effect of liquid environment,” *Journal of Catalysis*, vol. 41, no. 1, pp. 124–133, Jan. 1976, doi: 10.1016/0021-9517(76)90207-4.

[64] P. J. Ferreira *et al.*, “Instability of Pt/C Electrocatalysts in Proton Exchange Membrane Fuel Cells: A Mechanistic Investigation,” *J. Electrochem. Soc.*, vol. 152, no. 11, p. A2256, Oct. 2005, doi: 10.1149/1.2050347.

[65] R. M. Darling and J. P. Meyers, “Mathematical Model of Platinum Movement in PEM Fuel Cells,” *J. Electrochem. Soc.*, vol. 152, no. 1, p. A242, 2005, doi: 10.1149/1.1836156.

[66] W. Bi, G. E. Gray, and T. F. Fuller, “PEM Fuel Cell Pt/C Dissolution and Deposition in Nafion Electrolyte,” *Electrochem. Solid-State Lett.*, vol. 10, no. 5, p. B101, Mar. 2007, doi: 10.1149/1.2712796.

[67] J. Thangavelautham and S. Dubowsky, “On the Catalytic Degradation in Fuel Cell Power Supplies for Long-Life Mobile Field Sensors,” *Fuel Cells*, vol. 13, no. 2, pp. 181–195, 2013, doi: 10.1002/fuce.201200065.

[68] P. Schneider, C. Sadeler, A.-C. Scherzer, N. Zamel, and D. Gerteisen, “Fast and Reliable State-of-Health Model of a PEM Cathode Catalyst Layer,” *J. Electrochem. Soc.*, vol. 166, no. 4, p. F322, Mar. 2019, doi: 10.1149/2.0881904jes.

[69] A. Kregar and T. Katrašnik, “Theoretical analysis of particle size re-distribution due to Ostwald ripening in the fuel cell catalyst layer,” *Open Physics*, vol. 17, no. 1, pp. 779–789, Jan. 2019, doi: 10.1515/phys-2019-0081.

[70] A. Kregar, G. Tavčar, A. Kravos, and T. Katrašnik, “Predictive system-level modeling framework for transient operation and cathode platinum degradation of high temperature proton exchange membrane fuel cells☆,” *Applied Energy*, vol. 263, p. 114547, Apr. 2020, doi: 10.1016/j.apenergy.2020.114547.

[71] G. Tavčar and T. Katrašnik, “An Innovative Hybrid 3D Analytic-Numerical Approach for System Level Modelling of PEM Fuel Cells,” *Energies*, vol. 6, no. 10, Art. no. 10, Oct. 2013, doi: 10.3390/en6105426.

[72] H. A. Baroody and E. Kjeang, “Predicting Platinum Dissolution and Performance Degradation under Drive Cycle Operation of Polymer Electrolyte Fuel Cells,” *J. Electrochem. Soc.*, vol. 168, no. 4, p. 044524, Apr. 2021, doi: 10.1149/1945-7111/abf5aa.

[73] M. Shojayian and E. Kjeang, “Simulation of cathode catalyst durability under fuel cell vehicle operation –Effects of stack size and temperature,” *Journal of Power Sources*, vol. 591, p. 233820, Jan. 2024, doi: 10.1016/j.jpowsour.2023.233820.

[74] M. Haslinger and T. Lauer, “Analyzing local degradation in an industrial PEMFC under EPA US06 drive cycle via 3D-CFD,” *Journal of Power Sources*, vol. 606, p. 234523, Jun. 2024, doi: 10.1016/j.jpowsour.2024.234523.

[75] J. Fu *et al.*, “A Hierarchical Optimizing Energy Management Strategy for Alleviating Degradation in Fuel Cell Hybrid System,” *IEEE Access*, vol. 12, pp. 57117–57127, 2024, doi: 10.1109/ACCESS.2024.3386366.

[76] W. Touil, Z. Li, R. Outbib, D. Hissel, and S. Jemei, “A system-level modeling framework for predicting Pt catalyst degradation in proton exchange membrane fuel cells,” *Journal of Power Sources*, vol. 625, p. 235628, Jan. 2025, doi: 10.1016/j.jpowsour.2024.235628.

[77] E. F. Holby and D. Morgan, “Application of Pt Nanoparticle Dissolution and Oxidation Modeling to Understanding Degradation in PEM Fuel Cells,” *J. Electrochem. Soc.*, vol. 159, no. 5, p. B578, Mar. 2012, doi: 10.1149/2.011204jes.

[78] Y. Li, K. Moriyama, W. Gu, S. Arisetty, and C. Y. Wang, “A One-Dimensional Pt Degradation Model for Polymer Electrolyte Fuel Cells,” *J. Electrochem. Soc.*, vol. 162, no. 8, p. F834, May 2015, doi: 10.1149/2.0101508jes.

[79] Y. Li and C. Y. Wang, “Modeling of Transient Platinum Degradation in a Low Pt-Loading PEFC under Current Cycling,” *J. Electrochem. Soc.*, vol. 164, no. 2, p. F171, Jan. 2017, doi: 10.1149/2.0081704jes.

[80] Z. Zheng *et al.*, “Voltage Cycling-Induced Pt Degradation in Proton Exchange Membrane Fuel Cells: Effect of Cycle Profiles,” *ACS Appl. Mater. Interfaces*, vol. 12, no. 31, pp. 35088–35097, Aug. 2020, doi: 10.1021/acsami.0c09883.

[81] W. Zheng, L. Xu, Z. Hu, Y. Zhao, J. Li, and M. Ouyang, “Dynamic modeling of Pt degradation and mitigation strategies in polymer electrolyte membrane fuel cells,” *eTransportation*, vol. 12, p. 100171, May 2022, doi: 10.1016/j.etran.2022.100171.

[82] V. A. Kovtunenko and L. Karpenko-Jereb, “Study of voltage cycling conditions on Pt oxidation and dissolution in polymer electrolyte fuel cells,” *Journal of Power Sources*, vol. 493, p. 229693, May 2021, doi: 10.1016/j.jpowsour.2021.229693.

[83] V. A. Kovtunenko and L. Karpenko-Jereb, “Lifetime of Catalyst under Voltage Cycling in Polymer Electrolyte Fuel Cell Due to Platinum Oxidation and Dissolution,” *Technologies*, vol. 9, no. 4, Art. no. 4, Dec. 2021, doi: 10.3390/technologies9040080.

[84] V. A. Kovtunenko, “Variance-Based Sensitivity Analysis of Fitting Parameters to Impact on Cycling Durability of Polymer Electrolyte Fuel Cells,” *Technologies*, vol. 10, no. 6, Art. no. 6, Dec. 2022, doi: 10.3390/technologies10060111.

[85] V. A. Kovtunenko, “The Holby–Morgan Model of Platinum Catalyst Degradation in PEM Fuel Cells: Range of Feasible Parameters Achieved Using Voltage Cycling,” *Technologies*, vol. 11, no. 6, Art. no. 6, Dec. 2023, doi: 10.3390/technologies11060184.

[86] V. A. Kovtunenko, “Feasible domain of cycling operating conditions and model parameters for Holby–Morgan model of platinum catalyst degradation in PEMFC,” *International Journal of Hydrogen Energy*, vol. 51, pp. 1518–1526, Jan. 2024, doi: 10.1016/j.ijhydene.2023.11.182.

[87] V. A. Kovtunenko, “Particle Size Distribution in Holby–Morgan Degradation Model of Platinum on Carbon Catalyst in Fuel Cell: Normal Distribution,” *Technologies*, vol. 12, no. 10, Art. no. 10, Oct. 2024, doi: 10.3390/technologies12100202.

[88] V. A. Kovtunenko, “Impact of Log-Normal Particle Size Distribution in Holby–Morgan Degradation Model on Aging of Pt/C Catalyst in PEMFC,” *Technologies*, vol. 13, no. 7, Art. no. 7, Jul. 2025, doi: 10.3390/technologies13070262.

[89] N. Goswami, J. B. Grunewald, T. F. Fuller, and P. P. Mukherjee, “Mechanistic interactions in polymer electrolyte fuel cell catalyst layer degradation,” *Journal of Materials Chemistry A*, vol. 10, no. 28, pp. 15101–15115, 2022, doi: 10.1039/D2TA02177C.

[90] Y. Zhu, Z. Qu, G. Zhang, and B. Yu, “A one-dimensional model for Pt degradation and precipitation in proton exchange membrane fuel cell considering Pt nucleation, particle size growth, and band formation,” *Electrochimica Acta*, vol. 475, p. 143590, Jan. 2024, doi: 10.1016/j.electacta.2023.143590.

[91] C. Sheng *et al.*, “Optimal energy management strategies for hybrid power systems considering Pt degradation,” *Applied Energy*, vol. 360, p. 122764, Apr. 2024, doi: 10.1016/j.apenergy.2024.122764.

[92] E. Dong, H. Zhao, R. Zhang, L. Chen, and W.-Q. Tao, “Effects of gradient structures of cathode catalyst layers on performance and durability of proton exchange membrane fuel cells,” *Electrochimica Acta*, vol. 477, p. 143772, Feb. 2024, doi: 10.1016/j.electacta.2024.143772.

[93] Z. Huang *et al.*, “Three-dimensional modeling for a 100 cm2 PEMFC with different Pt loadings under cathode Pt catalyst degradation,” *International Journal of Hydrogen Energy*, vol. 53, pp. 1107–1122, Jan. 2024, doi: 10.1016/j.ijhydene.2023.12.118.

[94] Y. Hu, M. Hao, and Y. Li, “Modelling catalyst degradation in proton exchange membrane fuel cell: Heterogeneous Pt degradation and cell performance loss,” *Electrochimica Acta*, vol. 536, p. 146702, Oct. 2025, doi: 10.1016/j.electacta.2025.146702.

[95] S. G. Rinaldo, W. Lee, J. Stumper, and M. Eikerling, “Model- and Theory-Based Evaluation of Pt Dissolution for Supported Pt Nanoparticle Distributions under Potential Cycling,” *Electrochem. Solid-State Lett.*, vol. 14, no. 5, p. B47, Feb. 2011, doi: 10.1149/1.3548504.

[96] S. G. Rinaldo, W. Lee, J. Stumper, and M. Eikerling, “Nonmonotonic dynamics in Lifshitz-Slyozov-Wagner theory: Ostwald ripening in nanoparticle catalysts,” *Phys. Rev. E*, vol. 86, no. 4, p. 041601, Oct. 2012, doi: 10.1103/PhysRevE.86.041601.

[97] Y. Ding, Z. Fang, H. Zhang, X. Cheng, and L. Li, “Modeling the non-uniform degradation of PEM fuel cell catalyst with a multi-scale framework based on population balance equation,” *Chemical Engineering Journal*, vol. 506, p. 159960, Jan. 2025, doi: 10.1016/j.cej.2025.159960.

[98] P. Urchaga *et al.*, “Catalyst Degradation in Fuel Cell Electrodes: Accelerated Stress Tests and Model-based Analysis,” *Electrochimica Acta*, vol. 176, pp. 1500–1510, Sep. 2015, doi: 10.1016/j.electacta.2015.03.152.

[99] H. A. Baroody, D. B. Stolar, and M. H. Eikerling, “Modelling-based data treatment and analytics of catalyst degradation in polymer electrolyte fuel cells,” *Electrochimica Acta*, vol. 283, pp. 1006–1016, Sep. 2018, doi: 10.1016/j.electacta.2018.06.108.

[100] Y. Wang, S. J. Moura, S. G. Advani, and A. K. Prasad, “Power management system for a fuel cell/battery hybrid vehicle incorporating fuel cell and battery degradation,” *International Journal of Hydrogen Energy*, vol. 44, no. 16, pp. 8479–8492, Mar. 2019, doi: 10.1016/j.ijhydene.2019.02.003.

[101] Y. Ao, S. Laghrouche, D. Depernet, and K. Chen, “Lifetime prediction for proton exchange membrane fuel cell under real driving cycles based on platinum particle dissolve model,” *International Journal of Hydrogen Energy*, vol. 45, no. 56, pp. 32388–32401, Nov. 2020, doi: 10.1016/j.ijhydene.2020.08.188.

[102] Y. Ao, K. Chen, S. Laghrouche, and D. Depernet, “Proton exchange membrane fuel cell degradation model based on catalyst transformation theory,” *Fuel Cells*, vol. 21, no. 3, pp. 254–268, 2021, doi: 10.1002/fuce.202100002.

[103] Y. Ding, Z. Fang, Y. Yuan, M. Tian, J. Yu, and L. Li, “Particle size distribution degradation model for PEM fuel cell Pt/C catalyst based on population balance equation,” *Chemical Engineering Science*, vol. 300, p. 120590, Dec. 2024, doi: 10.1016/j.ces.2024.120590.

[104] F. Hiraoka, Y. Kohno, K. Matsuzawa, and S. Mitsushima, “A Simulation Study of Pt Particle Degradation During Potential Cycling Using a Dissolution/Deposition Model,” *Electrocatalysis*, vol. 6, no. 1, pp. 102–108, Jan. 2015, doi: 10.1007/s12678-014-0225-y.

[105] M. Prokop, R. Kodym, T. Bystron, M. Drakselova, M. Paidar, and K. Bouzek, “Degradation kinetics of Pt during high-temperature PEM fuel cell operation part II: Dissolution kinetics of Pt incorporated in a catalyst layer of a gas-diffusion electrode,” *Electrochimica Acta*, vol. 333, p. 135509, Feb. 2020, doi: 10.1016/j.electacta.2019.135509.

[106] M. Prokop, R. Kodym, T. Bystron, M. Paidar, and K. Bouzek, “Degradation kinetics of Pt during high-temperature PEM fuel cell operation part I: Kinetics of Pt surface oxidation and dissolution in concentrated H3PO4 electrolyte at elevated temperatures,” *Electrochimica Acta*, vol. 313, pp. 352–366, Aug. 2019, doi: 10.1016/j.electacta.2019.04.144.

[107] M. Prokop *et al.*, “Degradation kinetics of Pt during high-temperature PEM fuel cell operation Part III: Voltage-dependent Pt degradation rate in single-cell experiments,” *Electrochimica Acta*, vol. 363, p. 137165, Dec. 2020, doi: 10.1016/j.electacta.2020.137165.

[108] C. Robin, M. Gérard, M. Quinaud, J. d’Arbigny, and Y. Bultel, “Proton exchange membrane fuel cell model for aging predictions: Simulated equivalent active surface area loss and comparisons with durability tests,” *Journal of Power Sources*, vol. 326, pp. 417–427, Sep. 2016, doi: 10.1016/j.jpowsour.2016.07.018.

[109] M. Mayur, M. Gerard, P. Schott, and W. G. Bessler, “Lifetime Prediction of a Polymer Electrolyte Membrane Fuel Cell under Automotive Load Cycling Using a Physically-Based Catalyst Degradation Model,” *Energies*, vol. 11, no. 8, Art. no. 8, Aug. 2018, doi: 10.3390/en11082054.

[110] M. Moein-Jahromi, M. J. Kermani, and S. Movahed, “Degradation forecast for PEMFC cathode-catalysts under cyclic loads,” *Journal of Power Sources*, vol. 359, pp. 611–625, Aug. 2017, doi: 10.1016/j.jpowsour.2017.05.102.

[111] W. Bi and T. Fuller, “Temperature Effects on PEM Fuel Cells Pt/C Catalyst Degradation,” *ECS Trans.*, vol. 11, no. 1, p. 1235, Sep. 2007, doi: 10.1149/1.2781037.

[112] M. Moein-Jahromi and M. J. Kermani, “Three-dimensional multiphase simulation and multi-objective optimization of PEM fuel cells degradation under automotive cyclic loads,” *Energy Conversion and Management*, vol. 231, p. 113837, Mar. 2021, doi: 10.1016/j.enconman.2021.113837.

[113] A. Baricci, M. Bonanomi, H. Yu, L. Guetaz, R. Maric, and A. Casalegno, “Modelling analysis of low platinum polymer fuel cell degradation under voltage cycling: Gradient catalyst layers with improved durability,” *Journal of Power Sources*, vol. 405, pp. 89–100, Nov. 2018, doi: 10.1016/j.jpowsour.2018.09.092.

[114] T. Takeshita, H. Murata, T. Hatanaka, and Y. Morimoto, “Analysis of Pt Catalyst Degradation of a PEFC Cathode by TEM Observation and Macro Model Simulation,” *ECS Trans.*, vol. 16, no. 2, p. 367, Oct. 2008, doi: 10.1149/1.2981871.

[115] A. A. Franco and M. Tembely, “Transient Multiscale Modeling of Aging Mechanisms in a PEFC Cathode,” *J. Electrochem. Soc.*, vol. 154, no. 7, p. B712, May 2007, doi: 10.1149/1.2731040.

[116] T. Jahnke, G. A. Futter, A. Baricci, C. Rabissi, and A. Casalegno, “Physical Modeling of Catalyst Degradation in Low Temperature Fuel Cells: Platinum Oxidation, Dissolution, Particle Growth and Platinum Band Formation,” *J. Electrochem. Soc.*, vol. 167, no. 1, p. 013523, Nov. 2019, doi: 10.1149/2.0232001JES.

[117] A. Van-Brunt, V. A. Beck, and B. M. Stühmeier, “Platinum Coarsening: Multiscale Analysis and Asymptotics in Proton Exchange Membrane Fuel Cells,” *J. Electrochem. Soc.*, vol. 172, no. 6, p. 064505, Jun. 2025, doi: 10.1149/1945-7111/addd4d.

[118] Y. Pan, H. Wang, and N. P. Brandon, “Integrated catalyst and membrane degradation model for proton exchange membrane fuel cells,” *Electrochimica Acta*, vol. 538, p. 146921, Oct. 2025, doi: 10.1016/j.electacta.2025.146921.

[119] R. K. Ahluwalia *et al.*, “Thermodynamics and Kinetics of Platinum Dissolution from Carbon-Supported Electrocatalysts in Aqueous Media under Potentiostatic and Potentiodynamic Conditions,” *J. Electrochem. Soc.*, vol. 160, no. 4, p. F447, Mar. 2013, doi: 10.1149/2.018306jes.

[120] R. K. Ahluwalia *et al.*, “Dynamics of Particle Growth and Electrochemical Surface Area Loss due to Platinum Dissolution,” *J. Electrochem. Soc.*, vol. 161, no. 3, p. F291, Jan. 2014, doi: 10.1149/2.051403jes.

[121] S. Jomori, N. Nonoyama, and T. Yoshida, “Analysis and modeling of PEMFC degradation: Effect on oxygen transport,” *Journal of Power Sources*, vol. 215, pp. 18–27, Oct. 2012, doi: 10.1016/j.jpowsour.2012.04.069.

[122] G. Gwak *et al.*, “Analyzing oxygen transport resistance and Pt particle growth effect in the cathode catalyst layer of polymer electrolyte fuel cells,” *International Journal of Hydrogen Energy*, vol. 45, no. 24, pp. 13414–13427, May 2020, doi: 10.1016/j.ijhydene.2020.03.080.

[123] R. Zhang, T. Min, L. Chen, Q. Kang, Y.-L. He, and W.-Q. Tao, “Pore-scale and multiscale study of effects of Pt degradation on reactive transport processes in proton exchange membrane fuel cells,” *Applied Energy*, vol. 253, p. 113590, Nov. 2019, doi: 10.1016/j.apenergy.2019.113590.

[124] J. Gostick *et al.*, “OpenPNM: A Pore Network Modeling Package,” *Computing in Science & Engineering*, vol. 18, no. 4, pp. 60–74, Jul. 2016, doi: 10.1109/MCSE.2016.49.

[125] M. Prokop, M. Drakselova, and K. Bouzek, “Review of the experimental study and prediction of Pt-based catalyst degradation during PEM fuel cell operation,” *Current Opinion in Electrochemistry*, vol. 20, pp. 20–27, Apr. 2020, doi: 10.1016/j.coelec.2020.01.016.

[126] A. Golparvar, Y. Zhou, K. Wu, J. Ma, and Z. Yu, “A comprehensive review of pore scale modeling methodologies for multiphase flow in porous media,” *Advances in Geo-Energy Research*, vol. 2, no. 4, pp. 418–440, Dec. 2018, doi: 10.26804/ager.2018.04.07.

[127] H.-J. Vogel, J. Tölke, V. P. Schulz, M. Krafczyk, and K. Roth, “Comparison of a Lattice-Boltzmann Model, a Full-Morphology Model, and a Pore Network Model for Determining Capillary Pressure–Saturation Relationships,” *Vadose Zone Journal*, vol. 4, no. 2, pp. 380–388, 2005, doi: 10.2136/vzj2004.0114.

[128] L. Chen, G. Wu, E. F. Holby, P. Zelenay, W.-Q. Tao, and Q. Kang, “Lattice Boltzmann Pore-Scale Investigation of Coupled Physical-electrochemical Processes in C/Pt and Non-Precious Metal Cathode Catalyst Layers in Proton Exchange Membrane Fuel Cells,” *Electrochimica Acta*, vol. 158, pp. 175–186, Mar. 2015, doi: 10.1016/j.electacta.2015.01.121.

[129] K. J. Lange, P.-C. Sui, and N. Djilali, “Pore scale modeling of a proton exchange membrane fuel cell catalyst layer: Effects of water vapor and temperature,” *Journal of Power Sources*, vol. 196, no. 6, pp. 3195–3203, Mar. 2011, doi: 10.1016/j.jpowsour.2010.11.118.

[130] Y. Wang *et al.*, “Lattice Boltzmann simulation of cathode catalyst layer degradation on transport reaction process within a proton exchange membrane fuel cell,” *Green Energy and Resources*, vol. 1, no. 2, p. 100022, Jun. 2023, doi: 10.1016/j.gerr.2023.100022.

[131] R. Wu, Q. Liao, X. Zhu, and H. Wang, “Pore network modeling of cathode catalyst layer of proton exchange membrane fuel cell,” *International Journal of Hydrogen Energy*, vol. 37, no. 15, pp. 11255–11267, Aug. 2012, doi: 10.1016/j.ijhydene.2012.04.036.

[132] M. A. Sadeghi *et al.*, "Predicting PEMFC performance from a volumetric image of catalyst layer structure using pore network modeling," *Applied Energy*, vol. 353, p. 122004, Jan. 2024, doi: 10.1016/j.apenergy.2023.122004.

[133] N. Goswami, A. N. Mistry, J. B. Grunewald, T. F. Fuller, and P. P. Mukherjee, "Corrosion-Induced Microstructural Variability Affects Transport-Kinetics Interaction in PEM Fuel Cell Catalyst Layers," *J. Electrochem. Soc.*, vol. 167, no. 8, p. 084519, May 2020, doi: 10.1149/1945-7111/ab927c.

[134] G. Bucci, K. Gadelrab, and W. C. Carter, "Mesoscale Model for Ostwald Ripening of Catalyst Nanoparticles," *J. Electrochem. Soc.*, vol. 168, no. 5, p. 054515, May 2021, doi: 10.1149/1945-7111/abf970.

[135] J. P. Braaten, S. Ogawa, V. Yarlagadda, A. Kongkanand, and S. Litster, "Studying Pt-based fuel cell electrode degradation with nanoscale X-ray computed tomography," *Journal of Power Sources*, vol. 478, p. 229049, Dec. 2020, doi: 10.1016/j.jpowsour.2020.229049.

[136] J. T. Gostick *et al.*, "PoreSpy: A Python Toolkit for Quantitative Analysis of Porous Media Images," *Journal of Open Source Software*, vol. 4, no. 37, p. 1296, May 2019, doi: 10.21105/joss.01296.

[137] W. K. Epting and S. Litster, "Effects of an agglomerate size distribution on the PEFC agglomerate model," *International Journal of Hydrogen Energy*, vol. 37, no. 10, pp. 8505–8511, May 2012, doi: 10.1016/j.ijhydene.2012.02.099.

[138] T. E. Springer, T. A. Zawodzinski, and S. Gottesfeld, "Polymer Electrolyte Fuel Cell Model," *J. Electrochem. Soc.*, vol. 138, no. 8, p. 2334, Aug. 1991, doi: 10.1149/1.2085971.

[139] J. T. Hinatsu, M. Mizuhata, and H. Takenaka, "Water Uptake of Perfluorosulfonic Acid Membranes from Liquid Water and Water Vapor," *J. Electrochem. Soc.*, vol. 141, no. 6, p. 1493, Jun. 1994, doi: 10.1149/1.2054951.

[140] W. Olbrich, T. Kadyk, U. Sauter, M. Eikerling, and J. Gostick, "Structure and conductivity of ionomer in PEM fuel cell catalyst layers: a model-based analysis," *Sci Rep*, vol. 13, no. 1, p. 14127, Aug. 2023, doi: 10.1038/s41598-023-40637-0.

[141] L. Hao, K. Moriyama, W. Gu, and C.-Y. Wang, "Modeling and Experimental Validation of Pt Loading and Electrode Composition Effects in PEM Fuel Cells," *J. Electrochem. Soc.*, vol. 162, no. 8, p. F854, May 2015, doi: 10.1149/2.0221508jes.

[142] E. Pahon, D. Hissel, and N. Yousfi-Steiner, "A review of accelerated stress tests dedicated to proton exchange membrane fuel cells – Part I: Fuel cell component level," *Journal of Power Sources*, vol. 546, p. 231895, Oct. 2022, doi: 10.1016/j.jpowsour.2022.231895.

[143] D. M. Bernardi and M. W. Verbrugge, “A Mathematical Model of the Solid-Polymer-Electrolyte Fuel Cell,” *J. Electrochem. Soc.*, vol. 139, no. 9, p. 2477, Sep. 1992, doi: 10.1149/1.2221251.

[144] O. C. Bridgeman and E. W. Aldrich, “Vapor Pressure Tables for Water,” *Journal of Heat Transfer*, vol. 86, no. 2, pp. 279–286, May 1964, doi: 10.1115/1.3687121.

[145] K. Yasuda, A. Taniguchi, T. Akita, T. Ioroi, and Z. Siroma, “Platinum dissolution and deposition in the polymer electrolyte membrane of a PEM fuel cell as studied by potential cycling,” *Phys. Chem. Chem. Phys.*, vol. 8, no. 6, pp. 746–752, Feb. 2006, doi: 10.1039/B514342J.

[146] A. Kusoglu and A. Z. Weber, “New Insights into Perfluorinated Sulfonic-Acid Ionomers,” *Chem. Rev.*, vol. 117, no. 3, pp. 987–1104, Feb. 2017, doi: 10.1021/acs.chemrev.6b00159.

[147] K. Ehelebe *et al.*, “Platinum Dissolution in Realistic Fuel Cell Catalyst Layers,” *Angewandte Chemie International Edition*, vol. 60, no. 16, pp. 8882–8888, 2021, doi: 10.1002/anie.202014711.

[148] S. Thiele, R. Zengerle, and C. Ziegler, “Nano-morphology of a polymer electrolyte fuel cell catalyst layer—imaging, reconstruction and analysis,” *Nano Res.*, vol. 4, no. 9, pp. 849–860, Sep. 2011, doi: 10.1007/s12274-011-0141-x.

[149] Z. Zheng *et al.*, “Design of gradient cathode catalyst layer (CCL) structure for mitigating Pt degradation in proton exchange membrane fuel cells (PEMFCs) using mathematical method,” *Journal of Power Sources*, vol. 451, p. 227729, Mar. 2020, doi: 10.1016/j.jpowsour.2020.227729.

[150] S. Hegde, R. Wörner, and B. Shabani, “Automotive PEM fuel cell catalyst layer degradation mechanisms and characterisation techniques, Part II: Platinum degradation,” *International Journal of Hydrogen Energy*, vol. 143, pp. 179–212, Jul. 2025, doi: 10.1016/j.ijhydene.2025.05.034.

[151] H. Yu *et al.*, “Strategies to mitigate Pt dissolution in low Pt loading proton exchange membrane fuel cell: I. A gradient Pt particle size design,” *Electrochimica Acta*, vol. 247, pp. 1155–1168, Sep. 2017, doi: 10.1016/j.electacta.2017.07.093.

[152] H. Yu, A. Baricci, A. Casalegno, L. Guetaz, L. Bonville, and R. Maric, “Strategies to mitigate Pt dissolution in low Pt loading proton exchange membrane fuel cell: II. A gradient Pt loading design,” *Electrochimica Acta*, vol. 247, pp. 1169–1179, Sep. 2017, doi: 10.1016/j.electacta.2017.06.145.

[153] W. Shi, A.-H. Park, and Y.-U. Kwon, “Scalable synthesis of (Pd,Cu)@Pt core-shell catalyst with high ORR activity and durability,” *Journal of Electroanalytical Chemistry*, vol. 918, p. 116451, Aug. 2022, doi: 10.1016/j.jelechem.2022.116451.

[154] J. Cao, H. Cao, J. Shen, F. Wang, and H. Zhu, "Impact of CuFe bimetallic core on the electrocatalytic activity and stability of Pt shell for oxygen reduction reaction," *Electrochimica Acta*, vol. 350, p. 136205, Aug. 2020, doi: 10.1016/j.electacta.2020.136205.

[155] Y. Shao, J.-P. Dodelet, G. Wu, and P. Zelenay, "PGM-Free Cathode Catalysts for PEM Fuel Cells: A Mini-Review on Stability Challenges," *Advanced Materials*, vol. 31, no. 31, p. 1807615, 2019, doi: 10.1002/adma.201807615.

[156] Z. Zheng, L. Luo, S. Shen, G. Wei, and J. Zhang, "Insight into the potential strategies for mitigating Pt degradation in proton exchange membrane fuel cells (PEMFCs): From the perspective of Pt ion transport," *Journal of Power Sources*, vol. 522, p. 230999, Feb. 2022, doi: 10.1016/j.jpowsour.2022.230999.

[157] G. J. B. Agravante and J. T. Gostick, "Physics-Based Modeling of Platinum Catalyst Dissolution and Oxidation in PEM Fuel Cells: A Focused Review," *J. Electrochem. Soc.*, vol. 173, no. 7, p. 074507, Apr. 2026, doi: 10.1149/1945-7111/ae5740.

[158] A. Saeidfar, A. C. Kirlioglu, S. A. Gursel, and S. Yesilyurt, "Role of catalyst layer composition in the degradation of low platinum-loaded proton exchange membrane fuel cell cathodes: An experimental analysis," *Journal of Power Sources*, vol. 625, p. 235676, Jan. 2025, doi: 10.1016/j.jpowsour.2024.235676.

[159] G. J. B. Agravante and J. T. Gostick, "Simulating transient pore-scale behaviour of platinum degradation in PEM fuel cells using pore network modeling," *Journal of Power Sources*, vol. 663, p. 238878, Jan. 2026, doi: 10.1016/j.jpowsour.2025.238878.

[160] M. T. Q. S. da Silva, M. do Rocio Cardoso, C. M. P. Veronese, and W. Mazer, "Tortuosity: A brief review," *Materials Today: Proceedings*, vol. 58, pp. 1344–1349, Jan. 2022, doi: 10.1016/j.matpr.2022.02.228.

[161] B. Ghanbarian, A. G. Hunt, R. P. Ewing, and M. Sahimi, "Tortuosity in Porous Media: A Critical Review," *Soil Science Society of America Journal*, vol. 77, no. 5, pp. 1461–1477, 2013, doi: 10.2136/sssaj2012.0435.

[162] J. M. Zalc, S. C. Reyes, and E. Iglesia, "The effects of diffusion mechanism and void structure on transport rates and tortuosity factors in complex porous structures," *Chemical Engineering Science*, vol. 59, no. 14, pp. 2947–2960, Jul. 2004, doi: 10.1016/j.ces.2004.04.028.

[163] P.-Y. Lanfrey, Z. V. Kuzeljevic, and M. P. Dudukovic, "Tortuosity model for fixed beds randomly packed with identical particles," *Chemical Engineering Science*, vol. 65, no. 5, pp. 1891–1896, Mar. 2010, doi: 10.1016/j.ces.2009.11.011.

[164] S. Li, J. Yuan, G. Xie, and B. Sundén, "Effects of agglomerate model parameters on transport characterization and performance of PEM fuel cells," *International Journal of Hydrogen Energy*, vol. 43, no. 17, pp. 8451–8463, Apr. 2018, doi: 10.1016/j.ijhydene.2018.03.106.

[165] A. Putz, J. Hinebaugh, H. Day, M. Aghighi, A. Bazylak, and J. T. Gostick, “Introducing OpenPNM: An Open Source Pore Network Modeling Framework for General Scientific Applications,” *Meet. Abstr.*, vol. MA2013-02, no. 15, p. 1256, Oct. 2013, doi: 10.1149/MA2013-02/15/1256.

[166] K. Yu, C. Li, J. Xie, and P. J. Ferreira, “Understanding the Degradation Mechanisms of Pt Electrocatalysts in PEMFCs by Combining 2D and 3D Identical Location TEM,” *Nano Lett.*, vol. 23, no. 5, pp. 1858–1864, Mar. 2023, doi: 10.1021/acs.nanolett.2c04764.

[167] M. Sabharwal and M. Secanell, “Understanding the effect of porosity and pore size distribution on low loading catalyst layers,” *Electrochimica Acta*, vol. 419, p. 140410, Jul. 2022, doi: 10.1016/j.electacta.2022.140410.

[168] H. Nguyen, C. Klose, L. Metzler, S. Vierrath, and M. Breitwieser, “Fully Hydrocarbon Membrane Electrode Assemblies for Proton Exchange Membrane Fuel Cells and Electrolyzers: An Engineering Perspective,” *Advanced Energy Materials*, vol. 12, no. 12, p. 2103559, 2022, doi: 10.1002/aenm.202103559.

[169] H. Li *et al.*, “Revealing the Oxygen Transport Challenges in Catalyst Layers in Proton Exchange Membrane Fuel Cells and Water Electrolysis,” *Nano-Micro Lett.*, vol. 17, no. 1, p. 225, Apr. 2025, doi: 10.1007/s40820-025-01719-y.

[170] S. Dou, L. Hao, Q. Wang, and H. Liu, “Effects of agglomerate structure and operating humidity on the catalyst layer performance of PEM fuel cells,” *Applied Energy*, vol. 355, p. 122211, Feb. 2024, doi: 10.1016/j.apenergy.2023.122211.

[171] M. Ayoub, T. Böhm, M. Bierling, S. Thiele, and M. Brodt, “Review—Graded Catalyst Layers in Hydrogen Fuel Cells - A Pathway to Application-Tailored Cells,” *J. Electrochem. Soc.*, vol. 171, no. 9, p. 094503, Sep. 2024, doi: 10.1149/1945-7111/ad73a7.

[172] M. Mandal, A. Valls, N. Gangnus, and M. Secanell, “Analysis of Inkjet Printed Catalyst Coated Membranes for Polymer Electrolyte Electrolyzers,” *J. Electrochem. Soc.*, vol. 165, no. 7, p. F543, May 2018, doi: 10.1149/2.1101807jes.

[173] Z. Xie *et al.*, “Functionally Graded Cathode Catalyst Layers for Polymer Electrolyte Fuel Cells: II. Experimental Study of the Effect of Nafion Distribution,” *J. Electrochem. Soc.*, vol. 152, no. 6, p. A1171, May 2005, doi: 10.1149/1.1904990.

[174] J. Sharma *et al.*, “Catalyst layer formulations for slot-die coating of PEM fuel cell electrodes,” *International Journal of Hydrogen Energy*, vol. 47, no. 84, pp. 35838–35850, Oct. 2022, doi: 10.1016/j.ijhydene.2022.08.157.

[175] L. Ney *et al.*, “Screen Printing Catalyst Inks With Enhanced Process Stability for PEM Fuel Cell Production,” *Fuel Cells*, vol. 25, no. 2, p. e202400158, 2025, doi: 10.1002/fuce.202400158.

[176] S. A. Mauger, K. C. Neyerlin, A. C. Yang-Neyerlin, K. L. More, and M. Ulsh, "Gravure Coating for Roll-to-Roll Manufacturing of Proton-Exchange-Membrane Fuel Cell Catalyst Layers," *J. Electrochem. Soc.*, vol. 165, no. 11, p. F1012, Sep. 2018, doi: 10.1149/2.0091813jes.

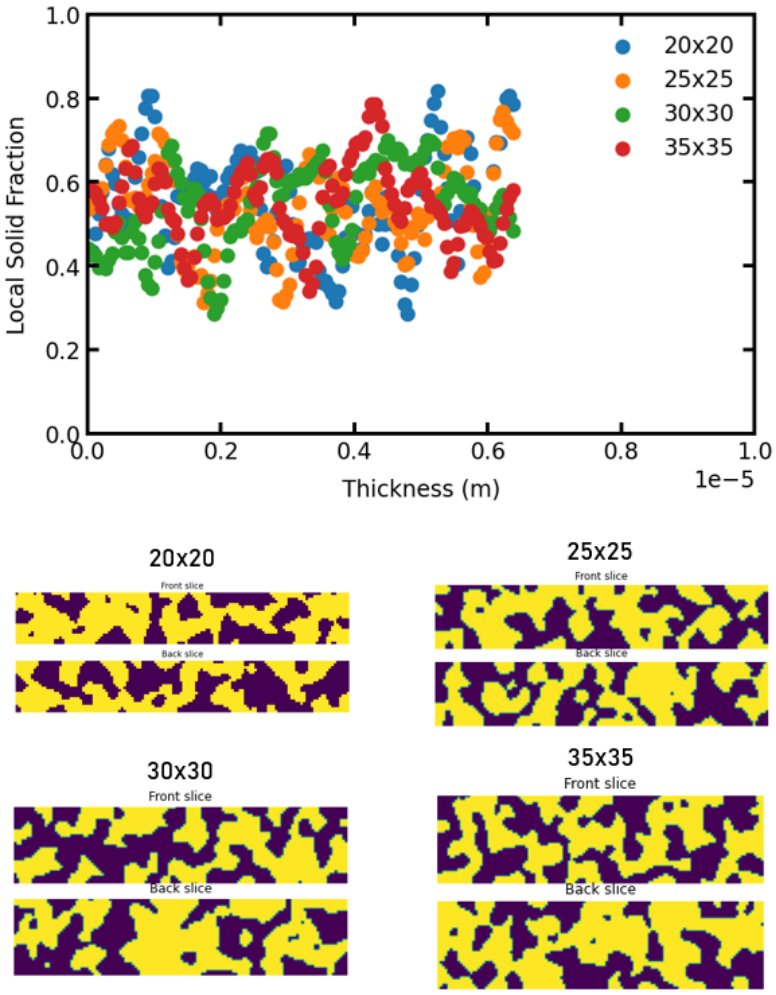
[177] G. Agravante and J. Gostick, "Model-informed strategies for mitigating platinum loss in polymer electrolyte membrane fuel cells," Apr. 2026, doi: 10.26434/chemrxiv.15001758/v1.

[178] M. T. Coats *et al.*, "Quantifying the Degradation of the Cathode Catalyst Layer Under Voltage Cycling Conditions Using Transmission Electron Microscopy Techniques," *J. Electrochem. Soc.*, vol. 172, no. 3, p. 034510, Mar. 2025, doi: 10.1149/1945-7111/adbd7a.

Appendix A
Modifications to the Blob Generation Algorithm

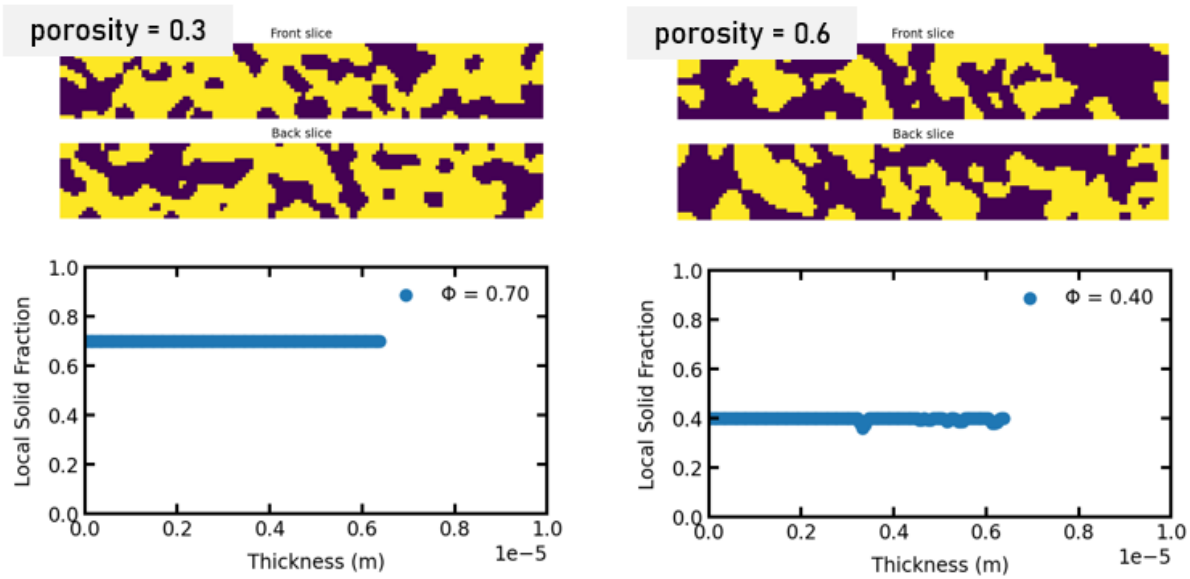
The blob generation algorithm in PoreSpy creates porous media by generating random noise within a specified image domain, applying a Gaussian blur, and thresholding the field to obtain a specified porosity. This results in a binary image suitable for porous media simulations.

For the purposes of this study, it is necessary to maintain a controlled porosity profile in the through-plane direction to avoid introducing unintended geometric constrictions. In the original algorithm, variations in the thresholded noise field lead to slice-wise fluctuations in local porosity. While these fluctuations are typically negligible in large domains (such as a full CCL domain), they become significant when operating in a reduced strip geometry, as used here for computational feasibility.



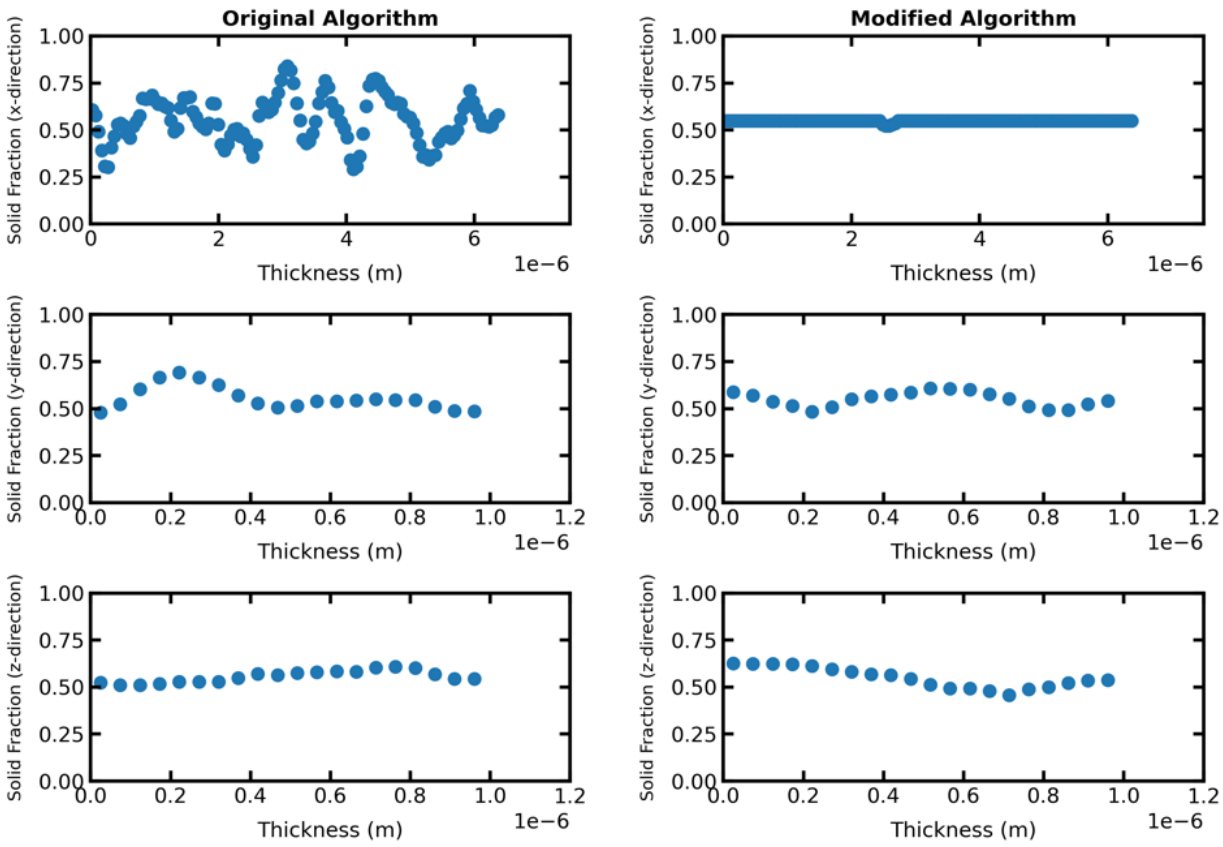
The figure above shows the variations in local solid fraction in each through-plane slice (x-direction) for domains of varying in-plane size (20×20 to 35×35 voxels) over a 130-voxel-thick catalyst layer. Even in the largest geometry considered, the slice-averaged porosity varies by approximately ±0.2. This magnitude of variation could introduce artificial constrictions along the through-plane direction. These artificially generated constrictions are inaccurate and may influence both performance and degradation simulations. Furthermore, these uncontrolled variations make it difficult to impose intentional spatial porosity gradients, as the fluctuations can obscure the specified structural modifications.

To address this, the blob generation algorithm was modified to enforce slice-wise porosity control. In this revised approach, two-dimensional blob fields are generated independently in each slice with a specified porosity. These slices are then stacked to construct the three-dimensional domain, after which unconnected solid regions are removed to ensure geometric consistency. This procedure retains the desired porosity profile and preserves realistic agglomerate-like morphology.



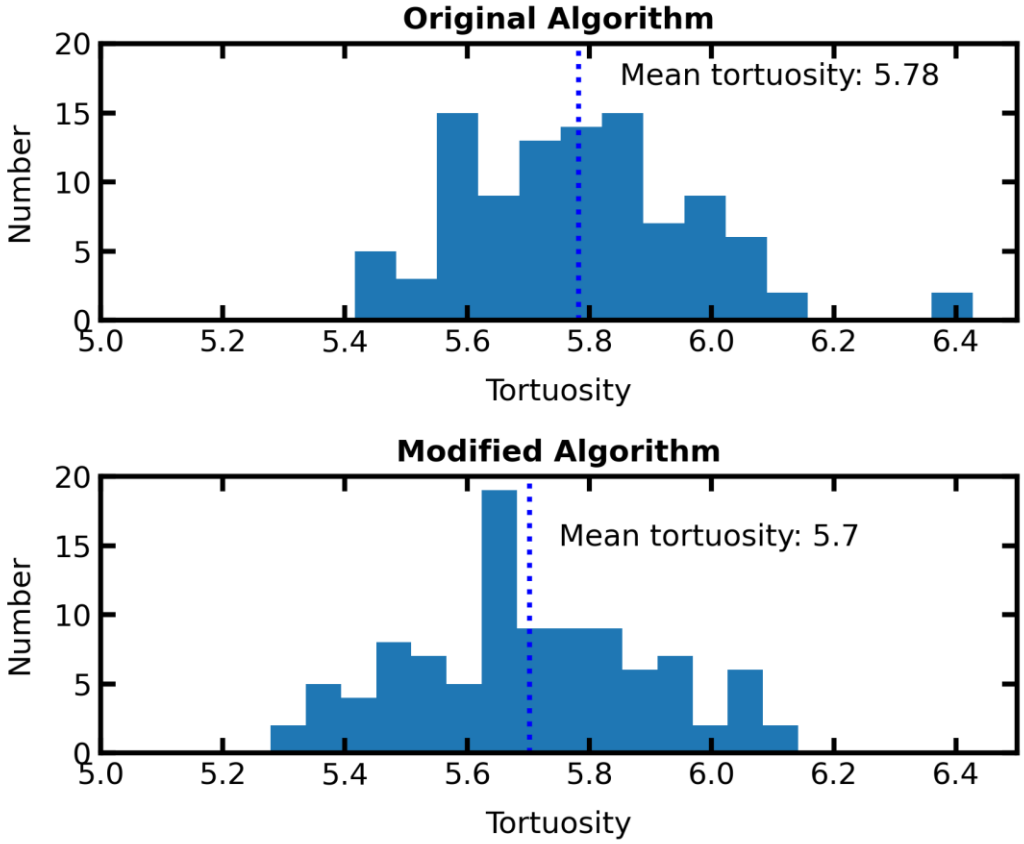
As shown above, the modified approach produces geometries with clearly defined agglomerates and visually consistent porous structures for different uniform porosity values. Although the effect of removing floating solids becomes more pronounced at lower porosity values since reduced porosity naturally increases this likelihood, the overall porosity remains approximately uniform, with variations on the order of ±0.05.

To validate the modified method, porosity profiles in all three spatial directions were compared between the original and modified algorithms.



The two approaches produce the same random variations in the in-plane directions, while the modified algorithm successfully suppresses the porosity variations in the through-plane direction.

Finally, transport equivalence was assessed by extracting pore networks from the generated images and running diffusion simulations under identical conditions using geometries produced by both methods. For each approach, 100 steady-state diffusion simulations were conducted on 50 × 50 × 50 samples with a porosity of 0.45 to determine the effective diffusivity and corresponding tortuosity. This allowed us to evaluate whether the transport behavior remained consistent between the two methods.



The resulting tortuosity distributions are nearly identical, with mean values of 5.78 and 5.70 for the original and modified approaches, respectively, and most values ranging between 5.5 and 6. The close agreement confirms that the modified algorithm preserves the transport characteristics of the geometry while providing improved control over the through-plane porosity distribution. Therefore, the revised method was adopted for all simulations presented in this work.

Appendix B
Metric Calculation

The following table summarizes the metrics used to evaluate performance and degradation, along with their selected indicators, formulations, and the expressions used to quantify relative improvement with respect to a base case.

Metric	Selected Indicator	Formulation	Relative improvement over base case
Initial Performance	Initial current density at 0.6 V	Polarization curve from the performance solver, $J_{0.6V}$	**Current density increase at 0.6 V** $\frac{J_{0.6V} - J_{0.6V,bc}}{J_{0.6V,bc}}$
Degradation Reduction	Total ECSA loss after 5 cycles	$SA_{total}^{loss} = 1 - \sum_{i=1}^{n_{Pt}} \frac{SA_{i,5cyc}}{SA_{i,BOL}}$	**ECSA loss reduction at 5 cycles** $\frac{SA_{total,bc}^{loss} - SA_{total}^{loss}}{SA_{total,bc}^{loss}}$
Degradation Homogeneity	Coefficient of Variation (through-plane) of ECSA loss after 5 cycles	$CoV_{tp} = \frac{\sigma_{tp}}{\mu_{tp}}$	**ECSA loss CoV reduction at 5 cycles** $\frac{CoV_{tp,bc} - CoV_{tp}}{CoV_{tp,bc}}$

A brief description of each metric and the associated equations is provided below.

Initial Performance

Initial performance quantifies how effectively the catalyst layer structure facilitates the oxygen reduction reaction. It is evaluated using the polarization curve generated by the performance solver. The current density at 0.6 V is selected as the performance indicator, as 0.6 V corresponds to the lowest voltage considered in the accelerated stress test range. At this voltage, the current density reflects the combined effects of kinetic, ohmic, and mass transport losses and provides a representative measure of performance under high current density. While this choice is somewhat arbitrary, it enables consistent comparison across all cases.

Degradation Reduction

Overall degradation reduction characterizes the extent of platinum degradation across the catalyst layer and is quantified using the total electrochemically active surface area (ECSA) loss after five cycles. The surface area of platinum particles within each pore, i, assuming spherical particles, is given by

$$SA_i = 4\pi r_i^2 n_i$$

where r_i the particle radius and n_i is the number of particles in pore i.

The total ECSA loss provides a widely used metric in the literature for assessing catalyst degradation, as a reduction in available surface area directly correlates with performance losses. However, total ECSA loss alone does not fully capture degradation effects, since access to catalytic sites is also critical particularly for low-loading catalyst layers, as reported by Yu et al. [152]. For this reason, degradation homogeneity is also considered.

Degradation Homogeneity

Degradation homogeneity characterizes the spatial nonuniformity of platinum degradation through the catalyst layer. This metric is motivated by the work of Sadeghi et al. [132], who demonstrated that spatially nonuniform platinum loss especially near the membrane results in larger performance penalties than uniform degradation, even when the total ECSA loss is identical.

In the present study, this behavior was further examined (see Appendix C), where it was shown that comparable performance losses also occur when degradation is localized near the gas diffusion layer. This indicates that the additional losses arise primarily from degradation heterogeneity itself rather than its specific location and are largely driven by increased mass transport limitations associated with heterogeneous platinum distributions.

Accordingly, degradation homogeneity is treated as a key metric and is quantified using the coefficient of variation (CoV) of the slice-averaged ECSA loss in the through-plane direction. The mean slice-averaged surface area loss for a domain consisting of n_{slices} (in this case, $n_{slices} = 130$) is given by

$$\mu_{tp} = \frac{1}{n_{slices}} \sum_{j}^{n_{slices}} SA_j$$

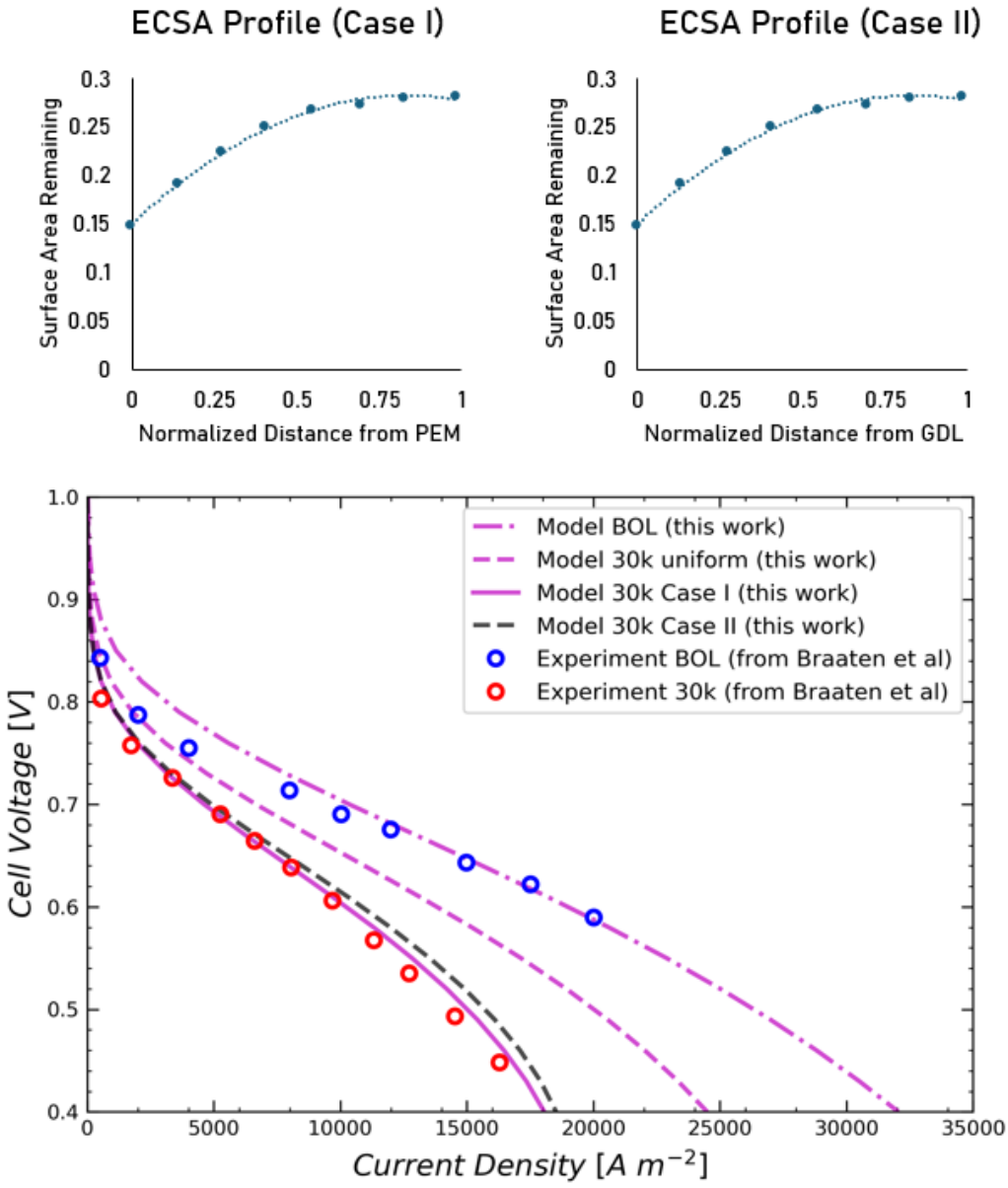
and the standard deviation, σ_{tp},

$$\sigma_{tp} = \sqrt{\frac{1}{n_{slices}} \sum_{j}^{n_{slices}} \left(SA_j - \mu_{tp}\right)^2}$$

Appendix C
Study on the Significance of Degradation Homogeneity

Experimental studies have reported spatially nonuniform catalyst degradation in PEM fuel cell catalyst layers, with greater platinum loss occurring near the membrane interface [178] [94]. Using a pore network model of the catalyst layer, Sadeghi et al. [132] investigated the impact of degradation distribution by removing platinum particles based on the surface area loss observed experimentally by Braaten et al. [135]. They found that uniformly removing platinum throughout the catalyst layer overestimated the cell performance after 30k cycles. However, when the platinum loss was spatially distributed to match the experimentally observed degradation profile (i.e., having greater loss near the membrane), the simulated performance more closely matched the experimental results. This behavior was attributed primarily to increased ohmic losses caused by catalyst depletion near the membrane.

To assess whether this behavior is reproduced in our model, we performed analogous simulations at 30k cycles. Platinum was removed both uniformly throughout the catalyst layer (uniform case) and nonuniformly (Case I) following the experimentally observed degradation profile with more particles being depleted near the membrane. The figure below shows the performance with the uniform case and the performance with Case I, along with the experimental data from Braaten et al. [135]:



We were able to arrive at the same conclusion, with uniform platinum deletion substantially overestimating performance at 30k cycles, and the nonuniform degradation case (Case I) more accurately reproducing the experimental performance curve. This confirms that the spatial distribution of degradation plays a critical role in determining end-of-life performance.

To further understand the underlying mechanisms, we considered an additional "flipped" degradation profile (Case II) in which platinum loss was instead more pronounced in the GDL interface while maintaining the same total ECSA loss and profile shape. The resulting performance is shown above as Case II. Interestingly, the flipped case still produces significantly lower performance compared to the uniform deletion case and remains relatively close to the experimental curve, although it performs slightly better than Case I. This result suggests that the mere presence of spatial heterogeneity, regardless of its orientation or location, substantially affects the performance.

The small improvement observed in the flipped case indicates that degradation near the membrane does contribute to additional ohmic losses. However, the much larger difference between the uniform and nonuniform cases (Cases I and II) demonstrates that mass transport limitations dominate end-of-life behavior. When platinum is unevenly distributed, regions with low local loading due to degradation create higher transport resistance for the reacting species, (dissolved oxygen and protons) which makes it more difficult to access active sites. Thus, performance losses arise not only from reduced total ECSA, but from the spatial redistribution of remaining catalyst. In fact, this interpretation aligns with the findings of Yu et al. [152], who showed that in low-loading catalyst layers, retaining platinum in depleted regions is more important for end-of-life performance than the overall ECSA loss itself. The results of our mini-study provide additional mechanistic insight: spatially heterogeneous degradation increases local mass transport resistance, which becomes increasingly critical as total catalyst loading decreases (i.e., longer-term degradation).

Overall, these findings indicate that degradation homogeneity is a meaningful performance descriptor. Two catalyst layers with identical total ECSA loss can exhibit substantially different performance depending on the spatial distribution of remaining platinum at the end-of-life. Therefore, degradation homogeneity should be considered alongside total ECSA loss when evaluating long-term durability.